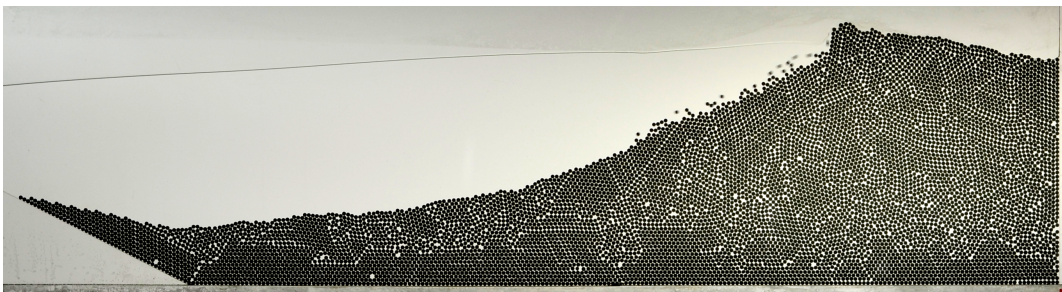


---

# Beach evolution and wave dynamics in a Hele-Shaw geometry

---



*Author:*  
A.J. VAN DER HORN

*Graduation Committee:*  
Prof. Dr. D. LOHSE  
Dr. D. VAN DER MEER  
Dr. A.R. THORNTON  
Dr. Ir. O. BOKHOVE  
Dr. W.K. DEN OTTER

July 2, 2012



I call our world Flatland, not because we call it so, but to make its nature clearer to you, my happy readers, who are privileged to live in Space.

---

Edwin A. Abbott, *'Flatland: A Romance of Many Dimensions'*



## Abstract

In this thesis, the evolution of beach morphologies and the occurrence of breaking waves in a quasi-two-dimensional Hele-Shaw geometry were investigated. This research was divided into three parts.

Firstly, experiments were performed to study the influence of single-frequency generated waves on initially flat beds of nearly monodisperse particles. The beds were observed to evolve into a number of possible steady morphology types. The type of steady morphology reached proved to be mainly dependent on the mean depth of the water layer on top of the bed. A detailed study of the internal bed structure showed a continuous rise in packing fraction of the bed in virtually all performed measurements. This was shown to be caused by both a high packing fraction of the redeposited sediment, and the continuous rearrangement of particles in the rest of the bed.

Secondly, the occurrence of breaking waves in the Hele-Shaw cell has been investigated. Different types of breaking waves have been observed. The characteristics of these breaker types are very similar to those described by Peregrine [21], of breaking waves observed in nature.

Lastly, experiments were performed to validate a numerical model by Gagarina, Van der Vegt, Ambati, and Bokhove [13]. A comparison of potential energies showed very good agreement between experiments and the model.



# Contents

<b>1</b>	<b>Introduction</b>	<b>1</b>
<b>2</b>	<b>Experimental Setup</b>	<b>3</b>
<b>3</b>	<b>Theoretical Aspects</b>	<b>7</b>
3.1	Flow equations . . . . .	7
3.2	Alternative: potential flow assumption . . . . .	12
3.3	Energy . . . . .	13
<b>4</b>	<b>Beach evolution</b>	<b>15</b>
4.1	Parameters . . . . .	15
4.2	Measurements . . . . .	15
4.3	Analysis . . . . .	16
4.4	Results . . . . .	27
4.5	Conclusions and discussion . . . . .	35
<b>5</b>	<b>Wave dynamics</b>	<b>37</b>
5.1	Parameters . . . . .	37
5.2	Measurements . . . . .	38
5.3	Analysis . . . . .	38
5.4	Results . . . . .	40
5.5	Conclusions and discussion . . . . .	43
<b>6</b>	<b>Model valorisation</b>	<b>49</b>
6.1	Parameters and measurement setup . . . . .	50
6.2	Analysis . . . . .	50
6.3	Results . . . . .	52
6.4	Conclusions and discussion . . . . .	54
<b>7</b>	<b>Conclusions and discussion</b>	<b>55</b>
<b>8</b>	<b>Recommendations</b>	<b>57</b>
8.1	Possible future research . . . . .	57
8.2	Possible setup improvements . . . . .	59
	<b>Acknowledgements</b>	<b>61</b>
	<b>Scientific Acknowledgements</b>	<b>63</b>
	<b>Bibliography</b>	<b>66</b>

<b>A</b>	<b>Supplementary experiments</b>	<b>67</b>
A.1	Temperature . . . . .	67
A.2	Surface tension measurements . . . . .	68
A.3	Bed particles . . . . .	70
A.4	Wavemaker motion . . . . .	73
<b>B</b>	<b>Wedge details</b>	<b>75</b>
<b>C</b>	<b>Beach evolution: precursory measurements</b>	<b>77</b>
<b>D</b>	<b>GA beach measurements</b>	<b>83</b>
<b>E</b>	<b>Beach evolution analysis</b>	<b>85</b>
E.1	Coastal region . . . . .	85
E.2	Particle positions . . . . .	87
E.3	Beach surface . . . . .	87
E.4	Initial state and east coast angles . . . . .	89
E.5	Sediment transport . . . . .	90
E.6	Phase diagrams . . . . .	92
E.7	Plotting . . . . .	92
<b>F</b>	<b>Wave dynamics analysis</b>	<b>93</b>
F.1	Free surface detection . . . . .	95
F.2	Plotting . . . . .	96

# Chapter 1

## Introduction

The investigation of formation and erosion of beaches is a much-studied subject in the field of coastal engineering (*e.g.*, [22; 26; 28]). The complexity of the subject lies in the complicated two-way interaction between the beach and the free-surface waves. While the waves induce transport of sediment, thus changing the beach morphology, this beach shape in turn influences the way in which the waves break and where exactly that takes place. To be able to investigate these processes thoroughly, one would wish to take a giant knife and cut the beach in half, giving a clear view of the cross-section of beach and waves, thus enabling a detailed study of the physics going on. Since this is generally accepted as a rather challenging approach to the investigation of the subject, Bokhove [9] thought of a more practical alternative: A vertical Hele-Shaw cell [17], which consists essentially of two parallel glass plates placed very closely together. This cell is filled with water and a layer of particles whose diameters are slightly smaller than the cell width. Waves are generated artificially by a sinusoidally-driven wavemaker. The most important advantage of this approach as compared to large, 3D wave tanks is easily thought of: *everything* is visible. Besides that, everything is controllable; both the geometry of the system as the motion of the wavemaker. Another advantage is that flow inside a Hele-Shaw cell resembles two-dimensional flow. An initial numerical approach to the complex (three-dimensional) interaction of beaches and waves would be the development of a two-dimensional model. The quasi-two-dimensional nature of the flow in this setup means it can be used for the validation of such a model.

To keep the sediment and its dynamics quasi-two-dimensional as well, all sediment particle diameters will have to be close to the glass plate separation distance. This allows for two-dimensional arrangement of the bed, and renders all individual particles visible. In order to have the experiments be as easily modelled as possible, the particles were chosen to be spherical and monodisperse.

Of course, this two-dimensional nature also has its disadvantages. Firstly, the dynamics in 2D are different than in 3D. This means that processes and phenomena observed in these experiments may not all be translated to three dimensions, and attention has to be paid to this difference when comparing the results to 3D measurements. Secondly, the flow is not *completely* two-dimensional. Important deviations from ‘normal’ 2D flow are caused by the Hele-Shaw profile induced by the proximity of the two glass plates; deviations which must also be included in the model equations in order to be comparable to experiments in this setup. Lastly, the monodispersity and spherical form of the bed particles may be easy to simulate, but is far from realistic when compared to natural beaches.

Considering all this, the Hele-Shaw cell approach to the investigation of beach-wave interactions may be considered a fundamental one. Due to the geometry of the setup, all dynamics taking place are visible, while the setup serves as well as a means of validating two-dimensional numerical models. Nevertheless, attention has to be paid to the differences arising between 2D, quasi-2D and 3D dynamics, and the difference in particle sizes and shapes between this experiment and real beaches.

In this work, an attempt has been made to answer the following three questions: (1) How does the bed of mono-disperse particles evolve under influence of single-frequency generated wave trains? (2) Does wave breaking occur in the Hele-Shaw geometry, and if so, is it comparable to the breaking of waves observed in nature? (3) How well do initial models simulate the flow in this setup?

This work is composed as follows. Firstly, chapter 2 treats the details of the Hele-Shaw cell experimental setup. Next, the theoretical aspects and the derivation of equations for numerical modelling of the flow are discussed in chapter 3. After that, the actual experiments and their results are treated one by one in chapters 4 and 5. Chapter 4 discusses the study of bed evolution due to sediment transport for a range of initial bed heights, water layer depths and wavemaker frequencies. Observations of different types of breaking waves and the comparison with their counterparts observed in nature is treated in chapter 5. Experiments done as an initial approach to validation of one of the numerical models and their comparison with the model are presented in chapter 6. After that, the most important conclusions are discussed in chapter 7, and this report finishes with a list of recommendations for setup improvement and future work in chapter 8.

## Chapter 2

# Experimental Setup

For all experiments described in this work, a single experimental setup was used. The most important part of the setup is the Hele-Shaw cell, which is depicted schematically in figure 2.1. The cell consists essentially of two parallel glass plates of length  $L$  and a space of width  $d \ll L$  between them. The Hele-Shaw cell is placed vertically along its short side, and both plates are connected along their short sides and lower long side, thus creating a very narrow tank. The cell is supported by a not-depicted wooden frame, which allows it to remain vertically at all times. At the bottom of the cell, around the middle, a plastic ‘wedge’ in the shape of a truncated triangle is placed of length  $l_w$ , height  $h_w$  and top length  $t_w$ .

The cell is partially filled with water to a depth  $H_0$ , and a number (order of  $10^4$ ) of spherical particles of diameter  $D_b$ , which form a ‘bed’ on the right of the wedge (from the camera’s perspective). Different particles were used in the beach evolution (chapter 4) and wave dynamics (chapter 5) experiments. In the former, porous Gamma Alumina particles were used, while in the latter non-porous glass particles were used. The properties of both types of particles are summarised in table 2.1. More details of these particles, including measurements of porosity, density and size distribution, can be found in appendix A.

A ‘wavemaker’ is added to the cell to be able to create waves. This wavemaker consists of a double metal welding rod of diameter 1.6 mm, one end of which is situated between the glass plates, on the left side of the wedge. The other end is attached to a pivot above the cell, which forms the centre of rotation of the

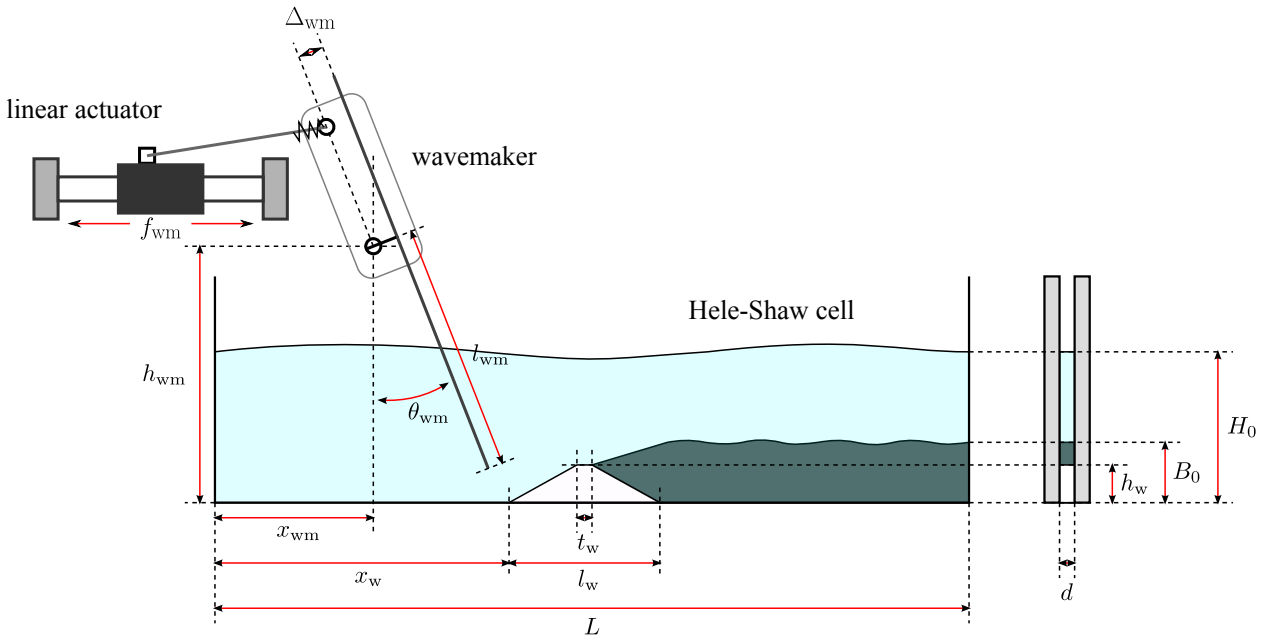
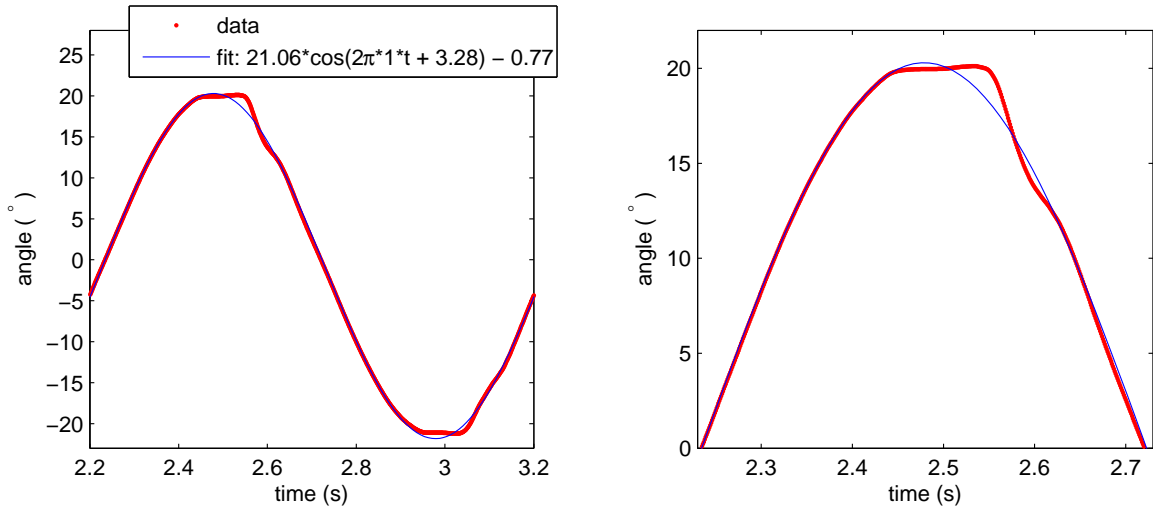


Figure 2.1: Schematic front and side view of Hele-Shaw experiment setup.

Material	Diameter (mm)	Density (g/cm <sup>3</sup> )	Porosity
Gamma Alumina	1.75 ± 0.1	2.08 ± 0.2	0.53 ± 0.05
Glass	1.80 ± 0.1	2.515 ± 0.03	0

Table 2.1: Properties of the spherical particles used in the experiments (see also appendix A.3.2).



(a) One period wavemaker motion. The fit gives the amplitude:  $\theta_{\text{wm}} = 21 \pm 1^\circ$ .

(b) Zoom of the first half of the period, showing the deviation from the sine curve caused by the spring.

Figure 2.2: Measured angular motion of the wavemaker driven at 1 Hz.

wavemaker. Due to construction details, the double metal rod was separated from the pivot by a distance  $\Delta_{\text{wm}}$ . The wavemaker has a length  $l_{\text{wm}}$  as measured from the pivot. The wavemaker is driven by a linear actuator (Copley Controls ThrustTube<sup>®</sup>, type STC-2506-S), which moves back and forth sinusoidally at a fixed amplitude of 30 mm and frequency  $f_{\text{wm}}$ , causing a quasi-sinusoidal motion of the wavemaker of angular amplitude  $\theta_{\text{wm}} \approx 21^\circ$  around the vertical position. The linear actuator is connected to the wavemaker by a metal rod and a spring, which was applied to smoothen the possibly ‘rough’ motion of the linear actuator. The measured resulting angular wavemaker motion is shown in figure 2.2. Figure 2.2a shows one period of motion of the wavemaker driven at 1 Hz. The angular amplitude is obtained from the sinusoidal fit:  $\theta_{\text{wm}} = 21 \pm 1^\circ$ . In figure 2.2b it can be seen that the wavemaker motion deviates from the sinusoidal trajectory around the turning point. This is most likely caused by the presence of the spring in the connection between wavemaker and linear actuator. See also appendix A.4. The wavemaker is the reason for the presence of the wedge, which prevents the bed particles from interfering with the wavemaker motion, which would damage both the wavemaker and the particles.

In total a lot of different experimental parameters had to be taken into account. All of these are listed in table 2.2.

Figure 2.3 shows a schematic top view of the the setup. The Hele-Shaw cell is shown in the middle. The linear actuator driving the wavemaker was controlled by an amplifier (Copley Controls Xenus<sup>®</sup>, type XTL-230-18-S), which in turn was controlled through a PC. The Hele-Shaw cell was illuminated from behind by two Hella<sup>®</sup> flood lights; the light was diffused by a diffuser placed directly behind the cell. A camera recording the measurements was situated in front of the Hele-Shaw cell. Different cameras and lenses were used for different experiments. Table 2.3 lists the camera, lenses and settings used during the three different experiments.

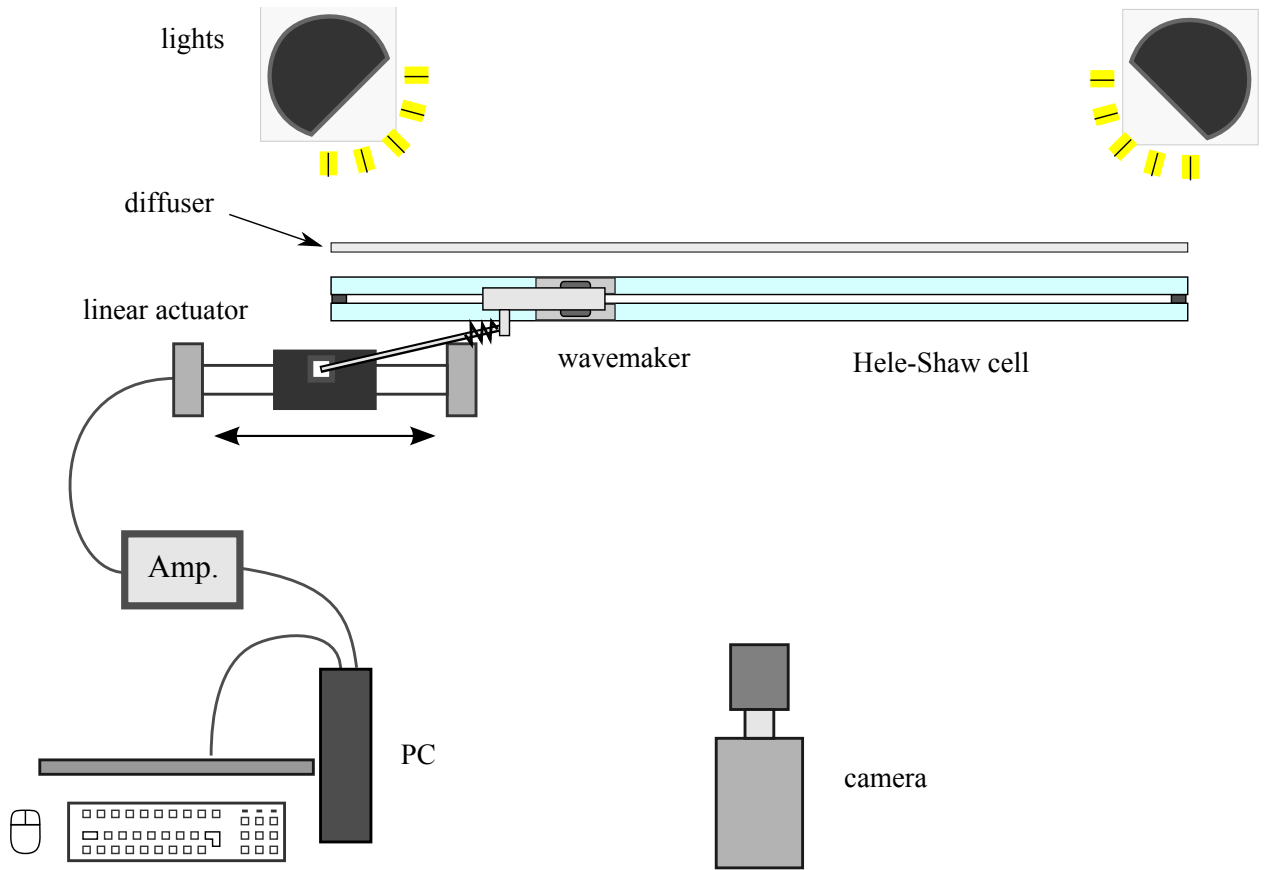


Figure 2.3: Schematic top view of the Hele-Shaw experimental setup.

Geometric		Other	
$L$	Setup length	$f_{\text{wm}}$	Wavemaker frequency
$d$	Setup width	$T$	Temperature
$H_0$	Mean liquid depth	$f_\rho$	Fluid density
$B_0$	Initial beach height	$f_\mu$	Fluid dynamic viscosity
$x_w$	Wedge horizontal position	$\sigma$	Fluid-air surface tension
$l_w$	Wedge length	$b_\rho$	Particle material density
$h_w$	Wedge height	$b_\Phi$	Particle porosity
$t_w$	Wedge top length	$D_b$	Particle diameter
$x_{\text{wm}}$	Wavemaker pivot horizontal position		
$\Delta_{\text{wm}}$	Wavemaker pivot-to-rod distance		
$h_{\text{wm}}$	Wavemaker pivot vertical position		
$l_{\text{wm}}$	Wavemaker length		
$\theta_{\text{wm}}$	Wavemaker angle amplitude		

Table 2.2: List of all Hele-Shaw experiment parameters.

<b>Experiment</b>	<b>Camera type</b>	<b>Lens type</b>	<b>framerate (fps)</b>	<b>shutter time (ms)</b>
Beach evolution	Nikon D5100	Nikon AF Nikkor 50 mm	0.1	8
Wave dynamics	Photron SA2	Nikon AF Nikkor 50 mm & Sigma Makro 50 mm	1000	1
Model valorisation	Mikrotron Eosens	Avanar 28 mm	500	1.5

Table 2.3: Camera, lens and settings used in the different experiments.

# Chapter 3

## Theoretical Aspects

One of the long-term goals in the investigation of beach and shore dynamics is the development of a numerical model capable of simulating waves breaking on the shore and its effect on the bed in terms of transport of sediment. As a first approach, Bokhove [11] has worked on a model describing the flow in a Hele-Shaw geometry, in particular the one used in the experiments described in this thesis. His derivation is described in section 3.1. A potential flow approximation to his equations, which was numerically implemented by Gagarina et al. [3; 13], is treated in 3.2. In order to validate the model, the energy in the system is compared, as explained in section 3.3.

The detailed treatment of the models derived by Bokhove [11] and Gagarina et al. [13] is essential to the understanding of the origins of possible differences arising between model and experiments. This chapter may serve as a reference for future research on this project.

### 3.1 Flow equations

Equations for the flow in the experiments described in this thesis are derived starting with the Cauchy momentum and mass equations. These are non-dimensionalised, simplified using suitable assumptions, and lastly width- and depth-averaged following the derivation in Bokhove, van der Horn, van der Meer, Zweers, and Thornton [10].

#### 3.1.1 Governing equations

The Cauchy mass and momentum conservation equations are

$$\frac{D\rho}{Dt} + \rho(\nabla \cdot \underline{u}) = 0 \quad (\text{mass}) \quad (3.1)$$

$$\frac{D}{Dt}(\rho \underline{u}) = \nabla \cdot \underline{\underline{\sigma}} + \rho \underline{B}, \quad (\text{momentum}) \quad (3.2)$$

in which  $\frac{D}{Dt} = \frac{\partial}{\partial t} + (\underline{u} \cdot \nabla)$  is the material derivative,  $\underline{u} = (u, v, w)^T$  is the velocity field,  $\rho$  is the fluid density,  $\underline{\underline{\sigma}}$  is the stress tensor and  $\underline{B}$  is the external body force. The only body force present in our case is gravity which points in the negative  $z$ -direction, i.e.  $\underline{B} = -g\underline{e}_z$ . Also important are the kinematic boundary conditions at the bottom  $b(x, t)$  and free surface  $s(x, t)$ , which basically state that no fluid is to pass these boundaries (although the boundaries themselves may be moving). They are

$$\frac{D(s-z)}{Dt} = \frac{\partial s}{\partial t} + u_s \frac{\partial s}{\partial x} - w_s = 0 \quad (3.3)$$

$$\frac{D(b-z)}{Dt} = \frac{\partial b}{\partial t} + u_b \frac{\partial b}{\partial x} - w_b = 0. \quad (3.4)$$

### 3.1.2 Incompressibility

The fluid is assumed to be incompressible and homogeneous, which is reflected in a constant density  $\rho(\underline{x}, t) = \rho_0$ . This reduces the Cauchy mass equation 3.1 to

$$\nabla \cdot \underline{u} = \frac{\partial u}{\partial x} + \frac{\partial v}{\partial y} + \frac{\partial w}{\partial z} = 0. \quad (3.5)$$

The stress tensor for an incompressible, Newtonian fluid is given by

$$\sigma_{ij} = -p\delta_{ij} + \mu \left( \frac{\partial u_i}{\partial x_j} + \frac{\partial u_j}{\partial x_i} \right). \quad (3.6)$$

This reduces equation 3.2 to the incompressible Navier-Stokes equation,

$$\frac{\partial \underline{u}}{\partial t} + (\underline{u} \cdot \nabla) \underline{u} = -\frac{1}{\rho_0} \nabla p - g \underline{e}_z + \nu \nabla^2 \underline{u}, \quad (3.7)$$

in which  $\nu = \mu/\rho_0$  is the kinematic viscosity and  $\mu$  is the dynamic viscosity of the fluid. Adding  $0 = \underline{u}(\nabla \cdot \underline{u})$  to the left-hand side yields

$$\frac{\partial \underline{u}}{\partial t} + \nabla \cdot (\underline{u} \underline{u}^T) = -\frac{1}{\rho_0} \nabla p - g \underline{e}_z + \nu \nabla^2 \underline{u}. \quad (3.8)$$

### 3.1.3 Non-dimensionalisation

In order to evaluate the relative sizes of the different terms, the governing equations 3.5,3.8 are non-dimensionalised using the following transformations

$$\begin{aligned} x &= L\tilde{x}, & y &= d\tilde{y}, & z &= H\tilde{z}, & u &= U\tilde{u}, & v &= \epsilon U\tilde{v}, & w &= \delta U\tilde{w}, \\ t &= T\tilde{t} = \frac{L}{U}\tilde{t}, & p &= P_0\tilde{p}, \end{aligned} \quad (3.9)$$

in which  $L$  is the setup length,  $2l$  is the setup width,  $H$  is the typical liquid depth,  $\epsilon = l/L$ ,  $\delta = H/L$  and  $P_0 = \rho_0 U^2$ . The Reynolds number is defined as  $\text{Re} = UL/\nu$ , which is a measure for the ratio of inertial and viscous forces. For water at room temperature in the geometry considered, we have  $L = \mathcal{O}(1\text{m})$ ,  $l = 1 \cdot 10^{-3}\text{m}$ ,  $H = \mathcal{O}(0.1\text{m})$ ,  $\rho_0 = 998\text{kg/m}^3$  and  $\mu = 8.94 \cdot 10^{-4}\text{Pa} \cdot \text{s}$ . Estimating  $U = \mathcal{O}(0.1)\text{m/s}$  implies  $\text{Re} = \mathcal{O}(10^5)$ . Furthermore, the Froude number, which is a measure for the ratio of inertial and gravitational forces, is defined as  $\text{Fr} = U/\sqrt{gH}$ , so that  $\text{Fr} = \mathcal{O}(0.1)$ .

The non-dimensionalised Navier-Stokes and continuity equations become, dropping the tildes,

$$\frac{\partial u}{\partial t} + \frac{\partial u^2}{\partial x} + \frac{\partial uv}{\partial y} + \frac{\partial uw}{\partial z} = -\frac{\partial p}{\partial x} + \frac{1}{\text{Re}} \left( \frac{\partial^2 u}{\partial x^2} + \frac{1}{\epsilon^2} \frac{\partial^2 u}{\partial y^2} + \frac{1}{\delta^2} \frac{\partial^2 u}{\partial z^2} \right) \quad (3.10a)$$

$$\frac{\partial v}{\partial t} + \frac{\partial uv}{\partial x} + \frac{\partial v^2}{\partial y} + \frac{\partial vw}{\partial z} = -\frac{1}{\epsilon^2} \frac{\partial p}{\partial y} + \frac{1}{\text{Re}} \left( \frac{\partial^2 v}{\partial x^2} + \frac{1}{\epsilon^2} \frac{\partial^2 v}{\partial y^2} + \frac{1}{\delta^2} \frac{\partial^2 v}{\partial z^2} \right) \quad (3.10b)$$

$$\frac{\partial w}{\partial t} + \frac{\partial uw}{\partial x} + \frac{\partial vw}{\partial y} + \frac{\partial w^2}{\partial z} = -\frac{1}{\delta^2} \frac{\partial p}{\partial z} + \frac{1}{\text{Re}} \left( \frac{\partial^2 w}{\partial x^2} + \frac{1}{\epsilon^2} \frac{\partial^2 w}{\partial y^2} + \frac{1}{\delta^2} \frac{\partial^2 w}{\partial z^2} \right) - \frac{1}{\text{Fr}^2 \delta^2} \quad (3.10c)$$

$$\frac{\partial u}{\partial x} + \frac{\partial v}{\partial y} + \frac{\partial w}{\partial z} = 0. \quad (3.10d)$$

The values of  $\epsilon = \mathcal{O}(10^{-3})$  and  $\delta = \mathcal{O}(0.1)$  imply  $1/\epsilon^2 \gg 1/\delta^2 \gg 1$ , so the viscous term in the Navier-Stokes equation reduces to  $1/(\text{Re} \epsilon^2) \cdot (\partial_{yy} u + \mathcal{O}(1/\delta^2))$ . This reduces the Navier-Stokes  $Y$ -equation (3.10b) to

$$\frac{\partial v}{\partial t} + \frac{\partial uv}{\partial x} + \frac{\partial v^2}{\partial y} + \frac{\partial vw}{\partial z} = -\frac{1}{\epsilon^2} \frac{\partial p}{\partial y} + \frac{1}{\text{Re} \epsilon^2} \left( \frac{\partial^2 v}{\partial y^2} + \mathcal{O}\left(\frac{\epsilon^2}{\delta^2}\right) \right). \quad (3.11)$$

All prefactors on the LHS are of order 1, and since  $\text{Re}$  is of order  $10^5$ ,  $1/(\text{Re} \epsilon^2) = \mathcal{O}(10)$ . The pressure term however dominates, which is  $\mathcal{O}(1/\epsilon^2) = \mathcal{O}(10^6)$ . This reduces equation (3.11) further to

$$\frac{\partial p}{\partial y} = \mathcal{O}(1/\text{Re}) \approx 0. \quad (3.12)$$

In other words, the pressure is independent of  $y$ , i.e.  $p = p(x, z, t)$ . The Navier-Stokes  $Z$ -equation (3.10c) is reduced to

$$\frac{\partial w}{\partial t} + \frac{\partial uw}{\partial x} + \frac{\partial vw}{\partial y} + \frac{\partial w^2}{\partial z} = -\frac{1}{\delta^2} \frac{\partial p}{\partial z} + \frac{1}{\text{Re} \epsilon^2} \left( \frac{\partial^2 w}{\partial y^2} + \mathcal{O} \left( \frac{\epsilon^2}{\delta^2} \right) \right) - \frac{1}{\text{Fr}^2 \delta^2} . \quad (3.13)$$

The prefactors on the LHS are of order 1, while for the RHS holds  $1/(\text{Re} \epsilon^2) < 1/\delta^2$ ,  $1/(\text{Fr}^2 \delta^2)$ . This reduces equation (3.13) to

$$\frac{\partial p}{\partial z} + \frac{1}{\text{Fr}^2} = \mathcal{O} \left( \frac{\delta^2}{\text{Re} \epsilon^2} \right) . \quad (3.14)$$

Since  $\delta^2/(\text{Re} \epsilon^2) \ll 1$  hydrostatic pressure is obtained,

$$\frac{\partial p}{\partial z} = -\frac{1}{\text{Fr}^2} .$$

Integrating over  $z$  then gives the pressure,

$$\int_z^{s(x,t)} \frac{\partial p}{\partial z} dz = -\frac{1}{\text{Fr}^2} [z']_z^s$$

$$p(x, z, t) = p_s + \frac{1}{\text{Fr}^2} (s(x, t) - z) , \quad (3.15)$$

in which  $p_s$  is the ambient pressure (which is of little importance here, since only derivatives of  $p$  are considered). The Navier-Stokes  $X$ -equation (3.10a) is reduced only in the viscous term,

$$\frac{\partial u}{\partial t} + \frac{\partial u^2}{\partial x} + \frac{\partial uv}{\partial y} + \frac{\partial uw}{\partial z} = -\frac{\partial p}{\partial x} + \frac{1}{\text{Re} \epsilon^2} \left( \frac{\partial^2 u}{\partial y^2} + \mathcal{O} \left( \frac{\epsilon^2}{\delta^2} \right) \right) , \quad (3.16)$$

in which all prefactors except  $\mathcal{O}(\epsilon^2/\delta^2)$  are of order 1 or larger.

All prefactors in the continuity equation 3.10d are of order 1, so nothing changes there. The kinematic boundary conditions at  $s$  and  $b$  keep the same form as the dimensionalised ones,

$$\frac{\partial s}{\partial t} + u_s \frac{\partial s}{\partial x} - w_s = 0 \quad (3.17a)$$

$$\frac{\partial b}{\partial t} + u_b \frac{\partial b}{\partial x} - w_b = 0 . \quad (3.17b)$$

### 3.1.4 Hele-Shaw flow

Since the experimental setup (chapter 2) consists of two parallel plates placed close together, the assumption of Hele-Shaw flow is investigated. In Hele-Shaw flow the inertial terms become negligible, and the flow profiles in the two directions parallel to the plates are governed by the balance of pressure, gravity and viscous terms. Since pressure and gravity are  $y$ -independent,  $u$  and  $w$  are governed by

$$\frac{\partial^2 u_i}{\partial y^2} = C_i , \quad (3.18)$$

in which  $u_i$  is  $u$  or  $w$ , and  $C$  is constant in  $y$ . This gives the general parabolic solution

$$u_i = \frac{C_i}{2} y^2 + C_2 y + C_3 .$$

The no-slip boundary conditions  $u_i(1) = u_i(-1) = 0$  apply, giving for  $u_i$

$$u_i = \frac{C_i}{2} (y^2 - 1) .$$

Rewriting in terms of the depth-averaged velocity  $\bar{u}_i = 1/2 \int_{-1}^1 u_i dy = -C_i/3$  leads to

$$u_i = \frac{3}{2} \bar{u}_i (1 - y^2) . \quad (3.19)$$

Dimensionally, this would be

$$u_i = \frac{3}{2}\bar{u}_i(1 - y^2) . \quad (3.20)$$

To see whether the Hele-Shaw flow assumption is allowed, the magnitude of the viscous or pressure term (Stokes flow:  $\nabla_i p = \mu \nabla^2 u_i$ ) is compared to that of the inertia terms as done by Batchelor [6, Ch. 4]. The magnitude of the inertial term (in dimensional form) is estimated to be

$$\rho_0 \frac{Du}{Dt} \approx \rho_0 \frac{3u^2}{L} , \quad (3.21)$$

and the viscous and pressure term,

$$\partial_x p = \mu \nabla^2 u \approx \mu \frac{u}{l^2} . \quad (3.22)$$

So, the Hele-Shaw flow assumption is valid if

$$\frac{3\rho_0 u^2}{L \partial_x p} \approx \frac{3\rho_0 l^2 u}{\mu L} \ll 1 . \quad (3.23)$$

Everything in equation (3.23) is known, except for the horizontal velocity  $u$ , which can be estimated in two different ways. Firstly, by an estimation of the magnitude of the pressure gradient,

$$u \approx \frac{l^2 \partial_x p}{\mu} \approx \frac{l^2 \rho_0 g \Delta h}{\mu} , \quad (3.24)$$

in which  $\Delta h$  is twice the observed wave magnitude. Estimating  $\Delta h \approx 3$  cm based on observation leads to

$$\frac{3\rho_0 l^2 u}{\mu L} \approx \frac{3\rho_0^2 l^4 g \Delta h}{\mu^2 L} = 1.11 . \quad (3.25)$$

Secondly,  $u$  can be estimated to be the maximum velocity of the wavemaker,

$$u_{max,wm} = 2\pi f_{wm} \theta_{wm} l_{wm} , \quad (3.26)$$

in which  $f_{wm}$  is the wavemaker frequency,  $\theta_{max,wm}$  the wavemaker amplitude and  $l_{wm}$  the wavemaker length, see chapter 2. Using  $f_{wm} = 1.3$  Hz,  $\theta_{wm} \approx 20^\circ = 1/9$  rad and  $l_{wm} = 32$  cm implies  $u_{max,wm} = 0.29$  m/s, and

$$\frac{3\rho_0 l^2 u}{\mu L} = 0.98 . \quad (3.27)$$

Both estimations of  $u$  indicate that the inertia and pressure terms are of the same order. Besides the fact that it is on the edge of validity, Hele-Shaw flow will be assumed for the sake of simplicity; the possible error introduced due to this will be further investigated afterwards. For the non-dimensional velocities this comes down to

$$u = \frac{3}{2}\bar{u}(1 - y^2) \quad (3.28a)$$

$$w = \frac{3}{2}\bar{w}(1 - y^2) . \quad (3.28b)$$

### 3.1.5 Width averaging

Using equations 3.28, the Navier-Stokes, continuity and kinematic boundary condition equations can now be width-averaged, as done by Polhausen in Rosenhead [23]. A width-averaged variable is defined as follows,

$$\bar{f} = \frac{1}{2} \int_{-1}^1 f \, dy , \quad (3.29)$$

in which  $\bar{f}$  is the width-averaged variable and  $f$  is the original one. Applying this to the reduced Navier-Stokes  $X$ -equation (3.16) results in

$$\frac{\partial \bar{u}}{\partial t} + \frac{\partial \bar{u}^2}{\partial x} + \underbrace{[uv]_{y=-1}^1}_0 + \frac{\partial \bar{u}\bar{w}}{\partial z} = -\frac{\partial p}{\partial x} - \frac{3\bar{u}}{\text{Re} \epsilon^2} . \quad (3.30)$$

For  $\overline{u^2}$  is found

$$\begin{aligned}
\overline{u^2} &= \frac{1}{2} \int_{-1}^1 \frac{9}{4} \overline{u^2} (1-y^2)^2 dy \\
&= \frac{9}{8} \overline{u^2} \left[ \frac{y^5}{5} - \frac{2y^3}{3} + y \right]_{y=-1}^1 \\
&= \frac{6}{5} \overline{u^2} = \gamma \overline{u^2} .
\end{aligned} \tag{3.31}$$

The same prefactor  $\gamma = 6/5$  is obtained for  $\overline{u\overline{w}}$ . Substitution into equation (3.30) results in

$$\frac{\partial \overline{u}}{\partial t} + \gamma \frac{\partial \overline{u^2}}{\partial x} + \gamma \frac{\partial (\overline{u\overline{w}})}{\partial z} = - \frac{\partial p}{\partial x} - \frac{3\overline{u}}{\text{Re} \epsilon^2} . \tag{3.32}$$

Width-averaging the non-dimensional continuity equation (3.10d) leads to

$$\frac{\partial \overline{u}}{\partial x} + \underbrace{[v]_{y=-1}^1}_0 + \frac{\partial \overline{w}}{\partial z} = 0 , \tag{3.33}$$

and the kinematic boundary conditions (3.17) become

$$\frac{\partial s}{\partial t} + \overline{u}_s \frac{\partial s}{\partial x} - \overline{w}_s = 0 \tag{3.34a}$$

$$\frac{\partial b}{\partial t} + \overline{u}_b \frac{\partial b}{\partial x} - \overline{w}_b = 0 . \tag{3.34b}$$

### 3.1.6 Depth averaging

As a further simplification, everything is depth-averaged in the vertical direction. A depth-averaged variable is defined as follows,

$$f' = \frac{1}{h} \int_{b(x,t)}^{s(x,t)} \overline{f} dz , \tag{3.35}$$

in which  $h(x,t) = s - b$  is the local water depth,  $f'$  is the width- and depth-averaged variable and  $\overline{f}$  is the just width-averaged one.

Applying this to the width-averaged Navier-Stokes  $X$ -equation (3.32) gives for the pressure term, using eq. (3.15)),

$$\begin{aligned}
\int_b^s \frac{\partial p}{\partial x} &= \int_b^s \frac{1}{\text{Fr}^2} \frac{\partial}{\partial x} (s-z) dz \\
&= \frac{1}{\text{Fr}^2} \left( \frac{\partial}{\partial x} \int_b^s (s-z) dz - \left[ (s-q) \frac{\partial q}{\partial x} \right]_{q=b}^s \right) \\
&= \frac{1}{\text{Fr}^2} \left( \frac{\partial}{\partial x} \left( \frac{s^2}{2} - bs + \frac{b^2}{2} \right) + h \frac{\partial b}{\partial x} \right) \\
&= \frac{1}{\text{Fr}^2} \left( \frac{\partial}{\partial x} \left( \frac{h^2}{2} \right) + h \frac{\partial b}{\partial x} \right) ,
\end{aligned} \tag{3.36}$$

and for the whole equation,

$$\frac{\partial hu'}{\partial t} + \gamma \frac{\partial hu'^2}{\partial x} - \left[ \overline{u} \left( \frac{\partial q}{\partial t} + \gamma \overline{u} \frac{\partial q}{\partial x} - \gamma \overline{w} \right) \right]_{q=b}^s = - \frac{1}{\text{Fr}^2} \left( \frac{\partial}{\partial x} \left( \frac{h^2}{2} \right) + h \frac{\partial b}{\partial x} \right) - \frac{3u'}{\text{Re} \epsilon^2} ,$$

in which was assumed  $(\overline{u^2})' = u'^2$ , i.e. uniform flow over the depth  $h$ . Substitution of the width-averaged kinematic boundary conditions eqs. (3.34) and again assuming uniform flow leads to

$$\frac{\partial hu'}{\partial t} + \frac{\partial}{\partial x} \left( \frac{h^2}{2\text{Fr}^2} + \gamma hu'^2 \right) = - \frac{1}{\text{Fr}^2} h \frac{\partial b}{\partial x} - \frac{3u'}{\text{Re} \epsilon^2} + (1-\gamma)u' \frac{\partial h}{\partial t} . \tag{3.37}$$

Depth-averaging the width-averaged continuity equation (3.33) results in

$$\frac{\partial(hu')}{\partial x} - \left[ \frac{\partial q}{\partial x} \right]_{q=b}^s + [\bar{w}]_b^s = 0 ,$$

and substituting the kinematic boundary conditions eqs. (3.34),

$$\frac{\partial(hu')}{\partial x} + \left[ \frac{\partial q}{\partial t} \right]_{q=b}^s = \frac{\partial(hu')}{\partial x} + \frac{\partial h}{\partial t} = 0 . \quad (3.38)$$

Using eq. (3.38), eq. (3.37) can be rewritten to become

$$\frac{\partial hu'}{\partial t} + \frac{\partial}{\partial x} \left( \frac{h^2}{2\text{Fr}^2} + hu'^2 \right) + (\gamma - 1)hu' \frac{\partial u'}{\partial x} = -\frac{1}{\text{Fr}^2}h \frac{\partial b}{\partial x} - \frac{3u'}{\text{Re}\epsilon^2} . \quad (3.39)$$

### 3.1.7 Re-dimensionalisation

Rewriting eqs. (3.39) and (3.38) to dimensional form leads to (dropping the primes)

$$\frac{\partial(hu)}{\partial t} + \frac{\partial}{\partial x} \left( \frac{gh^2}{2} + hu^2 \right) + (\gamma - 1)hu \frac{\partial u}{\partial x} = -gh \frac{\partial b}{\partial x} - \frac{3\nu u}{l^2} \quad (3.40a)$$

$$\frac{\partial(h')}{\partial x} + \frac{\partial h}{\partial t} = 0 . \quad (3.40b)$$

In the width- and depth-averaged reduced Navier-Stokes  $X$ -equation (3.40a), all terms on the LHS except  $\partial gh^2/\partial x$  originate from the inertia terms of the Navier Stokes equation. The last of these,  $hu(\gamma-1)(\partial u)/(\partial x)$ , is present due to the non-uniformity of the Hele-Shaw flow in the  $y$ -direction; in uniform flow,  $\gamma$  would be 1 and the term would vanish. The terms  $(g/2)(\partial h^2/\partial x)$  on the LHS and  $gh(\partial b/\partial x)$  on the LHS originate from the pressure term; they indicate the contributions of the  $x$ -derivatives of the bottom and surface profiles  $b$  and  $s = h + b$  to the derivative of the pressure  $\partial p/\partial x$ . The last term on the RHS,  $3\nu u/l^2$ , represents the viscous dissipation of momentum due to the Hele-Shaw flow profile in the  $y$ -direction. Equation 3.40b is simply the width- and depth-averaged reduced continuity equation. The numerical implementation of equations (3.40) is still work-in-progress.

## 3.2 Alternative: potential flow assumption

An alternative to eqs. (3.40) can be derived using the assumption of potential flow in the  $x$  and  $z$ -directions. Assuming potential flow is a common practice and the derivation of its equations can be found in many text books, e.g. Whitham [27, Ch. 13]. The flow is assumed to be inviscid and irrotational in the  $x$ - and  $z$ -directions, so that

$$\mathbf{u} = \nabla \phi , \quad (3.41)$$

in which  $\phi$  is the so-called flow potential. This reduces the dimensional 2D width-averaged continuity equation (dimensional form of (3.33)) to the Laplace equation (dropping the primes),

$$\frac{\partial u}{\partial x} + \frac{\partial w}{\partial z} = \frac{\partial^2 \phi}{\partial x^2} + \frac{\partial^2 \phi}{\partial z^2} = \nabla^2 \phi = 0 . \quad (3.42)$$

The dimensional width-averaged 2D Navier-Stokes equation (dimensional form of (3.39)) can be slightly reformulated to become

$$\frac{\partial \mathbf{u}}{\partial t} + \gamma \nabla \left( \frac{1}{2} \mathbf{u}^2 \right) + \underbrace{\gamma(\boldsymbol{\omega} \times \mathbf{u})}_{=0} = -\frac{1}{\rho_0} \nabla p - g\mathbf{k} - \frac{3\nu}{l^2} \mathbf{u} , \quad (3.43)$$

in which  $\omega = \nabla \times \mathbf{u}$  is the vorticity, which is zero by definition in potential flow, and  $\gamma = 6/5$  is the prefactor introduced to the non-uniformity of the Hele-Shaw flow profile. Substituting eq. (3.41) and integrating the equation components over their respective spacial coordinates yields

$$\frac{\partial \phi}{\partial t} + \frac{\gamma}{2} (\nabla \phi)^2 + gz - \frac{3\nu \phi}{l^2} = \frac{p - p_0}{\rho_0} . \quad (3.44)$$

Let the free surface be described by

$$\eta(x, t) = h(x, t) - h_0 , \quad (3.45)$$

in which  $h_0$  is the static water depth. Evaluating equation (3.44) at the free surface gives the dynamic boundary condition,

$$\frac{\partial \phi}{\partial t} + \frac{\gamma}{2} (\phi_x^2 + \phi_z^2) + g\eta - \frac{3\nu \phi}{l^2} = 0 \quad \text{at } z = \eta , \quad (3.46)$$

in which  $\phi_{x_i} = \partial \phi / \partial x_i$  and the pressure difference due to the surface tension has been neglected. The kinematic boundary condition at the free surface is

$$\eta_t + \frac{\partial \phi}{\partial x} \frac{\partial \eta}{\partial x} = \frac{\partial \phi}{\partial z} \quad \text{at } z = \eta . \quad (3.47)$$

Hence, the system is described by equations (3.42), (3.46) and (3.47). This set of equations was numerically implemented by Gagarina et al. [13]. Experiments conducted to verify the numerical results are described in chapter 6.

### 3.3 Energy

The verification of the the numerical model by Gagarina et al. [13] by comparison of the flow field is challenging experimentally. Therefore, the energy in the system was studied instead. The total energy present in the system is

$$E = E_k + E_p + E_s , \quad (3.48)$$

in which  $E$  is the total energy present in the system,  $E_k$  the kinetic energy,  $E_p$  the potential energy and  $E_s$  the energy stored in the water surface. The kinetic energy is given by

$$E_k(t) = \int_0^L \int_{-h_0}^{\eta} \rho_0 (u(x, z, t)^2 + w(x, z, t)^2) dz dx . \quad (3.49)$$

in which  $E_k$  is the potential energy *per unit width*, and in the integration of  $z$ ,  $z = 0$  is taken to be at the mean free surface. To know the kinetic energy, one needs to know the exact flow field inside the system, which is not known in experiments. The potential energy (per unit width) however can be obtained more easily. Only the position of the free water surface  $\eta(x, t)$  and some static parameters are needed,

$$E_p(t) = \int_0^L \int_0^{\eta} \rho_0 g z dz dx = \frac{1}{2} \rho_0 g \int_0^L \eta(x, t)^2 dx , \quad (3.50)$$

The additional energy per unit width stored in the water surface as compared to the static case is

$$E_s(t) = \sigma_{aw} (l_s(t) - L) , \quad (3.51)$$

in which  $\sigma_{aw}$  is the air-water surface tension and  $l_s$  is the length of the free surface. The neglect of the surface tension in the numerical model might be a cause of possible difference between experiments and the model.



# Chapter 4

## Beach evolution

When considering waves breaking on the shore, one of the questions that rise is how the waves influence the shore itself. How do waves transport the sediment? How does the bed morphology change over time? Inspired by these questions, the evolution of a bed of monodisperse particles in the Hele-Shaw configuration was studied for different sets of the parameters mentioned in section 2. Since this represents a large parameter space, it was decided to focus on only three of them, keeping all others fixed. These were the initial bed height  $B_0$ , the difference between bed and fluid height  $H_0 - B_0$  and the wavemaker frequency  $f_{\text{wm}}$ . Of importance is the time scale in which the bed evolution happens. It was found that significant changes to the beach shape due to the surface waves occur in a matter of minutes to hours. Making a photograph every 10 seconds proved sufficient to capture the key details of the bed evolution process.

### 4.1 Parameters

The values of fixed and varied parameters examined in the beach evolution measurements are summarised in table 4.1. The values of  $B_0$ ,  $(H_0 - B_0)$  and  $f_{\text{wm}}$  were chosen based on precursory experiments undertaken in December 2011. The details of this original measurement series can be found in appendix C. The geometrical parameters are kept fixed. The wavemaker motion is controlled by a linear motor as described in chapter 2. The amplitude of the linear motor was fixed at 30 mm, at which the wavemaker angular motion was measured as described in section A.4. The temperature was not controlled but merely measured. The water temperature was found to be very close to the room temperature at all times, which proved to be between 23.5 and 28 °C in most of the experiments, while it reached higher temperatures, up to 28.7°C, in only 3 out of 80 cases. At the beginning of each day of measuring, the setup was flushed a few times with fresh MilliQ<sup>®</sup> water before being filled to the desired water level  $H_0$ . The surface tension experiments in appendix A.2 imply a significant change in surface tension within a matter of hours to days. Therefore, the setup was drained and refilled with new MilliQ<sup>®</sup> water between each measurement, resulting in a relatively constant surface tension, as was also measured and described in section A.2. The details of the beach particle parameters can be found in section A.3.

### 4.2 Measurements

In total 80 measurements have been performed. To make sure a possible variation of one of the (fixed) parameters during the course of a day would not coincide with a gradual variation of one of the intentionally varied parameters, the measurements were done in a semi-random order. Since adding and removing particles from the experiments takes a lot of time (partially due to their porosity), all measurements per beach height  $B_0$  were performed successively. However, the order of  $(H_0 - B_0)$  and  $f_{\text{wm}}$  were completely randomised within each  $B_0$  series. The exact order of performed measurements can be found in appendix D.

To setup each experiment, a fixed procedure was followed. The beach was flattened manually and its height  $B_0$  measured and checked to match the one desired. The water in the setup was drained and then

Varied parameters		Fixed parameters	
Parameter	Values	Parameter	Value
$H_0 - B_0$	$\in [10, 30, 50, 70] \pm 3$ mm	$L$	$956 \pm 1$ mm
$B_0$	$\in [50, 60, 70, 80] \pm 2$ mm	$d$	$2.0 \pm 0.05$ mm
$f_{wm}$	$\in [0.7, 0.9, 1.0, 1.1, 1.3]$ Hz	$x_w$	$363 \pm 1$ mm
		$l_w$	$212 \pm 0.1$ mm (app. B)
		$h_w$	$50 \pm 0.1$ mm (app. B)
		$t_w$	$20 \pm 0.1$ mm (app. B)
		$x_{wm}$	$205 \pm 1$ mm
		$\Delta_{wm}$	$15 \pm 0.5$ mm
		$h_{wm}$	$326 \pm 2$ mm
		$l_{wm}$	$319 \pm 2$ mm
		$\theta_{wm}$	$21 \pm 1^\circ$ (app.A.4)
		$T$	$23-29$ °C
		$f_\rho$	$\rho_{water}$
		$f_\mu$	$\mu_{water}$
		$\sigma$	$\sigma_{air-water}$ (app. A.2)
		$\rho_b$	$2.08 \pm 0.2$ g cm <sup>-3</sup> (app. A.3.2)
		$\Phi_b$	$0.45 \pm 0.09$ (app. A.3.2)
		$D_b$	$1.8 \pm 0.1$ mm (app. A.3.1)

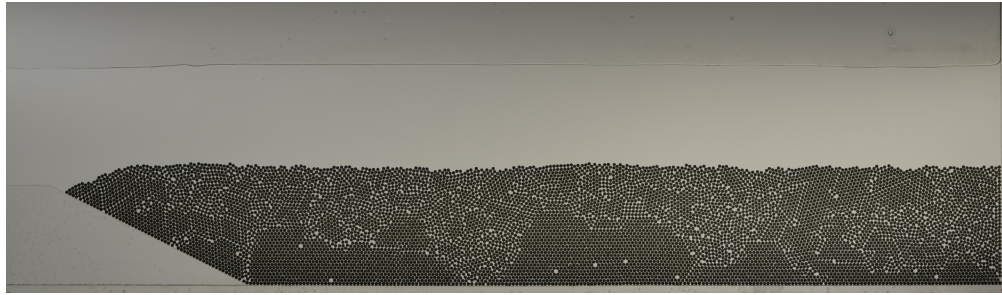
Table 4.1: Hele-Shaw beach experiment parameter values.

the setup was refilled with clean MilliQ<sup>®</sup> until its level was the desired depth  $H_0$ . A plug was applied to the water input tube, to make sure no energy would be dissipated during the measurement due to flow in this tube. A Nikon D5100 camera with a Nikon AF Nikkor 50 mm lens was used to take a photograph each 10 seconds. A square grid with spacing 20 mm was attached to the front glass of the Hele-Shaw cell, photographed, and then taken off again. This not only provided a reliable meter-per-pixel ratio for the measurements, but also allowed to check for possible lens distortions in the region of interest. The first photograph of each measurement consists of the static, initial configuration. In the 10 seconds between the first and second photograph, the linear actuator was put into motion, accelerating from rest to the desired constant frequency in a linear way within approximately 2 seconds. After that, the experiment was left running until an invariant or only very slowly varying beach state was reached. This had to be estimated by mere observation, since only thorough analysis afterwards could really quantify the beach invariability (this analysis and its results can be found in section 4.3.1). At that moment, the camera and wavemaker were switched off, and the photographs were downloaded to a computer.

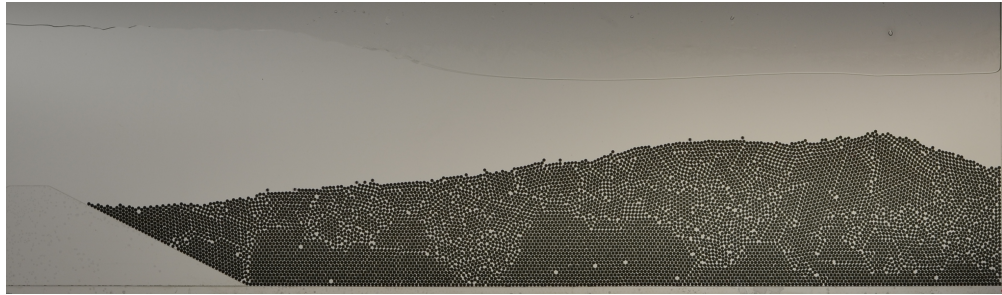
### 4.3 Analysis

Figure 4.1 shows snapshots from an exemplary measurement, which was the third of the 80 measurements conducted (see appendix D, table D.1). In this case the bed evolves from flat to a beach on the right side of the setup. This notion is however not sufficiently quantified. To get the details of the evolution of the bed during this measurement, the locations of the particles in each frame need to be known. Also, information concerning the amount of beach particles moved and the rate at which this happened are of interest. Therefore, a rigorous analysis was done using MATLAB. This analysis is explained next, and will be illustrated by figures obtained from measurement 3.

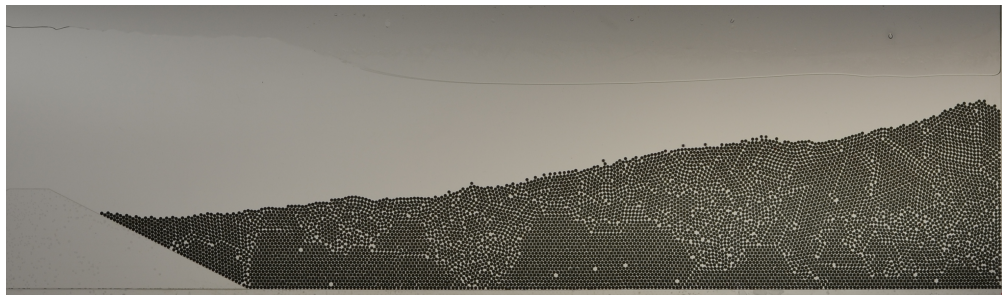
The time interval videos recorded were analysed using MATLAB. The details of the code used for this analysis can be found in appendix E. Firstly, a program was written to determine the locations of the centres of the beach particles in each frame. This code uses a MATLAB adaptation by Blair and Dufresne [8] of the IDL Particle Tracking software by Grier, Crocker, and Weeks [15]. Another program was written to determine which of the bed particles actually belong to the bed ‘surface’. The details of this program can be found in appendix section E.3. Essentially, the  $x$ -direction is divided into bins; the highest particle in each



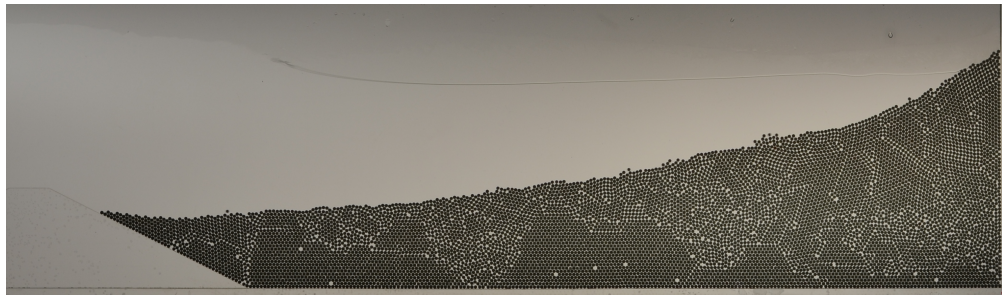
(a) 0 s



(b) 5 minutes



(c) 10 minutes



(d) 15 minutes



(e) 30 minutes

Figure 4.1: Snap shots of measurement 3, showing the creation of a beach.

bin is defined to belong to the beach surface.

Having this time-location data of the beach particles, different aspects can be investigated. A number of analysis examples are shown in figure 4.2. Fig. 4.2a shows the beach evolution, with the horizontal direction on the horizontal axis, time on the vertical axis and the vertical direction in colour. The part of the bed which emerged from the water is outlined in black. The horizontal magenta line indicates at what time the bed state switched from dynamic to quasi-steady, which will be further explained in section 4.3.1. The angle of the right-most one-third of the bed (‘eastern angle’) plotted against time in fig. 4.2b is an indication of beach formation. Fig. 4.2c shows an analysis of the initial bed. When investigating the reproducibility of a result, this analysis may be used to compare the initial beds. In this analysis, the flatness of the bed is quantified (‘normalised standard deviation’, which is the standard deviation of the bed surface particles divided by the linearised bed surface length, and ‘physical surface roughness’, which is the actual bed surface length divided by the linearised one) and a possible initial bed angle is determined. An analysis of the amount of transported sediment is shown in fig. 4.2d. The red part is sediment which was present in the first frame but is now gone, the green is newly deposited sediment. The tiny stars show the positions of their centres-of-mass. Fig. 4.2e shows a Voronoi tessellation of the final bed. Red means small cells or high density, blue means large cells or low density, yellow is in between. Note that only Voronoi cells with an area smaller than a certain cut-off area are taken into account, so the disproportionately large cells at the bed boundary are disregarded. This technique allows for detailed study of the bed structure, which will be treated more in detail in section 4.4.2.

### 4.3.1 Sediment transport

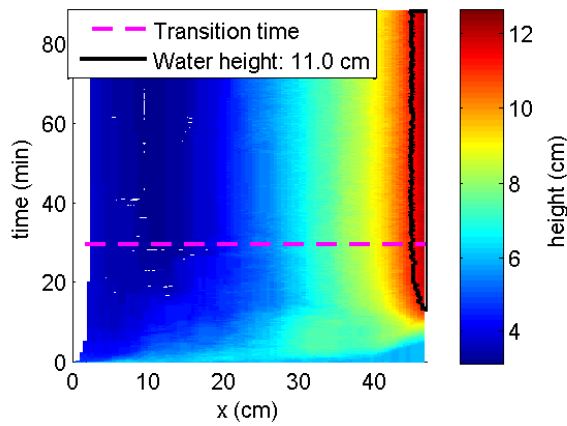
The amount of sediment transport taking place is an indication of the steadiness of the bed at a certain moment. It is therefore used to distinguish between the ‘dynamic’ and ‘quasi-steady’ state of an experiment. The bed characteristics at the moment at which the quasi-steady state is reached, will be used to categorise the measurement.

The analysis of sediment transport is illustrated by figure 4.3. Figure 4.3a shows the initial bed. Figure 4.3b shows the bed at the end of the measurement, in this example after 88 minutes and 10 seconds. The bed surfaces in all time frames are compared to the initial bed surface, resulting in a ‘negative’ part (red in figure 4.3b), which is the area of sediment having been present in the first frame but not anymore in the current one, and a ‘positive’ part (red in figure 4.3b), which is the area of sediment present in the current frame but not in the initial one. The little stars indicate the locations of the centres of mass of the negative and positive sediment areas. Figure 4.4a shows the negative and positive sediment areas as a function of time. Mass conservation may mislead one to the conclusion that both areas should be the same, but the rearrangement and compacting of the bed leads to a mismatch; *i.e.*, the negative and positive sediment areas may differ in particle density, which is reflected in a difference in total area. The bed density and changes therein are treated more in detail in section 4.4.2. The negative sediment was chosen to be used for further analysis, since this gives the best indication of actual bed evolution; in the case of minor sediment transport and bed rearrangement, the positive area may remain constant, but the evolution will still be visible in the negative area.

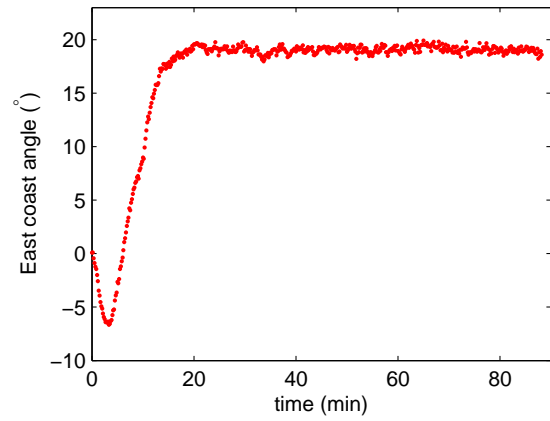
The distance between the centres-of-mass of the negative and positive sediment areas is the distance effectively travelled by the replaced sediment. This mean sediment replacement is shown in figure 4.4b. As both the area of the transported sediment and its replacement indicate bed evolution taking place, the product of the two is taken to serve as the parameter defining the state of the bed. This *cubical sediment transport* is shown in figure 4.4c.

### Cubical transport rate

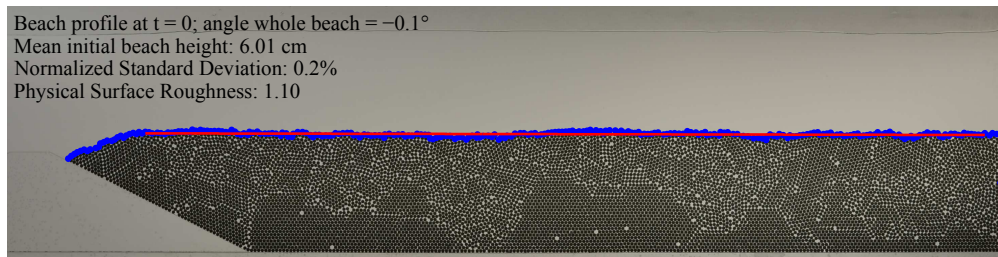
Important for the bed state is the rate at which the cubical sediment transport changes. Figure 4.4d shows the cubical transport rate (CTR), which is defined as the local time derivative of the cubical sediment transport. Note, that the CTR is expressed as distance cubed *per wavemaker period*  $T_{wm}$ , since the period of the wavemaker is the governing time scale in the experiment. It is determined for each time frame, by



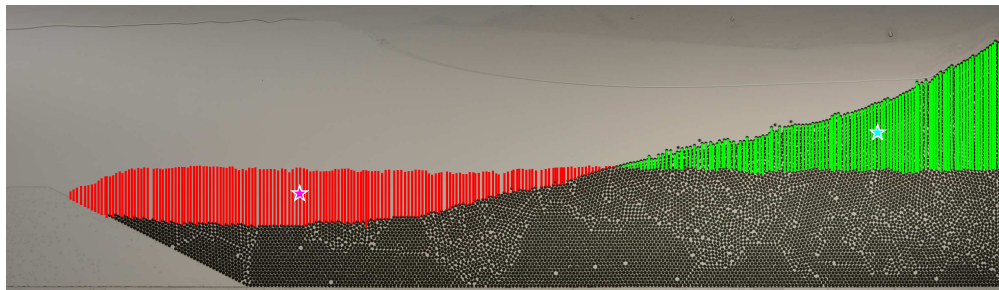
(a) Bed evolution analysis; colours indicate bed height, the black line indicates the part of the bed elevated from the mean water depth, and the dashed magenta line indicates the transition of the bed state to a quasi-steady one (see section 4.3.1).



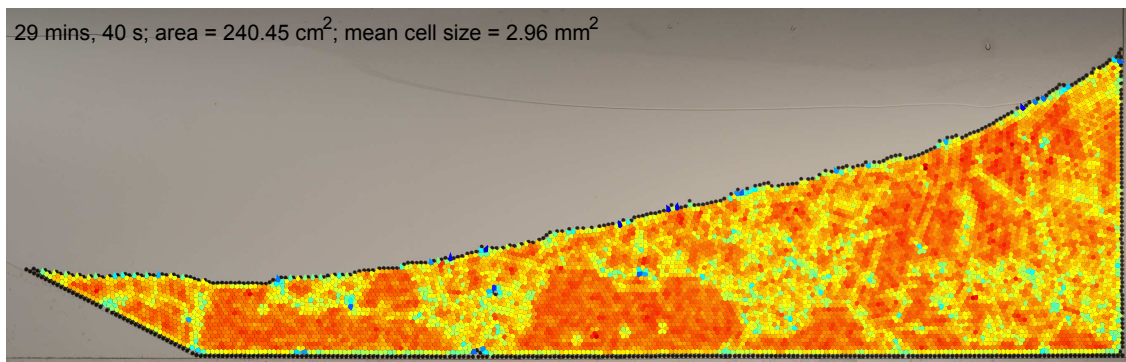
(b) Bed angle analysis, showing the angle of the 'eastern' (right-most, downstream) part of the bed. A non-zero angle indicates the presence a beach.



(c) Initial bed analysis; measurement of initial height, whole bed angle and roughness of the bed ('Normalised Standard Deviation' and 'Physical Surface Roughness').

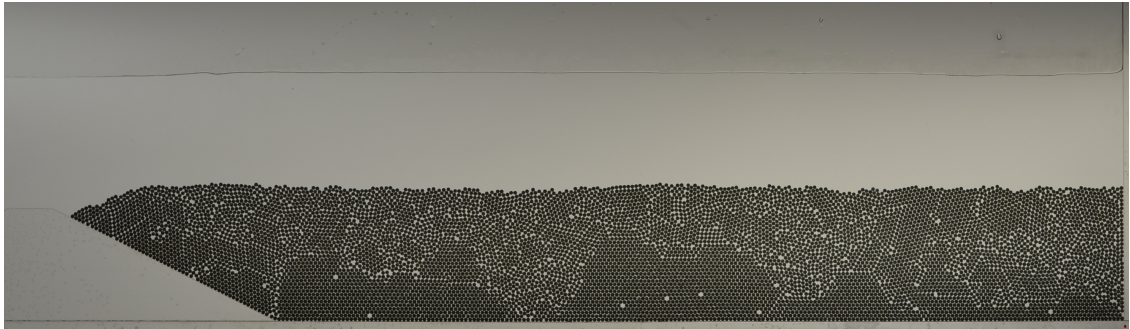


(d) Sediment transport analysis; green indicates redeposited sediment, red indicates where the redeposited sediment came from. Stars indicate the centres-of-mass of both areas.

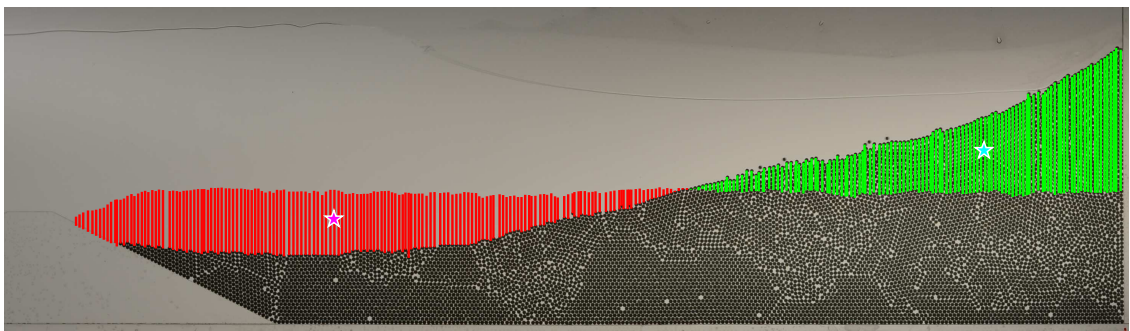


(e) Voronoi tessellation, which allows for a detailed study of the bed structure. Red indicates small Voronoi cells or high density, yellow and blue indicate larger Voronoi cells or lower density.

Figure 4.2: Analysis examples for the beach evolution measurement data.

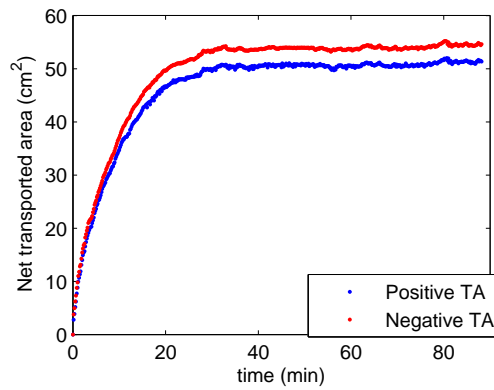


(a)  $t = 0$  s: initial bed

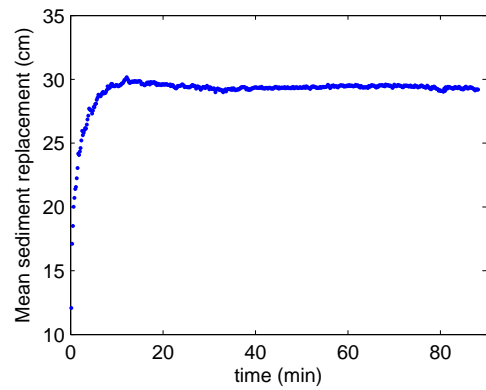


(b)  $t = 1$  h, 28 m, 10 s

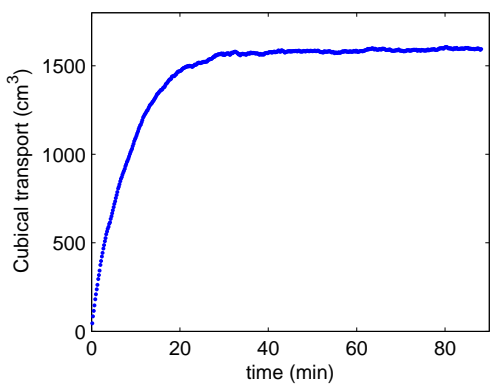
Figure 4.3: Sediment transport analysis. The coloured areas show the difference to the initial bed; the blue area indicates the ‘positive sediment’, which consists of redeposited particles, the red area (‘negative sediment’) indicates the sediment which was present in the first frame, but not anymore in the current one. The stars indicate the centres-of-mass of both areas.



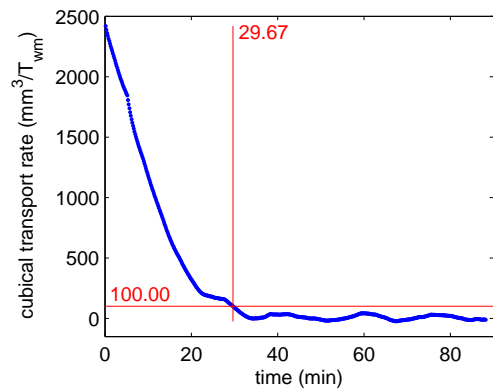
(a) Transported sediment area



(b) Mean sediment replacement: distance between centres-of-mass of positive and negative sediment parts



(c) Cubical sediment transport (replacement  $\times$  area)



(d) Cubical transport rate: time derivative of cubical sediment transport

Figure 4.4: Sediment transport: area, replacement, cubical transport and cubical transport rate.

taking the cubical sediment transport in a ‘linearisation window’  $t_{lin} = 10$  minutes around it, converting time to wavemaker periods, and making a linear fit through the points. *The transition of the bed state from dynamic to quasi-steady is defined to occur at that moment in time, after which the CTR does not reach a certain threshold rate  $R_{thresh}$  anymore.* This time is referred to as the *transition time* of the bed. Figure 4.4d illustrates this moment to be 29 minutes and 40 seconds for a threshold  $R_{thresh} = 100 \text{ mm}^3/T_{wm}$ .

This analysis is done for all 80 measurements performed. The resulting transition times are shown in figure 4.5. In this figure, white is the total measurement time, red is the time in which the bed is in the dynamic state, and purple indicates that the bed never reached a quasi-steady state. This means the measurement time was too short. Of the 80 measurements, only measurement nr. 53 is marked as too short. Due to time constraints, the measurements were chosen to run for 2 hours max, which was the case for this measurement.

### $R_{thresh}$ and $t_{lin}$

The moment at which a bed state is defined as changing from dynamic to quasi-steady is dependent on 2 chosen parameters: the cubical transport linearisation window  $t_{lin}$  and the CTR threshold  $R_{thresh}$ . In choosing the optimal quantities for both parameters, a number of things have to be considered.

Figure 4.6 shows some unexpectedly large and regularly-timed fluctuations in the CTR. These fluctuations are observed for practically all measurements. A detailed observation of the measurements showed the cause of these fluctuations: the imperfect timing of the camera shutter. Two different semi-states are observed for the bed within a single wavemaker period; a ‘quiet’ state, in which relatively few particles are detached from the bed, and a ‘violent’ state, in which a lot of movement takes place within the top layers of the bed and relatively many particles are detached from the bed. Since the timing of the camera is not perfect, sometimes the bed is photographed in the violent state, and sometimes in the quiet state. This appears to happen in cycles with a certain regularity, which are due to the unknown details of the camera shutter and/or timer. This regularity in time shift is reflected in the fluctuations of the CTR, since only particles which are not detached from the bed are observed during the analysis.

Secondly, a reasonable CTR threshold  $R_{thresh}$  needs to be chosen, while the CTR linearisation window  $t_{lin}$  should be chosen long enough to reduce the fluctuations to a reasonable limits, but short enough to still capture the important details of the CTR, *i.e.* the bed state transition. An  $R_{thresh}$  of  $100 \text{ mm}^3/T_{wm}$  has been chosen, which comes down to a sediment transport per wavemaker period of around 3 bed particles being transported 1 cm. At a CTR linearisation window  $t_{lin}$  of 10 minutes, this  $R_{thresh}$  is higher than the mentioned shutter-caused fluctuations. As an extra check, the measurement steady bed morphologies (sec. 4.3.2) determined both by human observation and by digital analysis have been compared. At  $t_{lin} = 10$  minutes, the humanly observed and digitally obtained morphologies match very well, while at higher  $t_{lin}$  the morphologies hardly change. Therefore,  $t_{lin}$  was chosen to be 10 minutes.

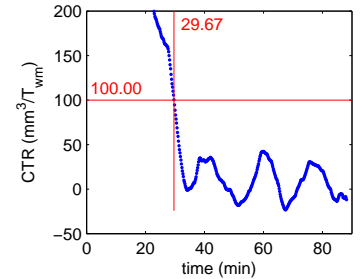


Figure 4.6: Oscillations in CTR; zoom of figure 4.4d.

### 4.3.2 Steady bed morphology (SBM)

The beach evolution analysis as explained in the previous section allows for a digital method of distinguishing between different evolution outcomes. Different bed morphologies were observed at the onset of the quasi-steady state, for example a dry beach emerging from the water on the right end of the setup, a dry dune forming in the middle of the bed, or a beach on the right which did not emerge from the water. Six such ‘steady bed morphologies’ (SBMs) can be distinguished: ‘Dry beach’, ‘Wet beach’, ‘Dune’, ‘Dune-beach’, ‘Significant transport’, ‘Quasi-static’ and ‘Suction’.

Each of the six SBMs was first qualitatively defined by its apparent characteristics. After that, the definitions were quantified to be able to be recognised by a computer. The steady bed morphologies and their definitions and quantifications are summarised in table 4.2. Each defined SBM will be treated in more detail next.

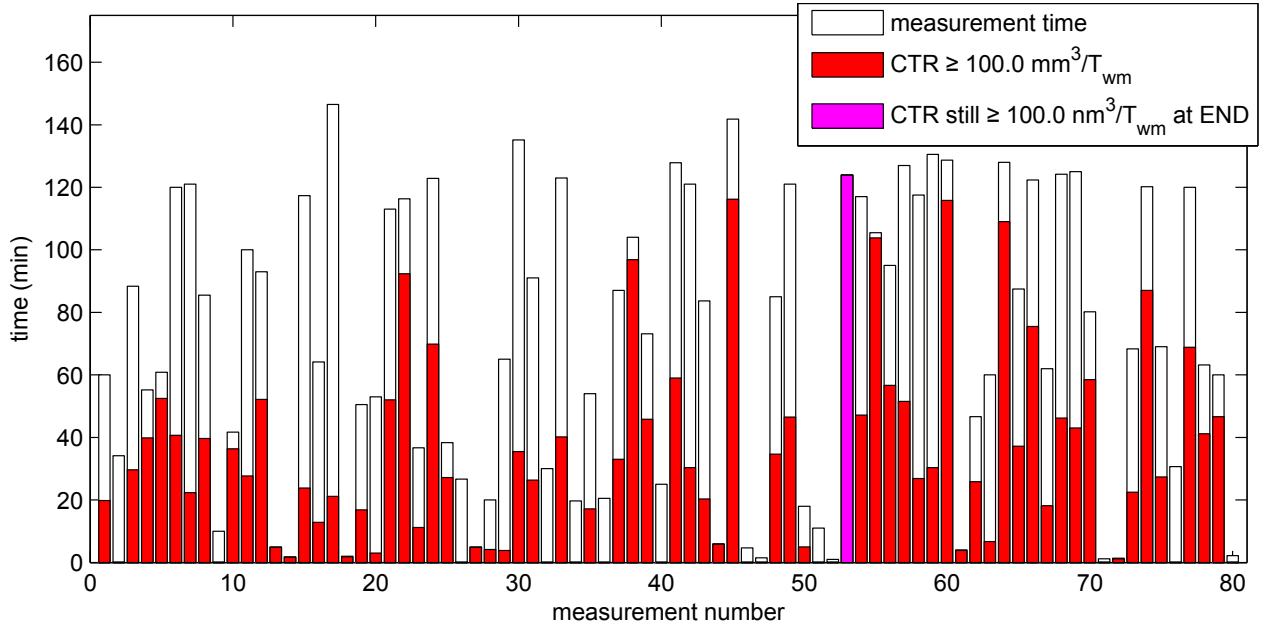
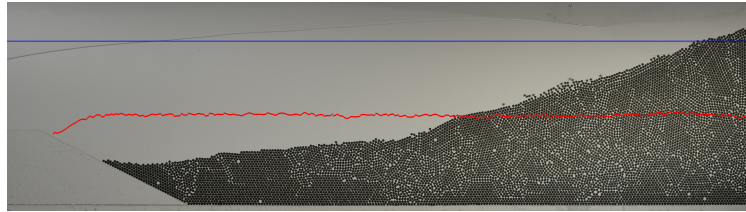


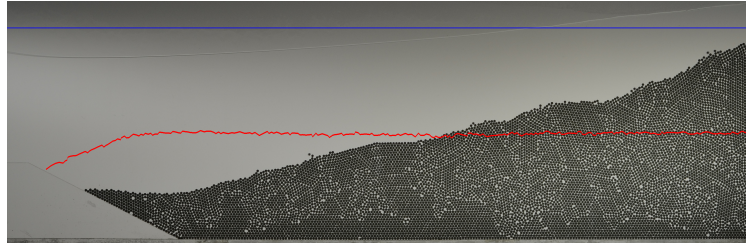
Figure 4.5: Bed state transition times: white = total measurement time, red = time in dynamic state. Purple indicates the bed never reached a quasi-steady state. Measurement numbers relate to the measurements in appendix D, tables D.1 and D.2.

SBM	Definition	Quantification
Dry beach	Beach emerges from water on right side of setup	Right end of the bed $>$ static water level (dry), bed maximum close to right setup end
Wet beach	Like dry beach, but now the bed does not emerge from water	no dry bed parts and $\theta_{\text{east}} > 5^\circ$
Dune	Bed emerges from water, but not on the far right of the setup	Some part of bed is dry, and it is not the right end
Dune-beach	Beach emerges from water, but has a dune-like structure	Right end of the bed dry, but bed maximum $>$ 5 cm away from right setup end
Significant transport	A significant amount of sediment transport is taking place, but none of the above is observed	No dry parts and replaced sediment $\geq 10$ cm <sup>2</sup>
Quasi-static	Hardly any sediment transport is taking place	No dry parts and less than 10 cm <sup>2</sup> replaced sediment
Suction	Lots of particles get sucked to wavemaker-part of setup	measurement time $<$ 20 min. and more than 90 particles lost

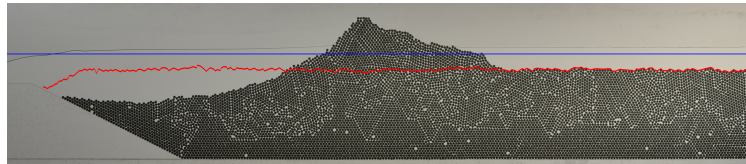
Table 4.2: Steady bed morphologies of the beach evolution experiment and their quantifications.



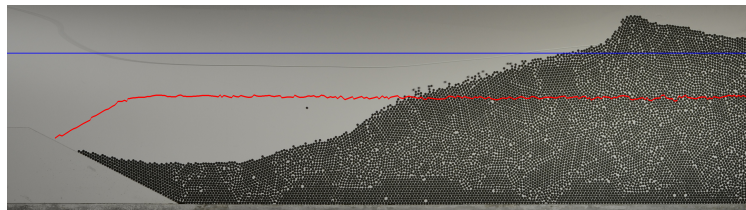
(a) Dry beach: bed emerges from water at downstream end of the setup.



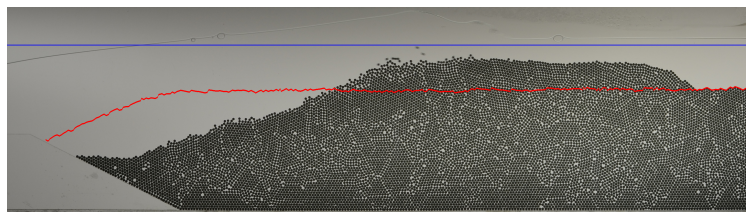
(b) Wet beach: beach with no part of the bed emerged from the water.



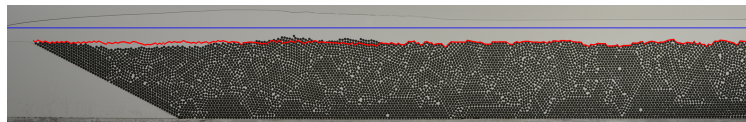
(c) Dune: bed emerges from water before reaching end of the setup.



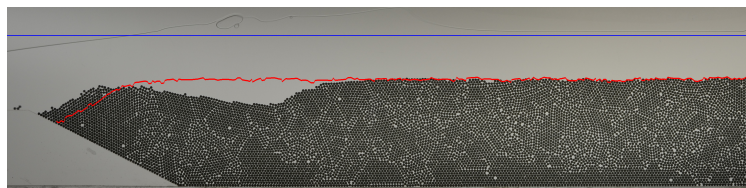
(d) Dune-beach: intermediate from between dry beach and dune.



(e) Significant transport: no emersion from the water.



(f) quasi-static: almost no evolution of the bed.



(g) suction: large number of bed particles sucked to the wavemaker.

Figure 4.7: Snapshots of all 7 different steady bed morphologies. red line = initial bed surface, blue line = static water height.

### Dry beach

A dry beach is shown in figure 4.7a. In this SBM, the downstream part of the bed rises out of the water during at least part of each wavemaker period. Since the free water surface is hard to detect, a bed surface part is defined to be ‘dry’ if the height of it is higher than the mean water depth  $H_0$ . Additional to any part of the bed being dry, it has to be the most *downstream* part that is dry for the SBM to be a dry beach. This feature is defined to be met if any one of the 10 most downstream particles of the bed surface is dry. Additionally, the bed maximum has to be close to the right-most (downstream) end of the setup. If the bed maximum is more than 5 cm upstream of the setup end, the bed will instead be categorised as a dune-beach (see next page). All dry beaches observed are further characterised by a gentle slope of the bed, resulting in a positive eastern bed angle of the order  $10^\circ$ .

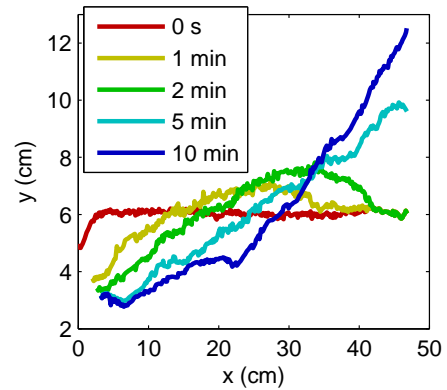


Figure 4.8: Typical bed evolution of a dry beach; water depth 11 cm.

### Wet beach

A wet beach is shown in figure 4.7b. The wet beach has the same gentle slope upward to the rightmost end of the bed, but is different from a dry beach in that no part of the bed is dry. Therefore, an SBM is recognised as a wet beach if no part of the bed is dry and the eastern angle is larger than  $5^\circ$ .

### Dune

Figure 4.7c shows a dune. This SBM is characterised by a hump in the bed rising out of the water, while a free water surface is present both up- and downstream of this hump. Usually, the left-most part of the dry dune has a steep cliff, leading up to the bed maximum, while right of that maximum the bed has a gentle negative slope.

For an SBM to be categorised as a dune, part of the bed has to be dry. Also, this cannot be the most downstream part of the bed, as this would make it a dry beach.

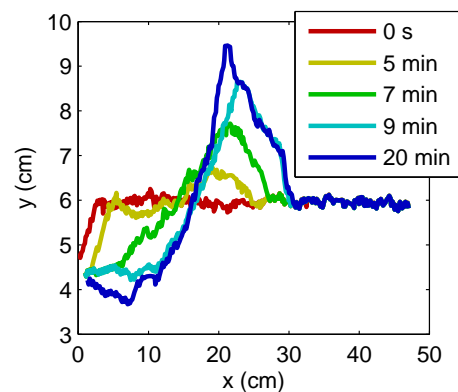


Figure 4.9: Typical bed evolution of a dune; water depth 7 cm.

### Dune-beach

Figure 4.7d shows a dune-beach. In this SBM, the right-most end of the bed is dry, like the case is for a dry beach. However, the structure of the bed looks very much like that of a dune, with usually a steep cliff leading up to the dry bed maximum, and a gentle negative slope right of that maximum.

An SBM is marked to be a dune-beach when the right-most end is dry like a dry beach, but the bed maximum is more than 5 cm left (upstream) of the right-most end of the setup. Note that *any* SBM containing a dry bed part, is either a dry beach, a dune or a dune-beach.

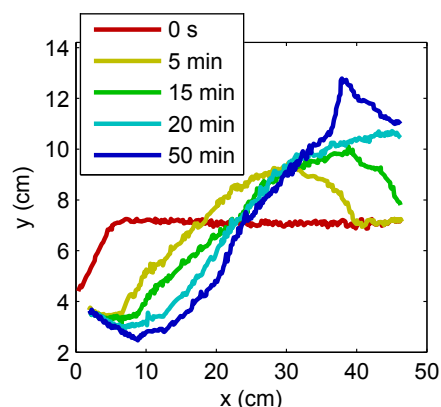


Figure 4.10: Typical bed evolution of a dune-beach; water depth 10 cm.

### Significant transport

Figure 4.7e shows the significant transport SBM. In the significant transport SBM, no beach, dune or dune-beach is present, but still a considerable amount of sediment transport has taken place. The SBM has to meet the following criteria to be characterised as significant transport: no part of the bed is dry, the eastern angle is smaller than  $5^\circ$  and more than  $10 \text{ cm}^2$  of sediment has been replaced as compared to the initial bed.

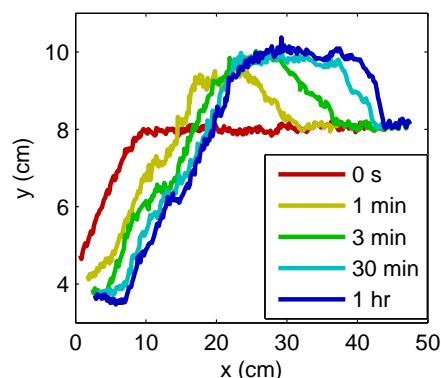


Figure 4.11: Typical bed evolution of significant transport; water depth 11 cm.

### Quasi-static

Figure 4.7f shows an SBM categorised as quasi-static. This SBM is reached when the bed hardly changes at all during the course of the measurement. It is characterised by no dry bed part, an eastern angle smaller than  $5^\circ$  and less than  $10 \text{ cm}^2$  of replaced sediment.

### Suction

Figure 4.7g shows a suction bed morphology. As may be clear from this figure, a lot of sediment is ‘missing’ from the bed at the end of the measurement. In fact, this sediment has been sucked to the wavemaker part of the setup, thus endangering the wavemaker and bed particles to being damaged. In order to prevent this from happening, the measurements where heavy suction occurred had to be ended rather quickly (within the order of minutes). Therefore, the outcome of a measurement is categorised as suction when the total measurement time is less than 20 minutes and the total number of particles ‘lost’ within this time is greater than 90.

Note, that in the suction case, strictly speaking no steady bed morphology is reached, since the measurement is terminated before the bed reaches a quasi-steady state. For the sake of readability, however, the suction

outcome will be referred to as a measurement's SBM.

## 4.4 Results

### 4.4.1 Phase diagrams

Based on the steady bed morphologies defined and described in section 4.3.2, a MATLAB program was written, see appendix E.6. This program goes through all measurement data, establishing the SBM of each measurement.

The resulting phase diagrams for all four initial bed heights  $B_0$  are shown in figures 4.12 and 4.13. Especially when looking at the 3D phase diagram, some form of 'grouping' of the SBMs becomes quite clear. Dunes are most likely to be generated at a water layer depth ( $H_0 - B_0$ ) of 1 cm, dune-beaches at 3 cm, dry beaches at 5 cm and wet beaches at 7 cm. For the different SBMs, this can be explained as follows.

#### Dunes

A typical dune formation (see fig. 4.9) starts with an initial heap of newly transported sediment being formed just behind the wedge. Next the heap starts moving downstream and growing, until at some point it reaches the free surface. Due to the small water layer depth this typically happens before the heap can reach the right-most end of the setup. It then effectively forms a dune with the waves coming in from the left (upstream) and a small, relatively 'calm' lake on the right (downstream). The free surface of this lake will still be moving up and down slowly, due to the porous structure of the bed.

#### Beaches

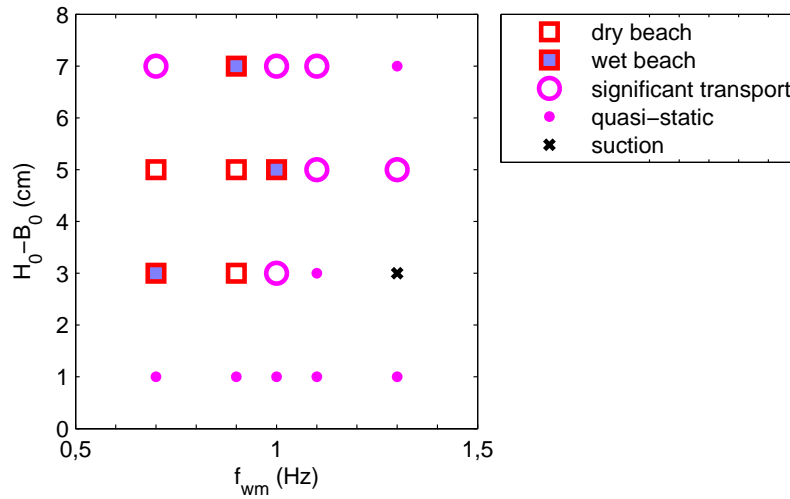
At deeper water layers, the heap does travel all the way to the end of the setup, and keeps growing there until the maximum stable beach angle has been reached (see fig. 4.8). This stable angle differs a lot between measurements; see figure 4.14. Note that most beaches 'settle' within the first hour, but some (low lines in figure 4.14) take more time. The initial dip in the angle is caused by the fact that a heap travelling downstream causes a negative slope in the right part of the bed just before it reaches the end. As expected, all stable angles are lower than the theoretical angle of repose for monodisperse circles as mentioned by Albert, Albert, Hornbaker, Schiffer, and Barabási [2]. Most stable angles are between  $10^\circ$  and  $20^\circ$ , even lower than the  $24 \pm 1^\circ$  for disks found by Cantelaube, Limon-Duparcmeur, Bideau, and Ristow [12], and the  $\sim 22^\circ$  found for glass and polystyrene beads according to Albert et al. [2]. A relation between the final beach angle and the measurement parameters has yet to be found. Sometimes, the water layer is shallow enough for the beach to emerge from the water, which makes it a dry beach. Other times, the water layer is just too deep, in which case the beach stays submerged, making it a wet beach.

#### Dune-beaches

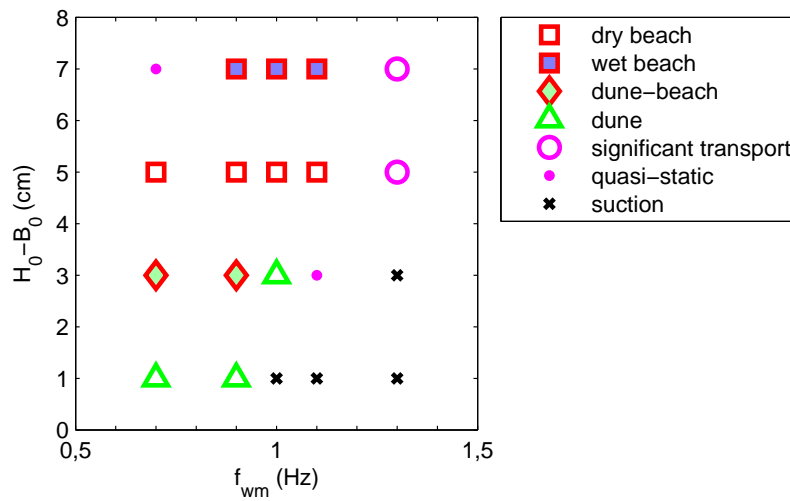
The dune-beach appears as a transition form between the beach and dune regions of the phase space. One might suspect a dune-beach to form like a dune, emerging close to the setup end due to the increased water layer depth, and then slowly to move downstream, thus growing until even the 'back' of the dune has risen from the water. This is not the case, as is illustrated by figure 4.10; first the bed evolves like any other dry beach, but once it reaches the water surface (here at  $t = 10$  min, 30 s) it 'switches' to a dune-like evolution, giving a rising bed upstream from the setup end, ending in a sharp cliff. This evolution has been observed for all 6 dune-beach cases.

#### Suction

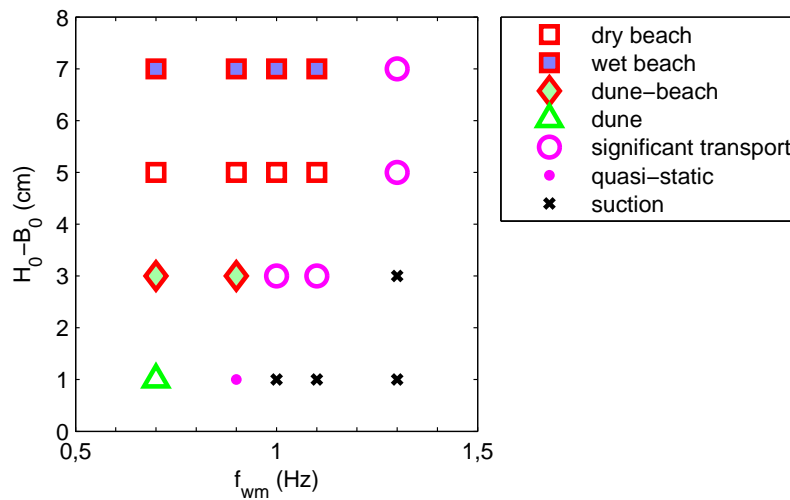
Suction SBMs are clearly grouped in the high frequency, low water layer depth corner of the phase space. In suction, strong upstream (left-ward) sediment transport occurs. Considering this, it may come as no surprise, that the suction part of the phase space is separated from the beach and dune parts by a layer of quasi-static and significant transport SBMs. In this layer, the downstream forces on the bed are (almost) cancelled by the upstream forces, which reduces the potential for sediment transport significantly.



(a)  $B_0 = 50$  mm

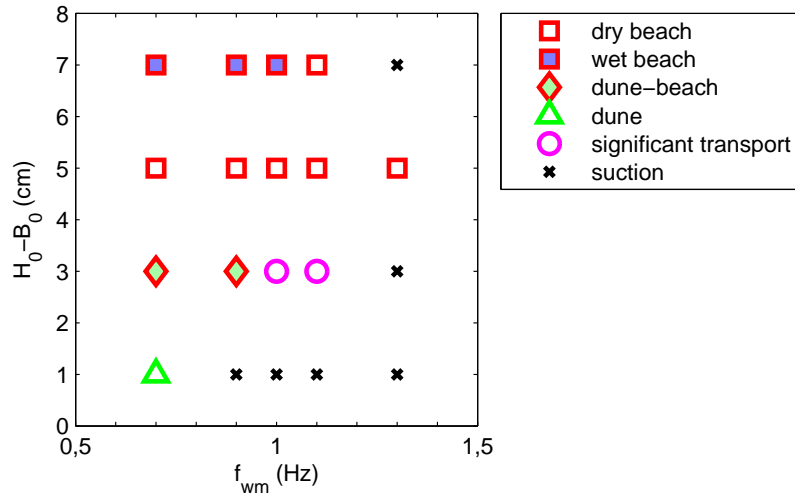


(b)  $B_0 = 60$  mm

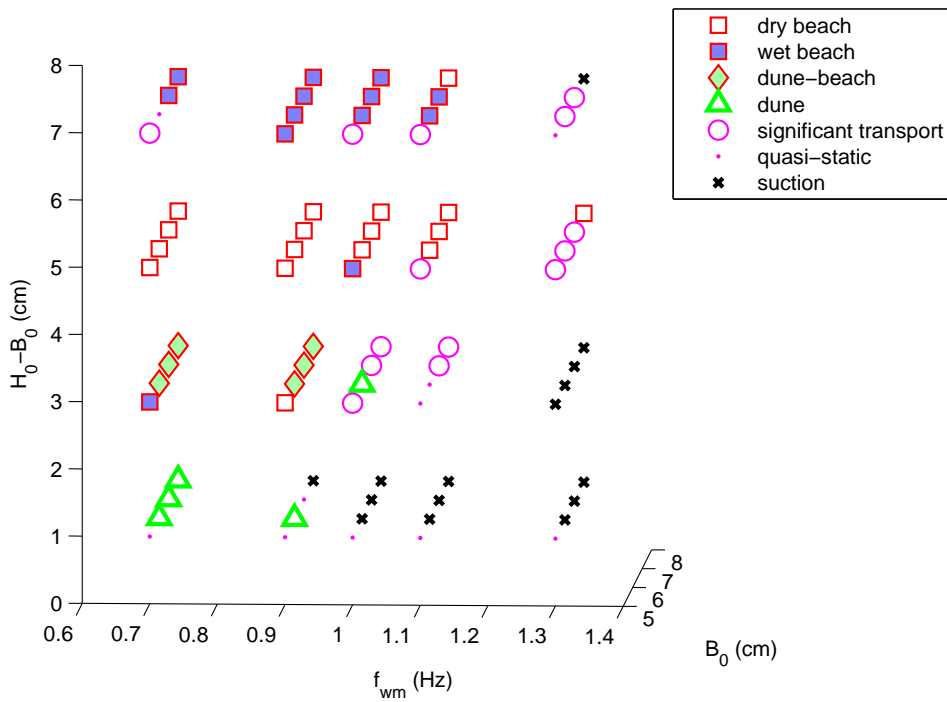


(c)  $B_0 = 70$  mm

Figure 4.12: Phase diagrams for  $B_0 = 5, 6$  and  $7$  cm. The different symbols indicate the different steady bed morphologies occurring for different measurement parameters.



(a)  $B_0 = 80$  mm



(b) 3D Phase diagram

Figure 4.13: Phase diagrams continued:  $B_0 = 8$  cm and 3D of all SBMs.

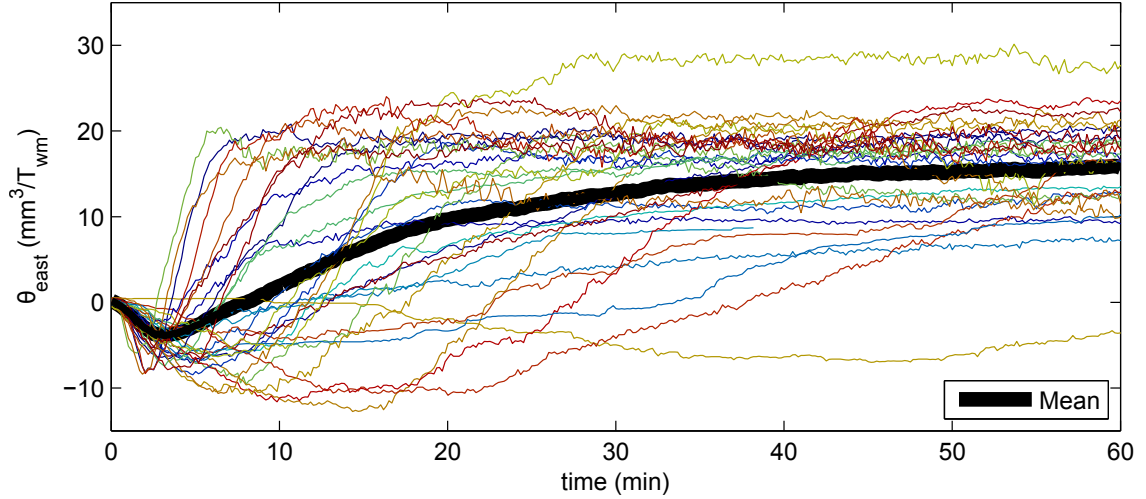


Figure 4.14: First hour of eastern bed angles of all dry and wet beaches observed.

### Bed activity

Furthermore, an increase in activity of the bed can be seen with increasing initial bed height  $B_0$ . For  $B_0 = 5$  cm, only a in few of the measurements enough sediment transport was happening for beaches to be formed, while no dunes or dune-beaches were observed. Suction was only reported in one case. For higher initial bed heights, dunes and dune-beaches are formed and more beaches are created, but also more instances of suction were observed.

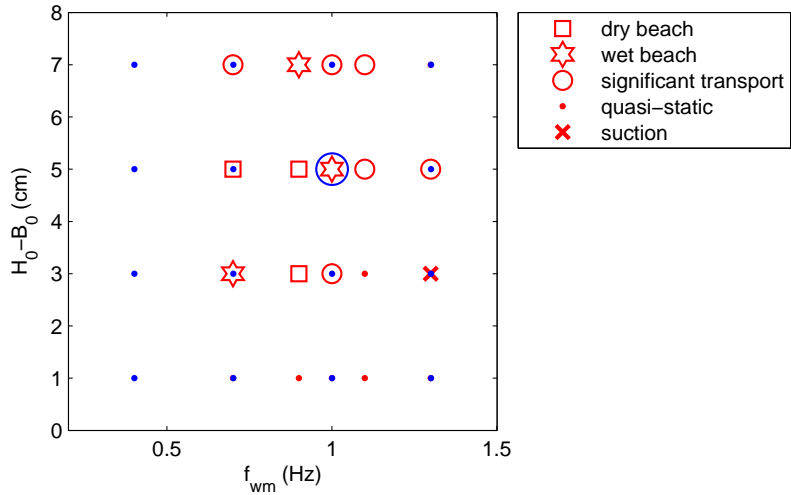
### Comparison to precursory measurements

Figure 4.15 shows combined phase diagrams for the two initial bed heights which were investigated in both the precursory and new measurement series. The SBMs of the ‘old’ measurements are depicted in blue, those of the new measurements in red. A significant difference in bed activity can clearly be seen. For  $B_0 = 5$  cm, all the old SBMs were quasi-static except for the significant transport at  $f_{wm} = 1$  Hz and  $H_0 - B_0 = 5$  cm. In the new measurements however, some dry beach and significant transport SBMs (and a single occurrence of suction) were obtained for parameters where the old measurements found only quasi-static SBMs, while a wet beach was found at  $f_{wm} = 1$  Hz and  $H_0 - B_0 = 5$  cm. For  $B_0 = 8$  cm, the difference in bed activity seems less, but is still visible. Two of the beaches found in the new series were quasi-static SBMs in the old one, and at  $H_0 - B_0 = 3$  cm where dune-beaches, significant transport and suction was found, the old measurements only reported significant transport. Interestingly, no suction was observed in the old measurement series. Two reasons for this, which may also be the reasons for the difference in bed activity as a whole, might be the difference in wavemaker motion between the old and new measurements, and the fact that the wavemaker was placed  $\sim 13$  mm further away from the bed in the old measurements. Both of these effectively reduced the proximity of the wavemaker to the bed. More details about this can be found in appendix C.

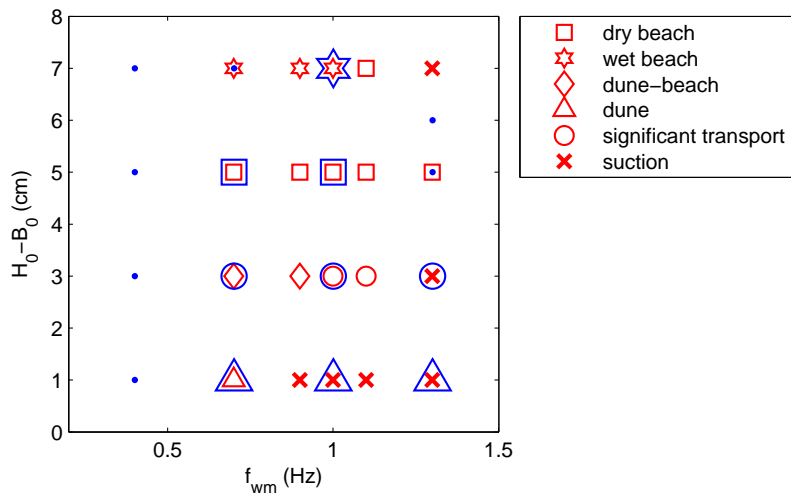
### 4.4.2 Bed structure

One might wonder what happens to the density of the bed during the measurements. Does the bed get packed more loosely, or more densely? Or does the packing change at all? Is the transported sediment repositioned more loosely or more densely? What happens to the density of the part of the bed which does not appear to be repositioned at all? Information about the bed density, or packing fraction, which may shed light on these matters was obtained using Voronoi tessellation.

The packing fractions of the whole bed of all measurements are shown in figure 4.16a. From this graph it seems that the packing fraction of each bed is rising during the measurement. Eventually, the packing fractions are expected to reach a certain horizontal maximum, at a close packing fraction value somewhere



(a)  $B_0 = 50$  mm



(b)  $B_0 = 80$  mm

Figure 4.15: Combined phase diagrams of old and new measurements, for  $B_0 = 5$  and 8 cm. Precursory measurement results are in blue, new measurement results in red.

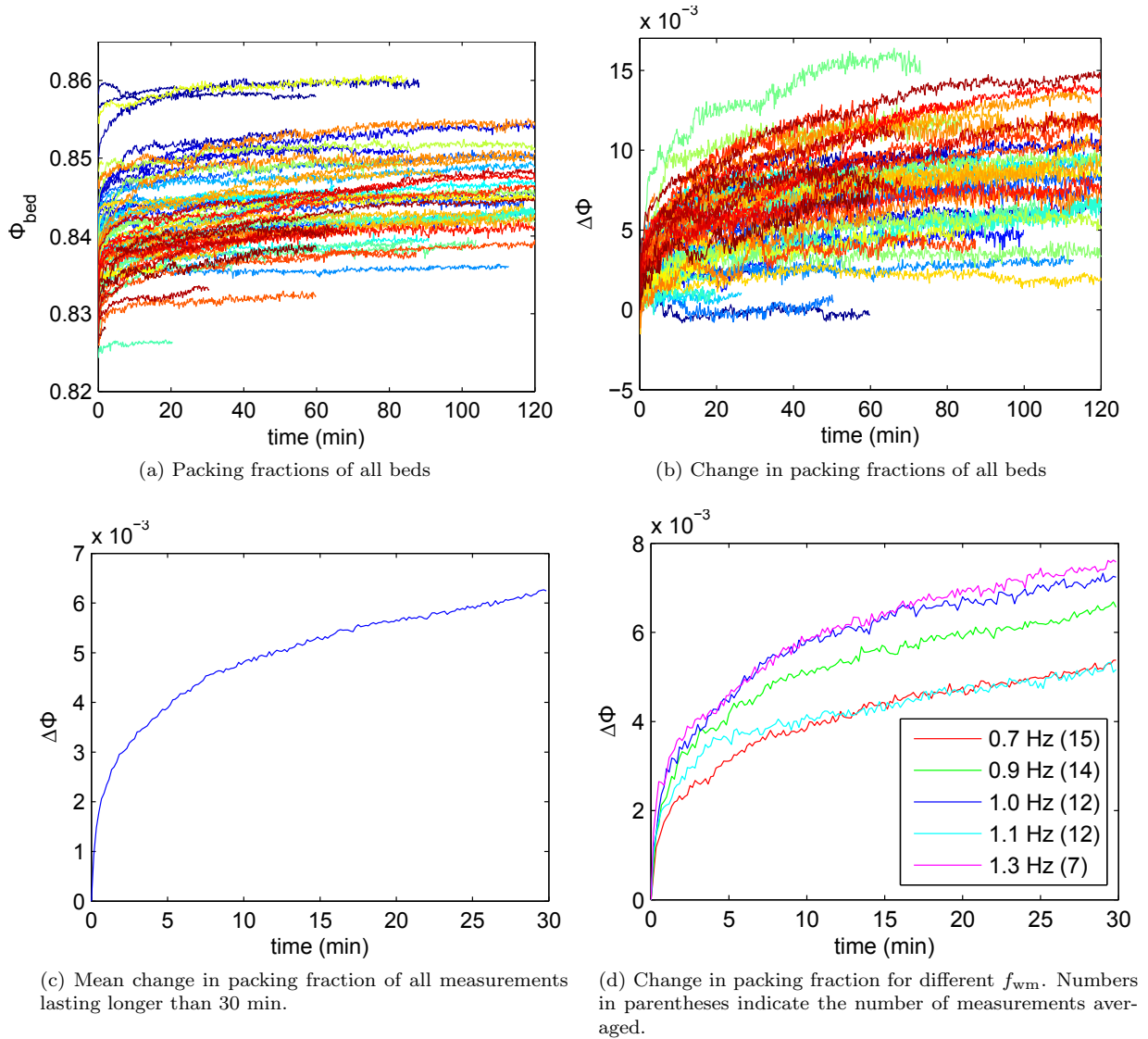


Figure 4.16: Evolution of the packing fraction of the whole bed.

below the theoretical 2D maximum packing fraction for circles  $\pi/\sqrt{12} \approx 0.91$ . Note that all bed packing values are larger than the random (loose) packing fraction for circles of 0.82 as obtained numerically by Kausch, Fesko, and Tschoegl [19]. The slope of the evolving packing fractions indicates that this may take a while and will certainly happen on a different timescale than the duration of the measurements. The differences in initial packing is caused by the fact that the beds had to be manually prepared. Therefore, it is more useful to look at the *change in packing fraction* during the measurements. Figure 4.16b shows the change in packing fraction as compared to the initial bed for all measurements. Here the trend of a rising packing fraction is even more clear. The mean of bed packing fraction evolutions depicted in figure 4.16c indicates the existence of two regimes in the rate of change of the packing fraction; an early regime with a high packing rate for  $0 \leq t \lesssim 5$  minutes, and a long-term regime with a relatively low packing rate for  $t \gtrsim 10$  minutes. The existence of these regimes might be explained as follows. First of all, the incoming waves act as a shaker of the bed. This effective shaking will keep rearranging the bed until it reaches (possibly parameter-dependent) random close packing. This continuous packing is reflected in the second, long-term time regime. The initial bed however was arranged *manually* in static water. This allows for the presence of very unstable, loose packed regions within the bed, which are likely to collapse when the first waves hit the

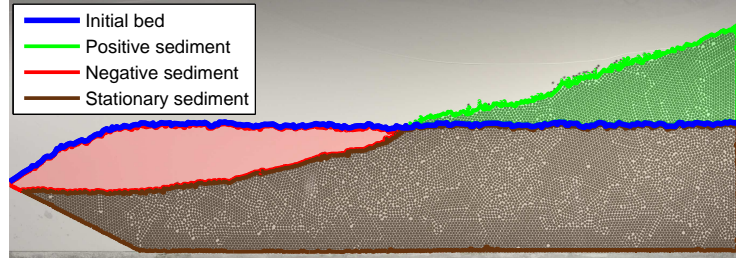
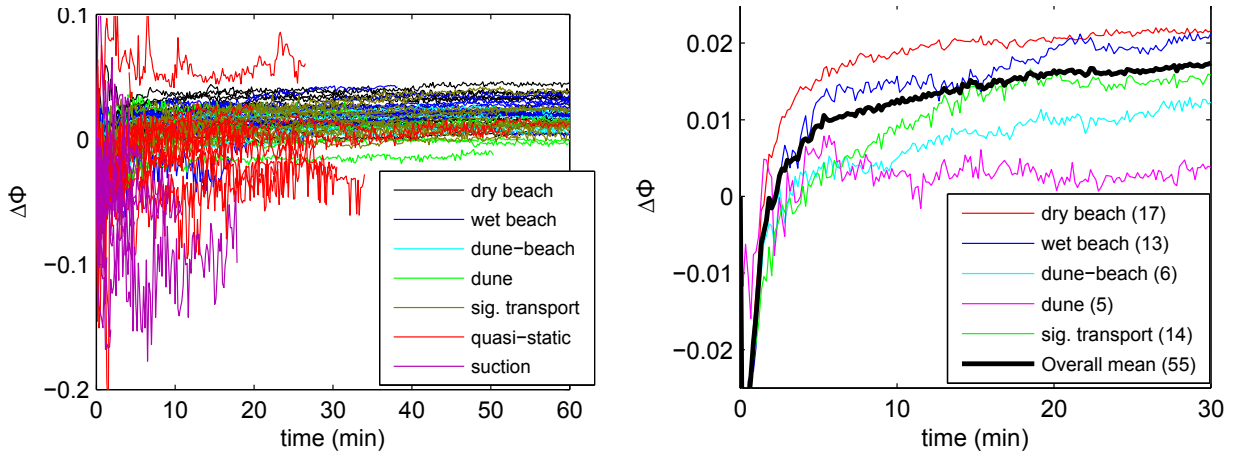


Figure 4.17: Different parts of the bed, with the initial bed profile in blue. Positive sediment: the part which was not there initially but is there now; Negative sediment: the part which was there initially but is not there anymore; Stationary sediment: the part of the bed which contained particles initially and now still.



(a) All measurements; coloring by SBM. Note the relatively chaotic behaviour of the quasi-static and suction SBMs.

(b) Mean of different SBMs; numbers in parentheses indicate the number of measurements averaged.

Figure 4.18: Difference between the packing fractions of the positive and negative sediment bed parts.

bed. This would be reflected in a high initial packing rate, as observed. Note, that this behaviour in packing fraction was also found by Barker and Mehta [5], who did numerical simulations on periodical shaking of frictionless, hard spheres with a small amount ( $< 10\%$ ) of polydispersity. They explained this to be caused by the "structural rearrangements (...) driven by two relaxation mechanisms (...) – the faster relaxation corresponding to the motion of independent particles, and the slower to the motion of clusters" [5, p. 186].

Figure 4.16d shows the mean change in packing fraction for different wavemaker frequencies. One would anticipate higher frequencies to act as more intense shakers, resulting in a rise in packing fraction with wavemaker frequencies. The packing fraction evolutions of most frequencies seem to follow this behaviour. The change in packing fraction of  $f_{wm} = 1.1$  Hz however, is significantly lower than expected. More research would be necessary to clarify this behaviour.

For a slightly more detailed study of the packing fraction, the bed can be divided into three parts as illustrated by figure 4.17. The positive (PS) and negative sediment (NS) parts were already defined in the section about sediment transport, 4.3.1. The 'stationary' sediment (SS) at a certain time  $t$ , is defined as that part of the bed which contained particles initially, and still at time  $t$ . In essence, it is the region of overlap of the initial bed and the bed at time  $t$ . Figure 4.18a shows the difference between the packing fractions of the positive and negative sediment for all measurements. The packing fraction differences of the suction and quasi-static SBMs behave rather unpredictable. In these measurements there is only little positive sediment generated.

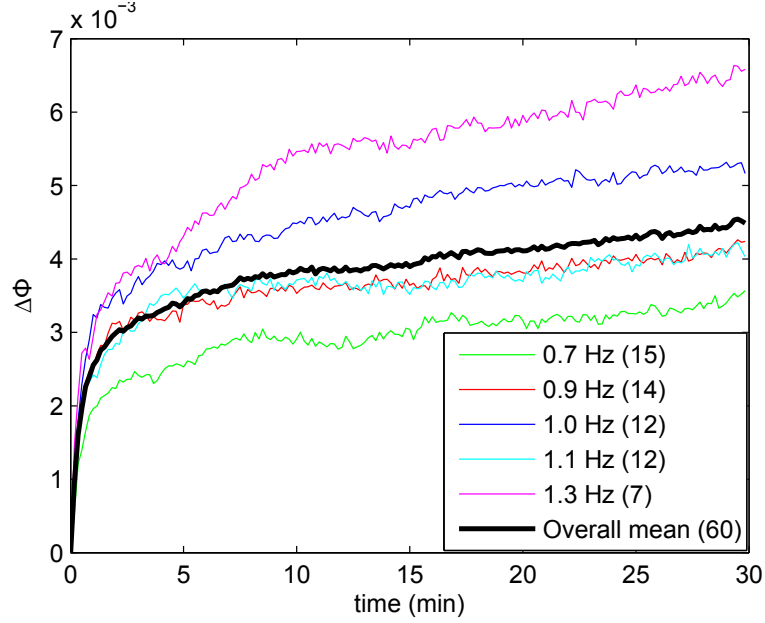


Figure 4.19: Mean change in packing fraction of the stationary sediment (see fig. 4.17) of all measurements lasting longer than 30 min. Different colors show means for different  $f_{wm}$ ; with the total mean in black. Numbers in parentheses indicate the number of measurements averaged.

The relatively small amount of particles in their PS causes the large fluctuations; therefore, no conclusions can be drawn based on these  $\Delta\Phi$  evolutions. The means of the other 5 SBMs are depicted in figure 4.18b. The beach SBMs give the highest density difference, while the dune-beaches and dunes give the least increase in density. During dune formation, typically part of the dune (which is part of the PS) is dry continuously. The observed sturdiness of these parts gave rise to the suspicion that a significant number of the particles in the dune may be sticking to the glass walls due to the presence of capillary bridges. This would also explain the relatively low packing fraction of the dune-like SBMs shown in figure 4.18b: the capillary bridges would prevent the particles from rearranging further, thus effectively keeping the packing fraction lower. Since the actual presence of these capillary bridges has not been the focus of this study, this needs to be further investigated.

A change in packing fraction of particles being picked up and repositioned may not be very surprising. But what happens to the part of the bed which seems not to be replaced at all? Figure 4.19 shows the change in packing fraction for the stationary sediment part of the bed (see fig. 4.17) for different wavemaker frequencies  $f_{wm}$ . Since the packing fractions of all stationary sediment parts show a similar distribution about the mean as that of the entire bed (fig. 4.16a), only the means were plotted. The black line shows the total mean. Although it does not reach the same amplitude of the difference in packing fraction between the positive and negative sediment parts (fig. 4.18b), it still proves to be a significant contribution to the evolving packing fraction of the entire bed (fig. 4.16c). Furthermore, again some correlation between packing fraction and  $f_{wm}$  seems to be present. However, like with the whole bed (figure 4.16d), also in the case of the stationary sediment the change in packing fraction at a frequency  $f_{wm} = 1.1$  Hz is unexpectedly low.

## Dunes

As shown in the phase diagram figure 4.13b, 5 dunes in total have been observed. In figure 4.20a a Voronoi tessellation of one of these is shown. Although the entire dune exists of re-deposited sediment, a clear difference in density can be observed between its left and right half. The position of the PS centre of mass, determined originally for the analysis of sediment transport, can be re-used to distinguish between the left and right half of the dune. Figure 4.20b shows the difference in packing fraction between the left and right dune halves,  $\Phi_{left} - \Phi_{right}$ , averaged over the 5 observed dunes. Note that this difference is of the same order

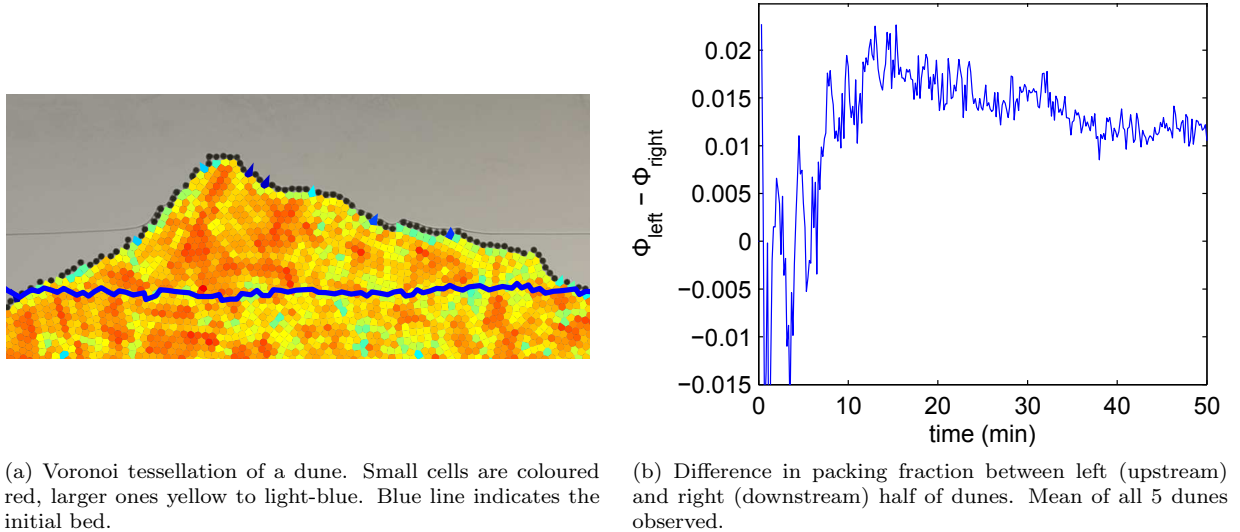


Figure 4.20: Differences in internal dune packing.

of magnitude as the difference in PS and NS packing fractions (fig. 4.18b) and even larger than the mean change in packing fraction in the whole bed (fig. 4.16c). This may be caused by the fact that the left, upstream half of the dune is continuously subjected to the compressing forces of incoming waves, on the right, downstream side the water is almost static. The unexpected maximum of packing fraction difference somewhere around 15 minutes has yet to be explained.

#### 4.4.3 Reproducibility

The reproducibility of the obtained results can be evaluated by looking at three different aspects. First of all, the phase diagram figure 4.13b shows clearly distinct regions in phase space for the different SBMs found. If the measurements had been less well repeatable, the phase diagram would have contained more ‘unexpected’ SBMs and would therefore have been more chaotic. Secondly, the comparison of the new and old measurements showed some disagreement. However, the cause of the differences was well explainable, and taking the relative difference in bed activity into consideration the agreement between the two measurement sets is clear. Thirdly, a total of 5 measurements have been performed twice; two in the old measurement series, and three in the new. All 5 resulted in the same steady bed morphologies the second time.

### 4.5 Conclusions and discussion

The 80 measurements performed show some interesting features of bed evolution under single-frequency generated waves. The 3D phase diagram in figure 4.13b summarises the variety in observed phenomena for different values of water layer depth ( $H_0 - B_0$ ), wavemaker frequency  $f_{wm}$  and initial bed height  $B_0$ . The water layer depth proves to be the most dominant parameter to determine the steady bed morphology type; dunes were observed at small water layer depths (around 1 cm), beaches at larger depths ( $\gtrsim 5$  cm), and a hybrid-like dune-beach at an intermediate water layer depth (3 cm). The general activity of the bed seems to be determined by  $f_{wm}$  and  $B_0$ . The least transport was observed at  $B_0 = 5$  cm, while at larger  $B_0$  significantly more transport was observed. Note that the height (5cm) of the fixed wedge between wavemaker and bed correlates with the most pronounced ‘jump’ in activity, which was even more clear in the results of the precursory experiments (see appendix C). Concerning the wavemaker frequency, especially the measurements at  $B_0 = 5$  and 7 cm suggest a slight optimum in terms of transport at an  $f_{wm}$  of approximately 0.9 Hz. Furthermore, the analysis of the bed structure shows that the packing fraction of the bed increases continuously during the measurement. This is partly caused by the fact that transported particles are redeposited in a more compact configuration than they used to be in initially. However, the packing fraction of the part of

the bed which is not redeposited also increases; the ‘stationary’ sediment is not completely stationary after all. In dunes, a significant difference in packing fraction between the up- and downstream halves was found. This might be caused by the continuously incoming waves on the left, while the right is subject to almost static water. Lastly, the observed bed morphologies are quite reproducible: the phase diagram 4.13b shows clearly distinct SBM regions, the phase diagrams of the old and new measurements agree well except for an explainable difference in bed activity, and the few measurements which were repeated all had identical SBMs the second time.

Some things still remain unclear. How the stable beach angles shown in figure 4.14 depend on the measurement parameters, for example, needs to be further investigated. Also the value of close packing fraction of the bed may be of interest, although this will be different when using particles with a different size distribution. A correlation between wavemaker frequency and packing fraction evolution was expected, but the measurements show unexpected behaviour (fig. 4.16d). Further examination would be needed to explain this. Also, the performed measurements provide enough data to investigate possible localised repositioning of the bed, *i.e.* the whether certain parts of the bed become more compact or reposition quicker than other parts. The author excuses himself for the absence of this kind of analysis, which was due to the lack of time available. Lastly, although in quite a number of cases a possible explanation was given for the observed phenomena, many of these may have to be investigated further in order to be confirmed (or rejected).

Considering the two questions posed at the start of this chapter, only one has been answered. A lot of insight has been gained on the evolution of bed morphology for different single-frequency generated wave trains, initial bed heights and water layer depths. The Hele-Shaw setup allowed not only the detailed study of the change in superficial beach shape, but also that of the internal bed structure.

The question of how the sediment is actually transported by the waves is one of a more fundamental nature. While the information during this measurement series was obtained by 10-second interval photography, the interaction between the fluid and the individual particles during the process of bed detachment and re-deposition happens on a much shorter, sub-wavemaker-period timescale. High-speed imaging combined with PIV of the fluid and PTV of the particles might be necessary to investigate this process.

# Chapter 5

## Wave dynamics

One of the complex and interesting questions in the study of beach formation is how breaking waves influence the sediment. Do different types of breaking waves affect the bed differently? How does the bed shape influence the place and type of breaking of the wave? To know if these questions can be investigated using the Hele-Shaw setup, one would first have to know *if* wave breaking occurs at all in this setup, if so what *types* of breaking occur, and finally whether or not the possible breaker types can be related to naturally observed equivalents.

Galvin [14] reported different types of breaking for waves breaking on a normal, three-dimensional shore, namely the spilling, plunging, collapsing and surging breaker. These breaker types and their description as mentioned by Peregrine [21] are listed in table 5.1. While the beach evolution discussed in the previous chapter focusses on a process happening in the order of minutes to hours, wave breaking as was observed in this setup typically happened within a few hundred milliseconds. To record the details of the breaking process, a high-speed Photron SA2 camera with a 50 mm lens was used, which enabled recording speeds up to 1000 fps.

### 5.1 Parameters

An overview of the parameters in this experiment is shown in table 5.2. Many parameters are different from the ones used in the beach evolution experiment (table 4.1). For one, the wavemaker was placed more to the right. Also, the setup was shortened for some experiments and different particles were used (non-porous glass). The water-air surface tension  $\sigma$  was not the same in all measurements, since in some measurements traces of surfactant (Dreft<sup>®</sup>) were present in the water. In those measurements, a known amount of surfactant was added to the water at first, which proved to be too much, and the setup was flushed several times with clean MilliQ<sup>®</sup> water before the spilling breaker measurements were done. At this point, some traces of surfactant were still present, but how much exactly was impossible to determine. Also, the variable  $B_0$  is no longer listed, since the beach is no longer flat at any point of the experiment. The values of  $H_0$  and

Breaker type	Description
Spilling	White water appears at the wave crest and spills down the front face, sometimes preceded by the projection of a small jet.
Plunging	Most of the wave's front face overturns and a prominent jet falls near the base of the wave, causing a large splash.
Collapsing	The lower portion of the front face overturns and behaves like a truncated plunging breaker.
Surging	No significant disturbance of the smooth wave profile occurs except near the moving shoreline.

Table 5.1: Wave types and their description as cited from Peregrine [21].

Varied parameters		Fixed parameters	
Parameter	Values	Parameter	Value
$H_0$	see table 5.3	$L$	$857 \pm 2$ mm
$f_{\text{wm}}$	see table 5.3	$d$	$2.0 \pm 0.05$ mm
$\sigma$	see text and table 5.3	$x_w$	$372 \pm 1$ mm
		$l_w$	$212 \pm 0.1$ mm (app. B)
		$h_w$	$5 \pm 0.1$ mm (app. B)
		$t_w$	$20 \pm 0.1$ mm (app. B)
		$x_{\text{wm}}$	$305 \pm 2$ mm
		$\Delta_{\text{wm}}$	$15 \pm 0.5$ mm
		$h_{\text{wm}}$	$337 \pm 1$ mm
		$l_{\text{wm}}$	$327 \pm 1$ mm
		$\theta_{\text{wm}}$	$21^\circ$ (sec.A.4)
		$T$	20-25 °C
		$f_\rho$	$\rho_{\text{water}}$
		$f_\mu$	$\mu_{\text{water}}$
		$\rho_b$	$2.515 \pm 0.03$ kg dm <sup>-3</sup> (sec. A.3.2)
		$\Phi_b$	0
		$D_b$	$1.8 \pm 0.1$ mm (sec. A.3.1)

Table 5.2: Wave dynamics experiment parameters.

$f_{\text{wm}}$  differ between measurements but were recorded at each measurement. Lastly, small amounts ( $< 0.4\%$ ) of red dye are present in the water, which enables the detection of the free surface. This proved to be of no effect to the surface tension (see appendix A.2), and is assumed to be of no influence to the viscosity either.

## 5.2 Measurements

At the start of a measurement series the setup was flushed with clean MilliQ<sup>®</sup> water a number of times. Before each measurement, water was drained from or added to the Hele-Shaw cell until the desired water level was reached. In some cases, surfactant was added to the MilliQ<sup>®</sup> water before it was added; as described in the previous section, this was followed by a repeated drainage and re-filling of the Hele-Shaw cell with clean MilliQ<sup>®</sup> water, until only small traces of surfactant were left in the cell.

After that, the beach was manually shaped into the desired shape. Different shapes were tried, since the breaker type seemed to depend heavily on the bed shape. Subsequently, the plug was applied to the water input, and the water level  $H_0$  was remeasured. Then, the wavemaker was switched on, accelerating to a constant frequency within approximately 2 seconds. After the wavemaker reached this frequency, the high-speed camera was switched on and then recorded the wave motion for several seconds. When the recording finished, the wavemaker motion was ended and the recording was downloaded to a computer. This process was repeated several times with different bed shapes, water levels, wavemaker frequencies and recording speeds.

An example of a measurement is shown in figure 5.1, which shows snapshots from a 1000 fps recording of a plunging breaker. Eight measurements in particular turned out to give interesting results; their parameters are listed in table 5.3.

## 5.3 Analysis

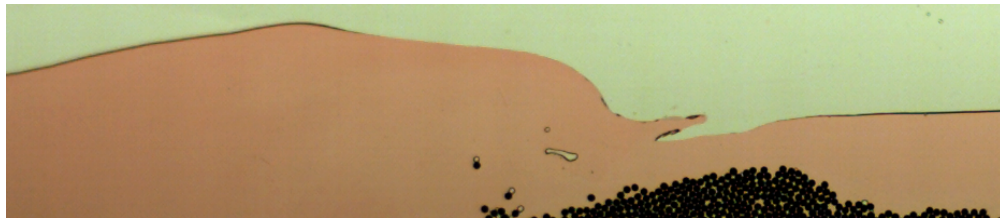
The analysis of the high-speed videos was done in MATLAB. The details of this analysis can be found in appendix F. A program was written to extract the free-surface location from the high-speed video frames, which makes use of the red colour of the water. This data was then plotted in 3D versus time, effectively giving ‘wave evolution’ plots.



(a) 0 ms



(b) 100 ms



(c) 150 ms



(d) 200 ms



(e) 250 ms



(f) 350 ms

Figure 5.1: Snapshots of a breaking wave, which is of the plunging type (see section 5.4).

No.	$H_0$ (mm)	$f_{wm}$ (Hz)	Surfactant added	Breaker type
1	$92 \pm 1$	1.0	yes	Spilling
2	$92 \pm 1$	0.95	yes	Spilling
3	$98 \pm 1$	1.2	yes	Plunging
4	$98 \pm 1$	1.1	yes	Plunging
5	$98 \pm 1$	1.0	yes	Collapsing
6	$95 \pm 1$	0.90	no	Collapsing
7	$102 \pm 1$	0.95	no	Surging
8	$95 \pm 1$	0.90	no	Surging

Table 5.3: Parameter values of eight wave evolution measurements of interest and their observed breaker types.

## 5.4 Results

Four different types of breaking waves have been observed. Two of these match the descriptions of the plunging and surging breakers given by Peregrine [21]. The two others are reminiscent of the spilling and collapsing breakers described by Peregrine [21], however they do not match perfectly. The wave evolution of all measurements mentioned in table 5.3 are shown in figures 5.8 to 5.11. These illustrate the wave evolution of all four breaker types observed. Each of the observed wave types and their differences compared to naturally observed equivalents are treated in the following.

### 5.4.1 Spilling breaker

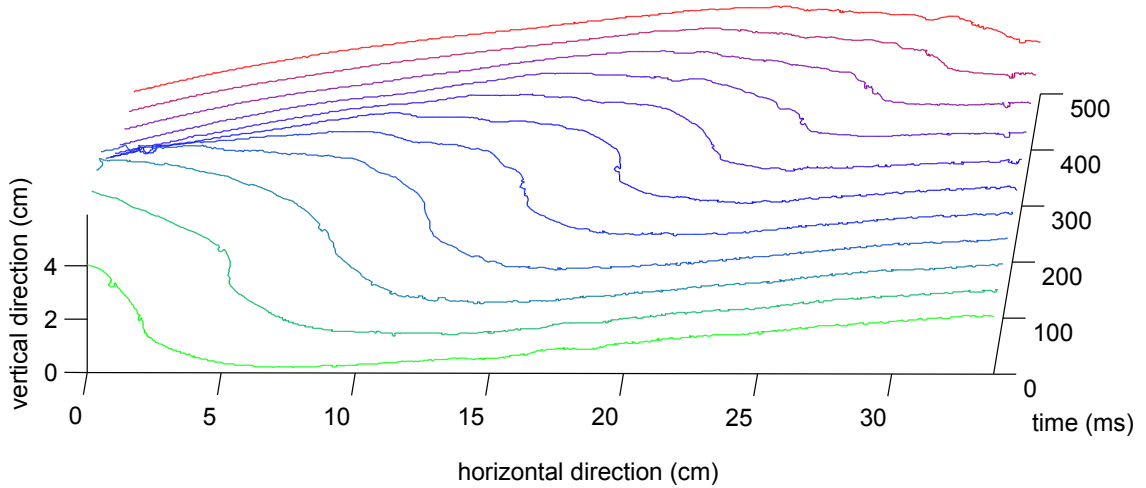


Figure 5.2: Free surface profiles of a spilling breaker; lines are 50 ms apart.

Figure 5.2 shows water surface profiles versus time of measurement 1 in table 5.3, which shows a spilling breaker. This breaker is characterised by bubbles accumulating on the waves' crest (see figure 5.3). At times, the front face of the wave almost becomes vertical (at 200 ms in figure 5.2), but the wave does not break.

Figure 5.8 shows the 3D time evolution of two spilling breakers. Although from the surface profile plot the origin of the bubbles may remain unclear, the 3D representation of the wave evolution sheds some light on this. The visible grooves in the plots are bubbles on the surface, whose lower concave shape can easily be detected, but whose upper meniscus is too thin to detect. Figure 5.8a shows the bubbles travelling along at

the front of the wave. Between 10 and 15 cm in the horizontal direction, it can be seen that two bubbles are picked up by the passing wave.

Note also that the wave does not overturn, even though the front face becomes vertical at a certain moment. The evolution of the spilling breaker in figure 5.8b also clearly shows the pick-up and carrying of bubbles on the free surface of the passing wave.

Compared to a spilling breaker as occurring in nature (*‘White water appears at the wave crest and spills down the front face, sometimes preceded by the projection of a small jet’*; table 5.1), the observed spilling breakers do *gather* the equivalent of ‘white water’, *i.e.* bubbles, at their crest. However, the bubbles are not *formed* there, as is the case in natural spilling breakers. The bubbles were already present on the free surface, and picked up by the passing breaker. Also, no small jets have been observed.

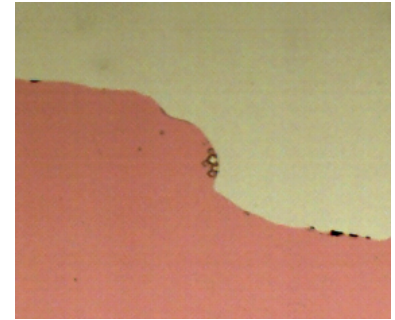


Figure 5.3: Snapshot of a spilling breaker.

### 5.4.2 Plunging breaker

The time evolution of a plunging breaker is shown in the snapshots in figure 5.1. The wave front becomes vertical (0-100 ms), overturns (100 ms) and may entrain water in this process; a secondary jet (150 ms) caused by the ‘splash-up’ plunges again, in this instance with more significant water entrainment (200 ms), after which the entrained bubbles move back up to the free surface (350 ms) due to buoyancy effects. The 3D time evolution of two plunging breakers is shown in figure 5.9. Figure 5.9a shows the evolution of the plunging breaker depicted in figure 5.1. Notice the large groove appearing at around 350 to 400 ms in the figure, which signifies the surfacing of the bubble entrained by the secondary jet. The plunging breaker in fig. 5.9b also shows a clear overturning of the wave and the accompanying air entrainment. The following splash-up however was not strong enough to create a new overturning jet.

The description of a plunging breaker as occurring in nature, stated that *‘most of the wave’s front face overturns and a prominent jet falls near the base of the wave, causing a large splash’* (see table 5.1). This agrees very well with the plunging breakers observed, in which the front face also overturns to cause a splash.

### 5.4.3 Collapsing breaker

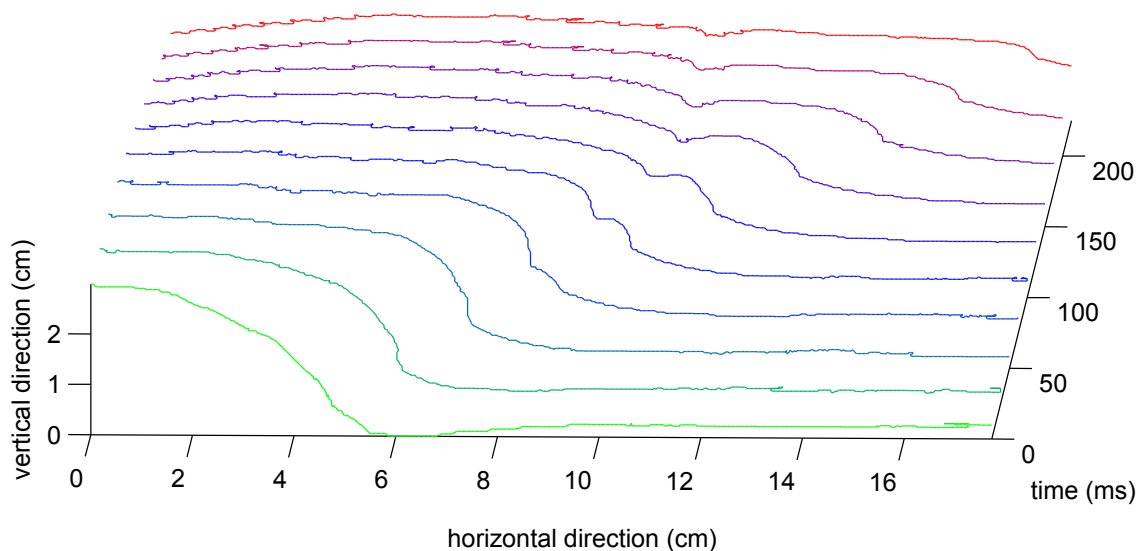


Figure 5.4: Free surface profiles of a collapsing breaker; lines are 25 ms apart.

Figure 5.4 shows water surface profiles versus time of measurement 6 in table 5.3, which shows a collaps-

ing breaker. This breaker is characterised by the splitting of the wave face into a halting upper part and protruding lower part, which is shown here to happen in the time interval 75-125 ms. Notice how the wave front is almost vertical just before the collapse, at 50 ms.

Figure 5.10 shows the 3D time evolution of two collapsing breakers. In figure 5.10b the 3D evolution of the breaker in figure 5.4 is shown. It is interesting to observe how the upper part moves forward, up to a certain point, after which its horizontal position seems to remain perfectly constant for at least the remaining  $\sim 100$  ms in the figure. Perhaps this is due to pinning of the free surface at the glass walls. Figure 5.10a shows a second collapsing breaker evolution. Notice the bubble moving on the waves' crest, which does not seem to be halted by the collapse of the breaker itself.

A collapsing breaker as occurring in nature, was described as a wave where *'the lower portion of the front face overturns and behaves like a truncated plunging breaker'* (see table 5.1). Although the collapsing breaker does show truncation of the practically vertical front face, the lower portion has not been observed plunging, in contrast to natural collapsing breakers.



Figure 5.5: Snapshot of a collapsing breaker.

#### 5.4.4 Surging breaker

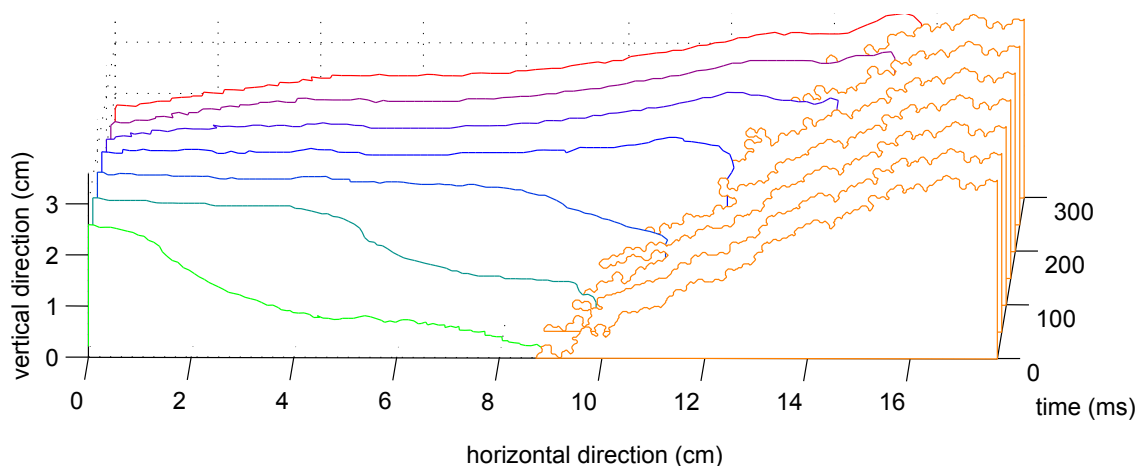


Figure 5.6: Free surface profiles of a surging breaker; lines are 50 ms apart.

Figure 5.6 shows water and bed surface profiles versus time of measurement 8 in table 5.3, which shows a surging breaker. Typically for a surging breaker, hardly anything happens to the wave until it reaches the shore (100-150 ms). There, it suddenly overturns (150 ms) and rolls up the shore (100-300 ms), reaches its highest point and recedes again seawards (not shown).

The 3D time evolution of two surging breakers is depicted in figure 5.11. Figure 5.11b shows the evolution of the surging breaker already depicted in fig. 5.6. Notice the approximately constant velocity of the incoming wave (*i.e.*, the straightness of the wave profile) and the sudden overturn around 150 ms. Figure 5.11a, shows an additional interesting feature. While the beach profile in measurement 8 was (superficially) constant over the 300 ms time interval, here the beach is actually observed changing; the incoming surging wave is seen to 'push up' part of the beach in the process of breaking.



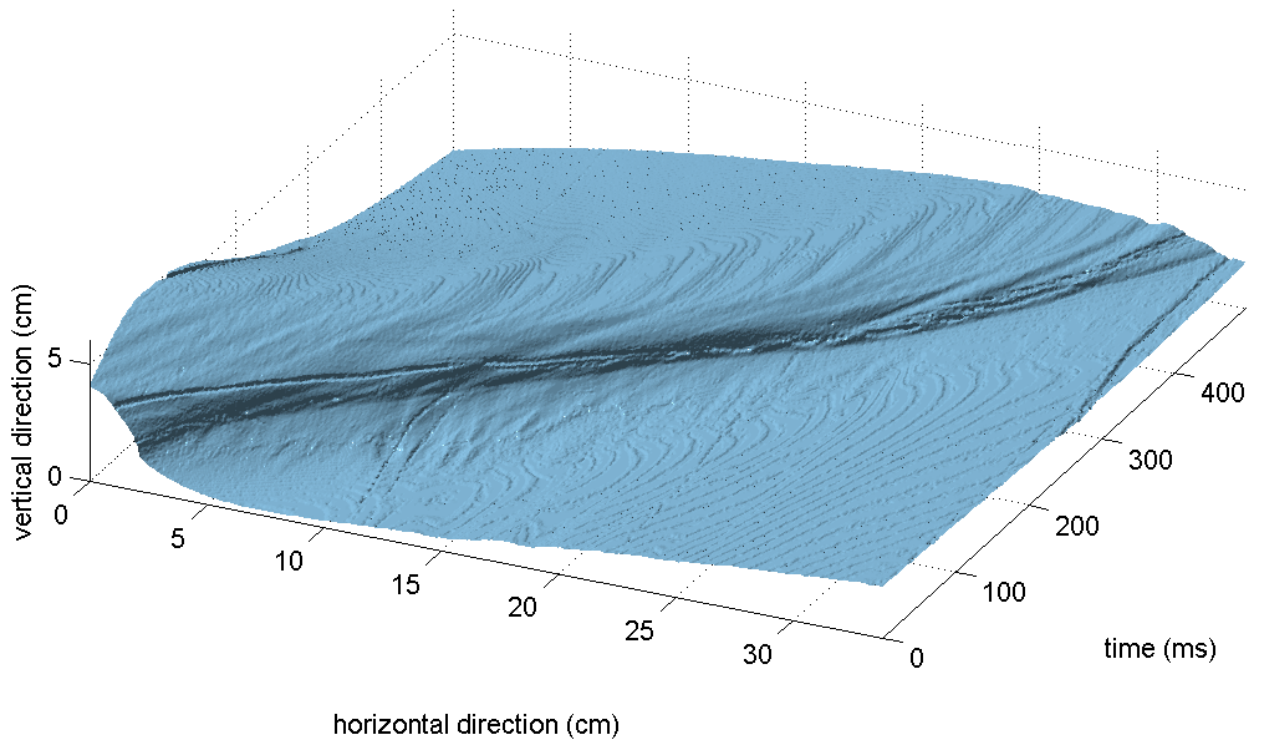
Figure 5.7: Snapshot of a surging breaker.

The description of a surging breaker as occurring in nature stated that ‘*no significant disturbance of the smooth wave profile occurs except near the moving shoreline*’ (see table 5.1). This agrees very well with the observed surging breakers, where little happens to the surface profile until the wave reaches the shore, where it breaks.

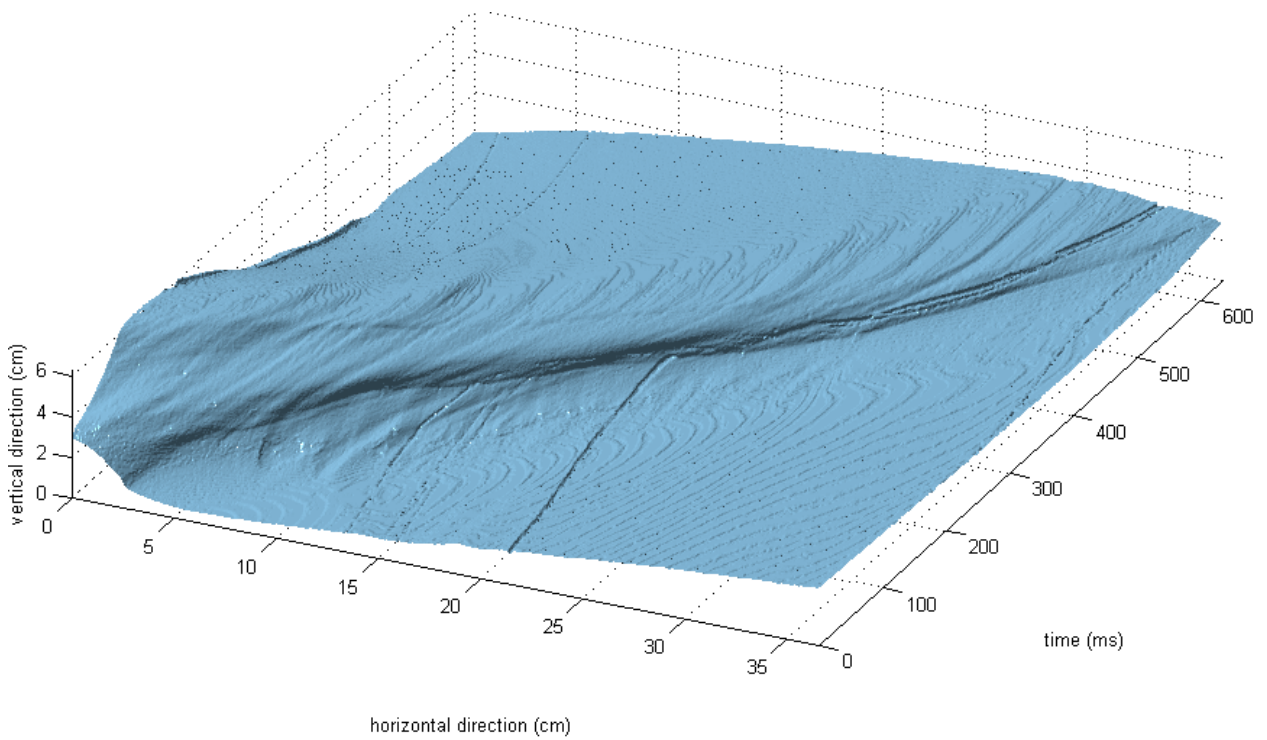
## 5.5 Conclusions and discussion

In answer to the questions posed at the beginning of this chapter, a number of things can be concluded. Firstly, wave breaking *does* occur in the Hele-Shaw cell setup. Secondly, four different types of breaking waves are observed: one in which tiny bubbles appear on the crest (spilling), one with a violent, air-entraining overturn of the wave front (plunging), one in which the front splits vertically in a halting upper and protruding lower part (collapsing) and one that only breaks upon reaching the shore (surging). Lastly, all breaker types show similarities to equivalent types of breaking waves occurring in nature. Two of the four types also show clear differences to their natural counterparts. In spilling breakers, bubbles were not formed by the breaking of the wave; existing bubbles were merely accumulated on the wave’s crest. In collapsing breakers, the lower portion of the wave front protrudes, but no plunging was observed afterwards.

The origin of these differences may perhaps be surface tension. While waves observed in nature are typically much larger, in the centimetre-scale waves observed in these experiments surface tension effects may become more dominant. This is suggested by the necessity of surfactant traces in the water in order to generate plunging breakers. Since the lower part of a collapsing breaker would act like a mini-plunger, the surface tension effects preventing the breaking are even more pronounced. In a natural spilling breaker, the bubble generation is caused by the tip of the wave overturning and rolling down the wave front itself, entraining air in the process. In the setup, surface tension would prevent the tip from breaking, thus preventing the wave from generating air bubbles.

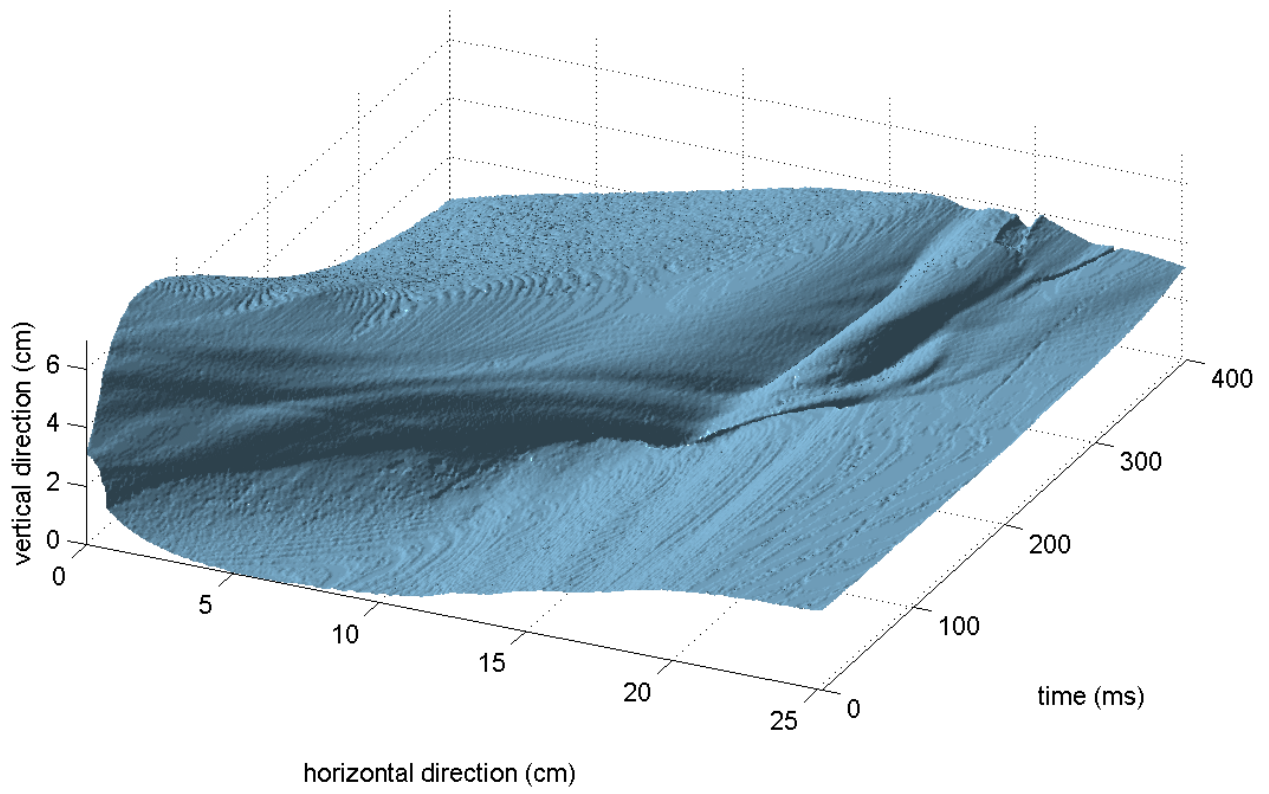


(a) measurement 1

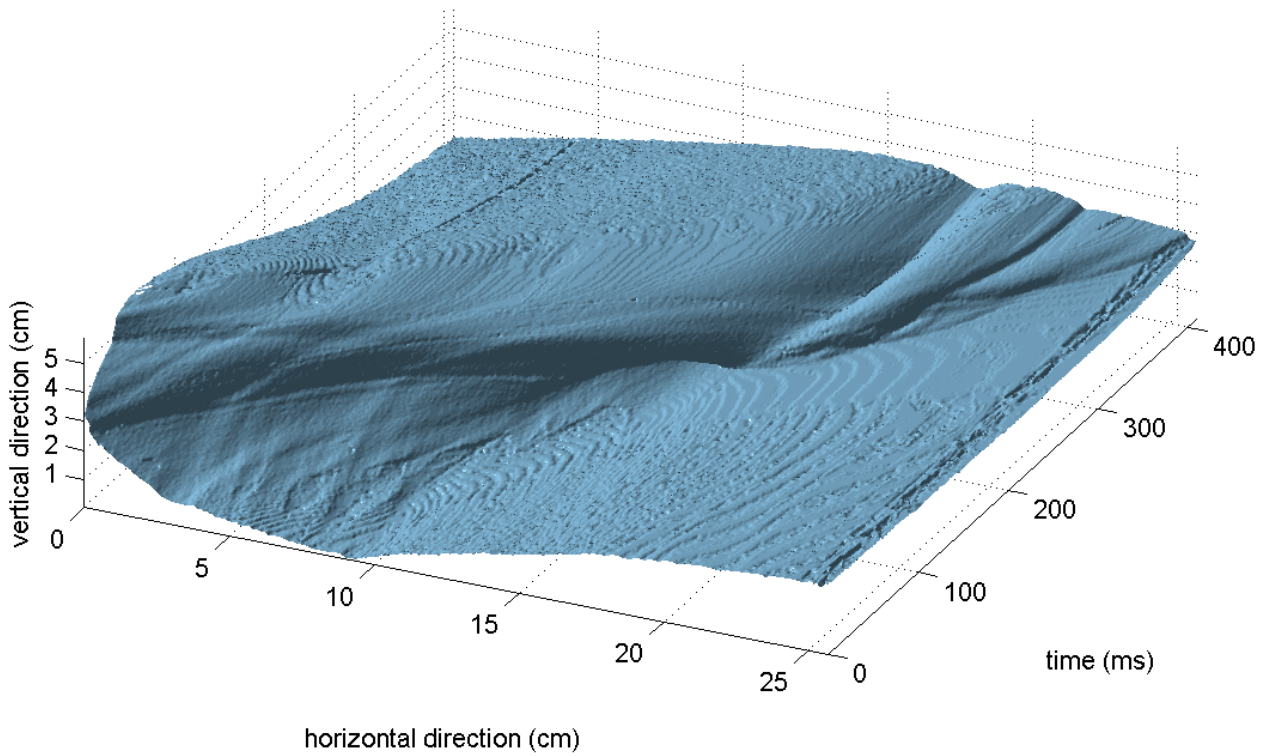


(b) measurement 2

Figure 5.8: Wave evolution plots of two spilling breakers. The thin ‘troughs’ indicate bubbles, which travel along on the waves’ crests.



(a) measurement 3



(b) measurement 4

Figure 5.9: Wave evolution plots of two plunging breakers. Note the clearly visible overturning and plunging of the waves.

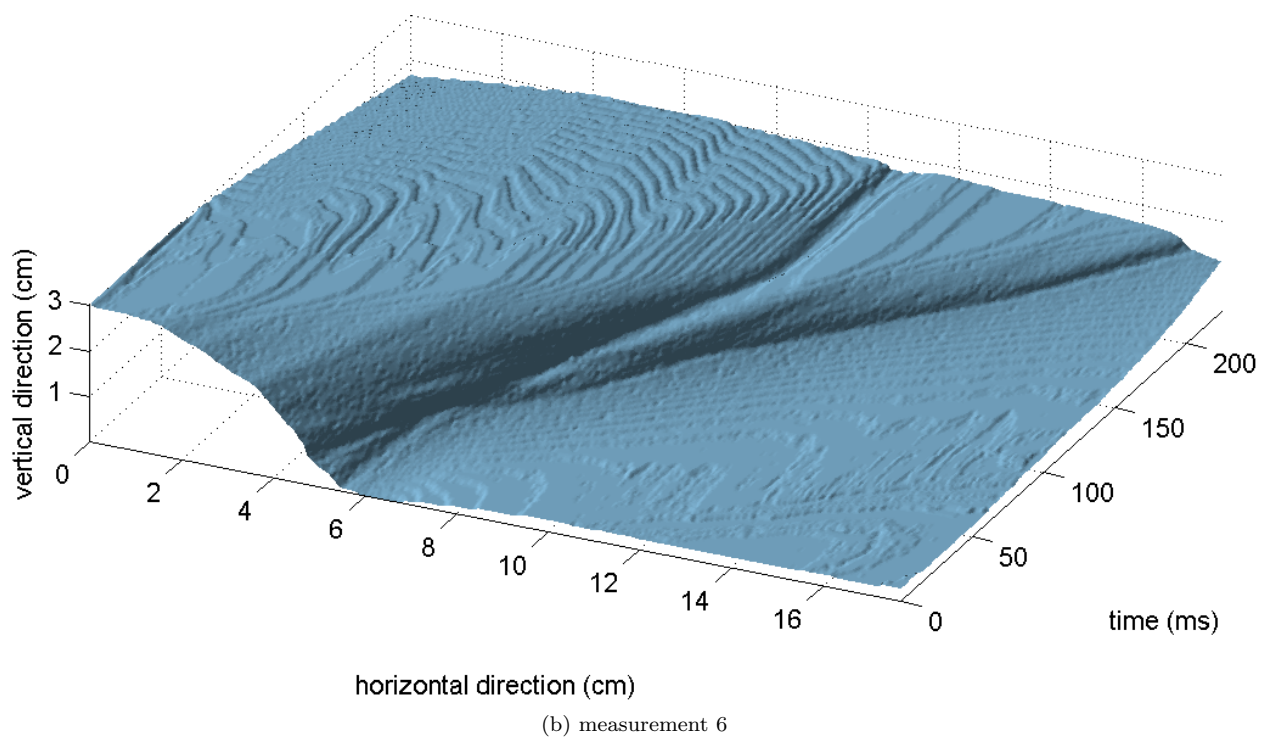
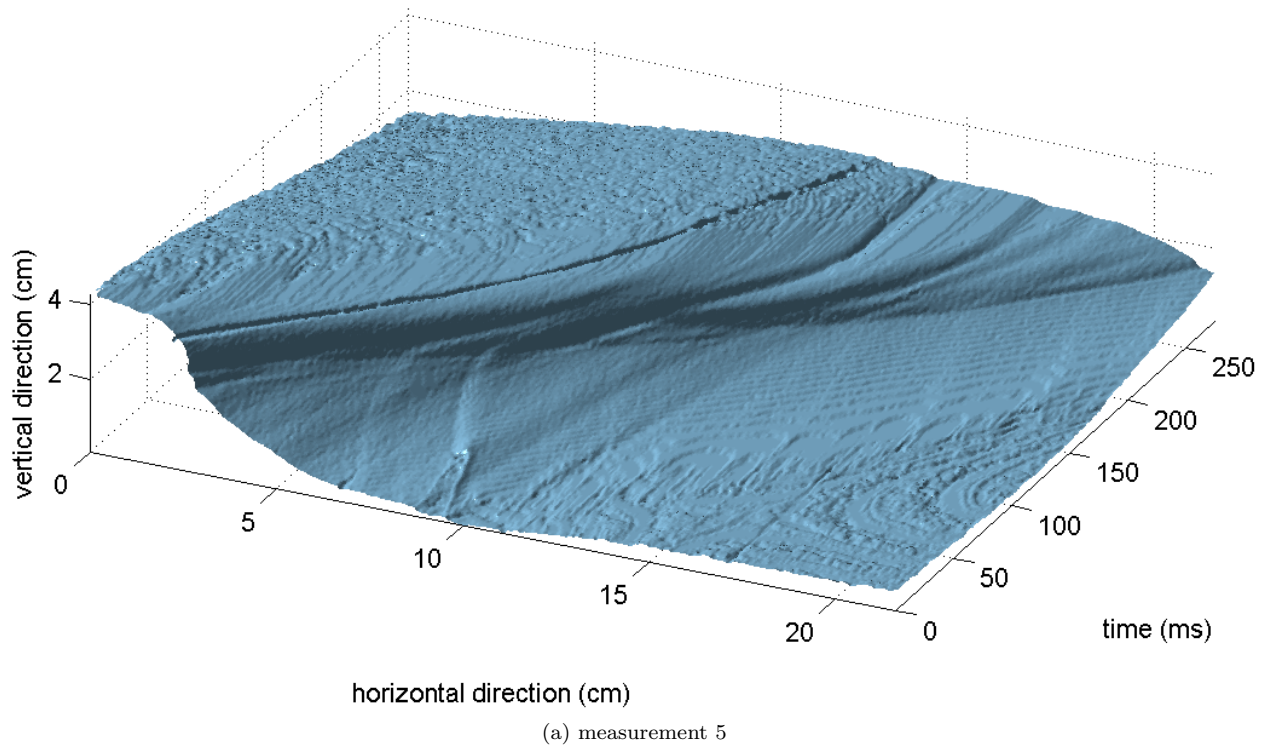


Figure 5.10: Wave evolution plots of two collapsing breakers, which are characterised by the collapse of the wave's front in a halting upper part and a protruding lower part.

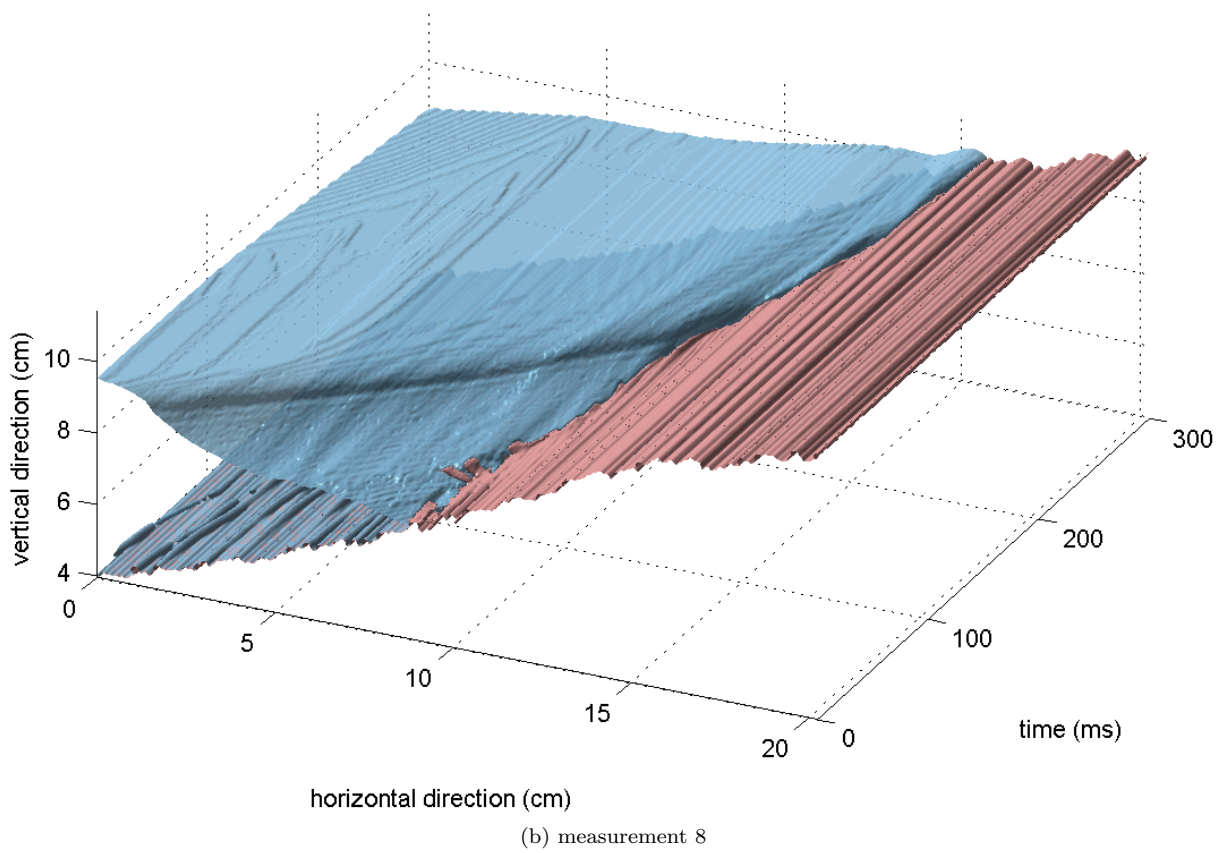
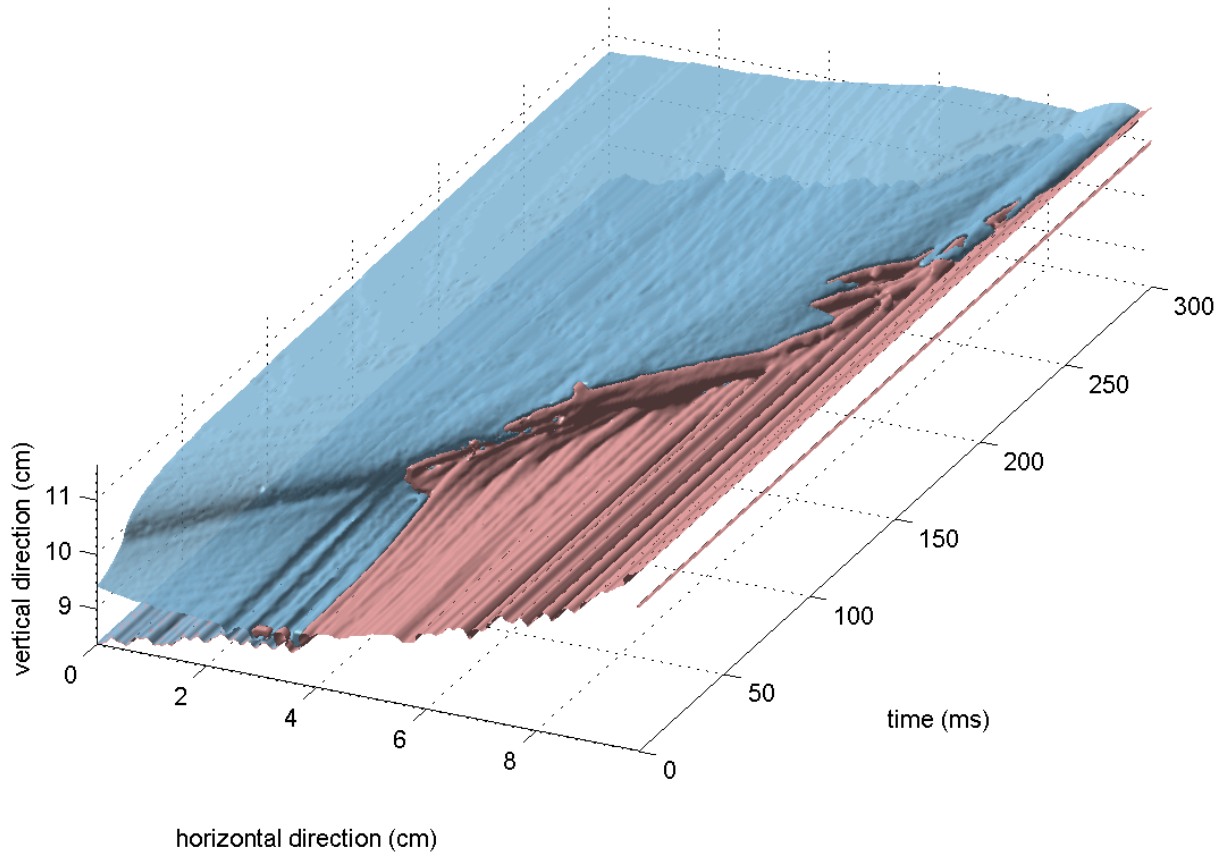


Figure 5.11: Wave evolution plots of two surging breakers<sup>47</sup>. The water is depicted in blue, the beach in red. Note, that no breaking occurs until the waves reach the beach.



# Chapter 6

## Model valorisation

One of the goals of the experiments described in this report was the valorisation of (future) results obtained from 2D numerical simulations. As was described in section 3.2, Gagarina et al. [13] made a numerical model of the flow in the Hele-Shaw geometry using a 2D potential flow approximation. Certain effects which occur in real world flow, however, were not incorporated. Possible sources of difference between experiments and this were expected to be energy loss (damping) due to the moving contact line, and surface tension effects. To find out whether or not these differences change the flow significantly, some experiments were conducted to compare the model with. Since there was no possibility to measure the exact flow profile in the setup, a comparison in terms of system energies was considered. However, to get the kinetic energy of the system one would need to know the flow profile too. It was chosen therefore to do experiments and simulations and extract from both only the (easily measurable) potential energy, which were then compared. An experiment which is easy to simulate was thought of for a first comparison between numerics and experiments. In this experiment, no particles or fixed wedge is present in the Hele-Shaw cell, only a fixed amount of water. Figure 6.1a shows the initial condition for the simulation. The water surface is tilted under an initial angle  $\alpha$ , after which it is released at  $t = 0$ . Experimentally, a fixed tilted water surface is impossible to achieve. An experimental approximation to the numerical initial condition is shown in figure 6.1b; in the experiments, the whole setup was tilted under an angle  $\alpha$ , and at the start of the measurement the setup is turned back horizontally within a time  $\Delta t$ . From the moment of ‘touchdown’, the potential energy in the system is measured using an approximation of equation 3.50, *i.e.*

$$E_p = \frac{1}{2} \rho_0 g \sum_{q=0}^{L/\Delta x} \eta(q)^2 \Delta x, \quad (6.1)$$

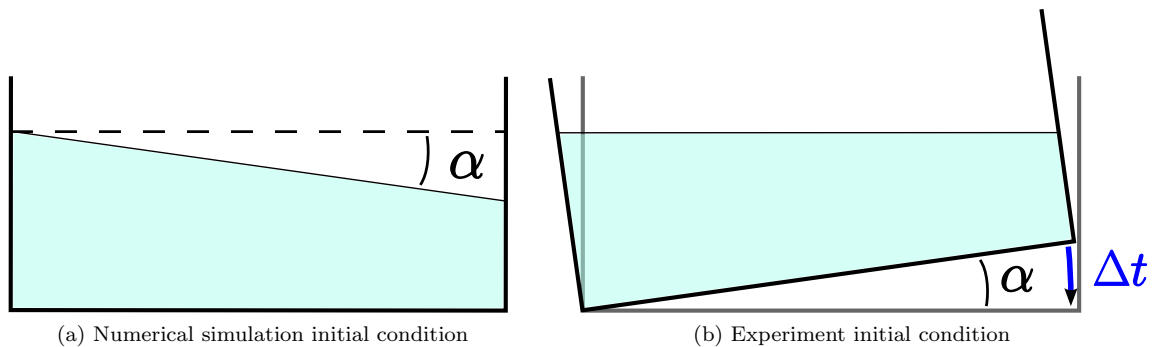


Figure 6.1: Schematic representation of the initial conditions of the numerical simulation and the valorisation experiments. The simulation starts with a water level under a tilted angle  $\alpha$ ; the experiments start with the setup tilted under an angle  $\alpha$ , after which it is turned horizontally within a time  $\Delta t$ .

Meas./Sim.	$L$ (cm)	$h_0$ (cm)	$\alpha$ ( $^\circ$ )	$\Delta t$ (ms)	$T$ ( $^\circ\text{C}$ )
05/17 m1	$95.6 \pm 0.1$	$9.9 \pm 0.1$	$6.53 \pm 0.1$	$429 \pm 10$	$24.0 \pm 0.3$
05/17 m2	$95.6 \pm 0.1$	$9.9 \pm 0.1$	$6.06 \pm 0.1$	$336 \pm 10$	$24.0 \pm 0.3$
05/21 m1	$95.5 \pm 0.1$	$10.4 \pm 0.1$	$4.61 \pm 0.1$	$130 \pm 10$	$25.3 \pm 0.3$
05/21 m2	$95.5 \pm 0.1$	$10.4 \pm 0.1$	$4.17 \pm 0.1$	$136 \pm 10$	$25.3 \pm 0.3$
05/21 m3	$95.5 \pm 0.1$	$10.4 \pm 0.1$	$3.95 \pm 0.1$	$173 \pm 10$	$25.3 \pm 0.3$
05/21 m4	$95.5 \pm 0.1$	$10.4 \pm 0.1$	$5.42 \pm 0.1$	$241 \pm 10$	$25.3 \pm 0.3$
Simulation	100	10	5.1428	–	25
Simulation	100	10	4.610	–	25

Table 6.1: Measurement and simulation parameters as used in the numerical verification experiments. the first column mentions the date and measurement names and ‘Simulation’ for the simulations. Further,  $L$  is the horizontal setup length,  $h_0$  the static water depth,  $\alpha$  the initial tilting angle and  $\Delta t$  the initial turning time (see fig. 6.1), and  $T$  the temperature. Note, that no temperature was implemented directly in the simulations; the temperature mentioned here signifies that the values of the water properties (density, viscosity) used in the model were those at 25  $^\circ\text{C}$  as known from literature.



Figure 6.2: Example of analysis of a frame in a numerics verification experiment. The red line indicates the location of the water surface as found by the analysis program.

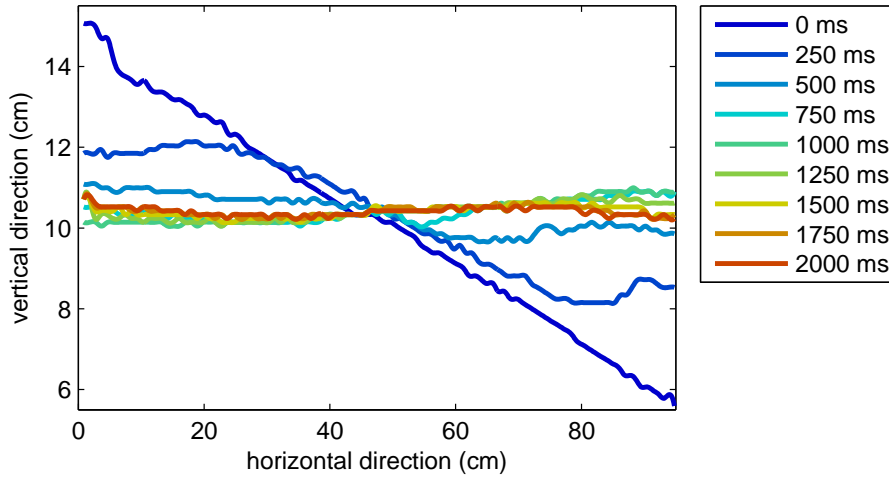
in which  $\rho_0$  is the water density,  $g$  the gravitational acceleration,  $L$  the horizontal setup length,  $\eta$  the free surface profile and  $\Delta x$  the resolution of the camera used, which was approximately 1 mm.

## 6.1 Parameters and measurement setup

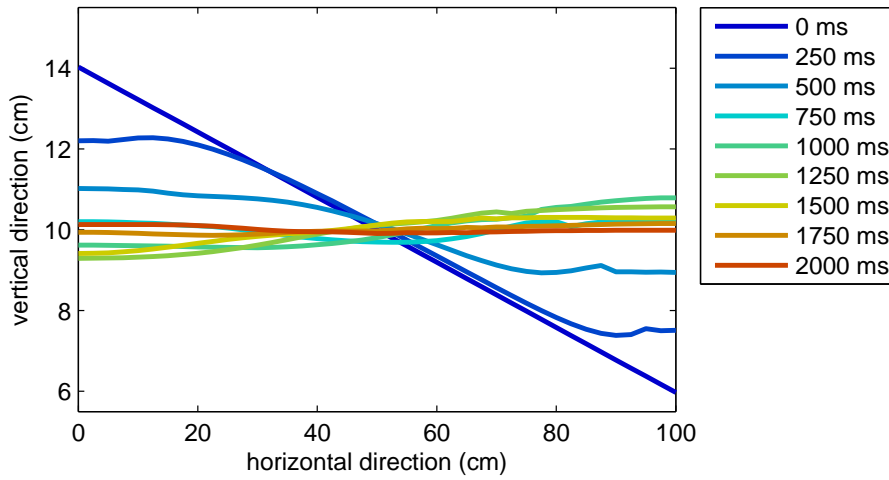
Table 6.1 lists the parameters used in the simulation and experiments. As mentioned earlier, no particles or wedge were present in the setup during the measurements, only water. Further, a Mikrotron Eosens high-speed camera was used in combination with an Avamar 28 mm lens, recording the experiment at 500 fps, with a shutter time of 1.5 ms. The turning of the setup was done manually.

## 6.2 Analysis

An example of an analysed frame is shown in figure 6.2. The red line indicates the location of the water surface as found by the analysis program. In order to be able to extract the water surface from the photographs, 0.2%Vol. red dye was added to the water, just as in the experiments described in chapter 5. The same program was used for the extraction of the water surface; see also appendix F. Due to light distortion (fig. 6.2, left) and intrinsic analysis program properties, small parts of the water surface at the left and right end of the setup were not taken into account. The total horizontal water surface length missing due to this is on the order of 1 cm; with a setup length of  $\sim 96$  cm, this would add  $\sim 1\%$  to the error in the found potential energy.



(a) Experiment; times are indicated relative to the moment of 'touchdown';  $\alpha = 4.61 \pm 0.1^\circ$ .



(b) Simulation;  $\alpha = 4.61^\circ$ .

Figure 6.3: Snapshots of water surface profiles for different times in experiment and simulation.

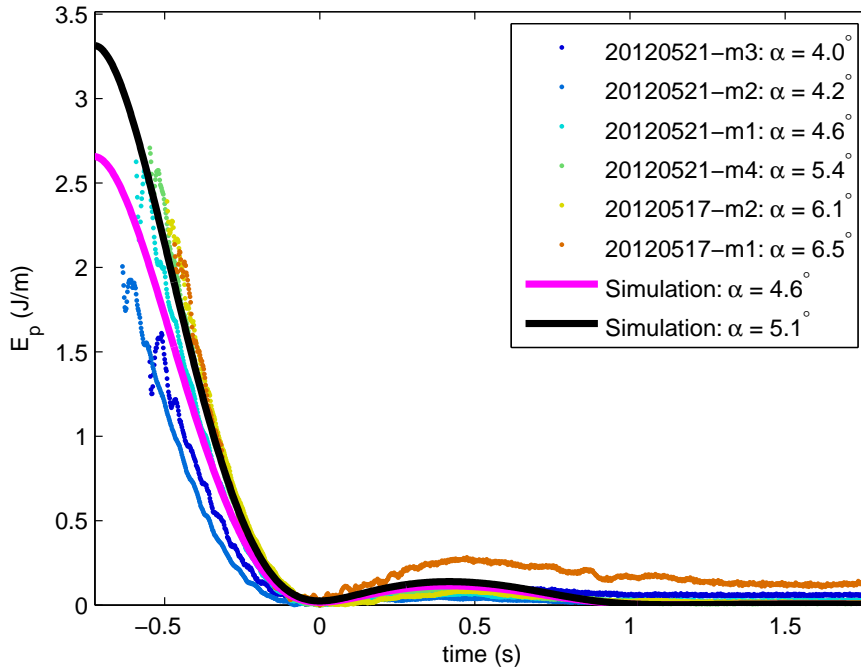
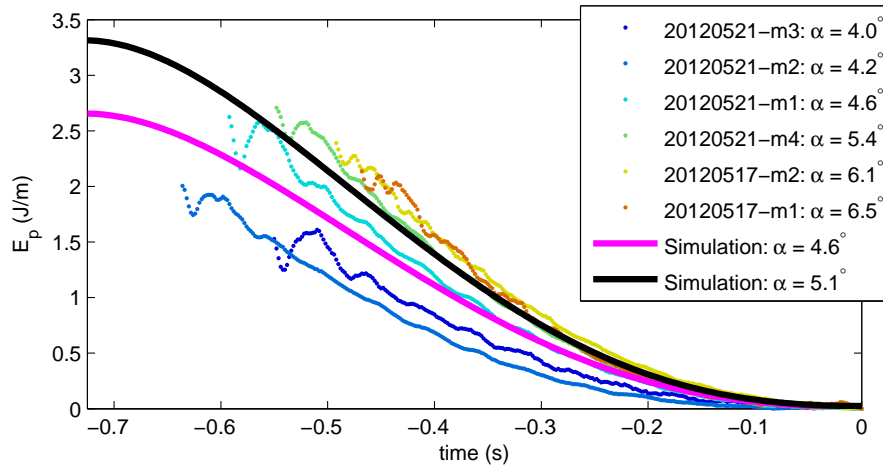


Figure 6.4: Potential energy versus time for all experiments and both simulations.  $t = 0$  is the time at which  $E_p$  of each experiment first reaches its minimum  $E_0$ .

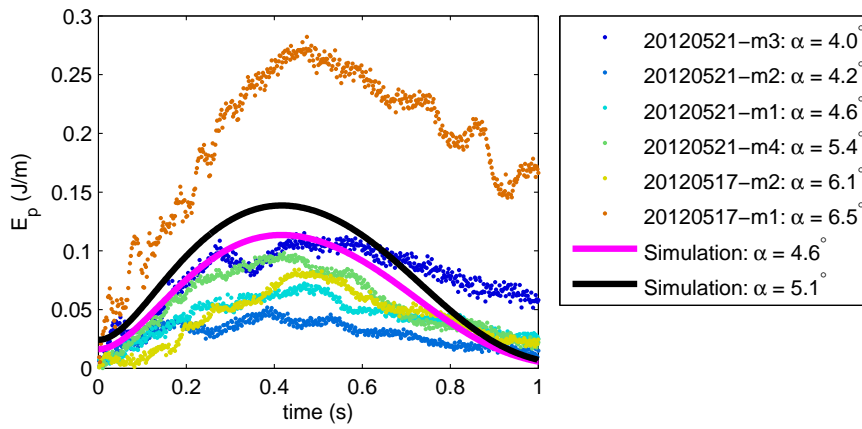
### 6.3 Results

Figure 6.3a shows water surface profiles at different times in a typical valorisation experiment ( $\alpha = 4.6^\circ$ ). Already the time scale in which the energy in the system is dissipated becomes clear; the water surface returns to the static state within approximately 2 seconds. Figure 6.3b shows similar water surface profiles for the simulation ( $\alpha = 4.6^\circ$ ). The agreements between both are striking. Notice also the small shockwave appearing on the right, which is present both in experiment and simulation. Note the small but visible difference in the surface height around  $t = 1000$  ms. This indicates that more of the system energy is dissipated in the first second in the experiment than is in the simulation. In figure 6.4 the measured and simulated potential energies are all plotted. Firstly using the moment of the initiation of the turning of the setup as  $t = 0$ , it was found that large deviations in time existed between the results, which strongly correlated with the rotation angle  $\alpha$  and rotation time  $\Delta t$ . This led to the conclusion that, due to the differences in rotation angle and rotation time, combined with the fact that each rotation was done manually, the initiation of rotation was *not* suitable for defining  $t = 0$ . Therefore, it was chosen to use the time in each measurement at which the potential energy first reached its minimum  $E_0$  as  $t = 0$ .

Figure 6.5 zooms in on different parts of figure 6.4. Interestingly, figure 6.5a shows a correlation between initial angle  $\alpha$  and initial potential energy decay rate. The reason for this might be further investigated. The potential energy in the simulation with  $\alpha = 5.1^\circ$  has a very good agreement with the experiments: its values are between that of  $\alpha = 4.6^\circ$  and  $\alpha = 5.4^\circ$ . The potential energy of the  $\alpha = 4.6^\circ$  simulation is initially a bit lower than that of the  $\alpha = 4.6^\circ$  experiment, but in the last 0.35 seconds before reaching the minimum both completely overlap. Figure 6.5b shows the first second after reaching the minimum. All potential energies show a slight recovery. For the simulations, the amplitude of this recovery seems to correlate with  $\alpha$ . In the experiments, no such correlation was observed. Note, that except for the experiment with  $\alpha = 6.5^\circ$ , maximum re-obtained potential energy in the experiments is less than that in the simulations. Examination of the surface lengths in experiments gives a maximum extension of the surface of a factor 1.07 compared to the static case. This means the added energy stored in the surface due to surface tension (equation 3.51) is only 5 mJ/m maximum. This is negligible compared to the difference in maximally recovered potential



(a) Initial potential energy decay.



(b) Potential energy first recovery.

Figure 6.5: Potential energy versus time for all experiments and both simulations. Zoom-ins of figure 6.4.

energy between simulation and experiments (figure 6.5b), which is in the order of 50 mJ/m. This indicates that the energy dissipation has to be slightly higher in the experiments, as was already suggested by figure 6.3. A possible source for this is dissipation due to the moving contact line, which was not implemented in the model. Note further, that the timing of reaching this maximum agrees very well between experiments and simulations.

## 6.4 Conclusions and discussion

The comparison of potential energy decay between simulations and experiments, figure 6.4, shows very good agreement of theory and experiments. Both the timing and initial decay rates of the potential energy matches the experiments very well. Also the water surface profiles, figure 6.3, are very similar. The major difference between experiment and model is the amount of potential energy regained after the first minimum. This cannot be caused by possible storage of energy in the surface, which is at least an order of magnitude smaller. Therefore, energy is probably slightly more dissipated in the experiments as compared to the simulations, which might be caused by damping due to the moving contact line. This should be further investigated.

The results give some confidence that the not-incorporated effects on the flow of surface tension and dissipation due to the moving contact line are small. A few things, however, should be kept in mind; Firstly, note that the type of experiment done to check the numerical model was not the same as any of the other experiments described in this work. The wave generated here was not at all a travelling one like those induced by the wavemaker, but rather a standing wave (of mode 2), which was not generated by a wavemaker but purely gravity driven. Also, no wave breaking took place in the valorisation experiment, which would have been impossible for the model to capture. Secondly, no particles, wedge or wavemaker were present in the setup, although objects within the bulk of the fluid may have relatively little effect on the effects caused by the movement of the fluid surface. Thirdly, the turning of the setup was done manually in these experiments. A more automatically controlled turning, perhaps by use of a (linear) motor, will likely give more reliable and better reproducible experimental results. Lastly, only the potential energy was measured and compared. Measurements of the entire flow profile (using, *e.g.*, PIV) would allow for a more thorough comparison of model and experiments.

## Chapter 7

# Conclusions and discussion

In this thesis, an attempt has been made to answer the following three questions: (1) How does the bed of mono-disperse particles evolve under influence of single-frequency generated wave trains? (2) Does wave breaking occur in the Hele-Shaw geometry, and if so, is it comparable to the breaking of waves observed in nature? (3) How well do initial models simulate the flow in this setup? Considering these research questions, which were posed at the beginning of this thesis, all three have been (partially) answered.

Firstly, some interesting results have been obtained concerning the evolution of the bed. One of the main results of this work is the phase diagram figure 4.13b. The water layer depth proves to be the most dominant parameter to determine the steady bed morphology type; dunes were observed at small water layer depths beaches at larger depths ( $\gtrsim 5$  cm), and a hybrid-like dune-beach at an intermediate water layer depth (3 cm). The general activity of the bed seems to be determined by  $f_{wm}$  and  $B_0$ . The amount of sediment transport observed increases with increasing initial bed height  $B_0$ , and the phase diagram suggests a slight optimum in terms of transport at an  $f_{wm}$  of approximately 0.9 Hz.

Furthermore, the internal structure of the bed was studied. The packing fraction of the bed as a whole increases continuously during the experiments. Not only are transported particles redeposited in a more compact configuration, but also the packing fraction of the part of the bed which is not redeposited increases. The increase of packing fraction was expected to correlate with the wavemaker frequency, but significant deviations from this were found, which makes further investigation necessary. The dual time regime behaviour of the change in packing fraction over time agrees with simulations done by Barker and Mehta [5], who explained this to be caused by the quick rearrangement of individual particles, and the slower rearrangement of particle clusters.

Secondly, wave breaking has been observed in the Hele-Shaw geometry. Four different types of breaking waves have been observed (spilling, plunging, surging, collapsing) which show quite some similarities to breaking wave types observed in nature. The origin of the differences between the waves in this geometry and in nature may be the difference in scale, which causes surface tension effects to be more dominant in the setup.

Lastly, experiments were conducted to compare a numerical model by Gagarina et al. [13] based on 2D potential flow with. The results are encouraging; the potential energy curves agree very well, just as the water surface profiles. The major difference between experiment and model is the amount of potential energy regained after the first minimum; the model shows less dissipation of energy than the experiment. This might be caused by damping due to the moving contact line, and should be further investigated. Some important aspects should be noted; The experiments done to compare the model with are quite different from the other ones described in this work. Also, no wave breaking took place, which would have been impossible for the model to simulate. Lastly, only the potential energies have been compared quantitatively, while knowledge of the entire flow profile would allow for more thorough comparison.

Summarising, the Hele-Shaw cell geometry is a suitable means to study shape evolution and compactifi-

cation of a bed of mono-disperse, spherical particles. The observation of breaking wave types equivalent to those observed in nature, gives confidence to the comparability of phenomena observed in this geometry and those present in nature. An initial comparison between a model based on potential flow and dedicated valorisation experiments shows significant agreement. Further investigation should be undertaken to build a model comparable to bed evolution experiments.

# Chapter 8

## Recommendations

The research described in this thesis and the conclusions drawn based on that may be an inspiration for future work. Recommendations for possible work to be done will be presented in this chapter in two different sections: experiments and research the author would have liked to conduct if not for a lack of time, and aspects that should be taken into consideration if a new setup would be constructed.

### 8.1 Possible future research

During the experiments and their analysis, many aspects proved to deserve a more thorough investigation. Due to time limitations not everything could be looked into as thoroughly as desired. Some experiments and analyses that might deserve a further investigation are listed in the following.

#### Further analysis of current data

The data gathered during the beach evolution experiments allows for a more thorough analysis of the bed structure and evolution than has been presented in this work. Some possibilities for further analysis using the readily available dataset are:

- Possible dependence of the maximum stable eastern (downstream) angle (figure 4.14) on the measurement parameters
- Localised densification of the bed. A possible approach is the comparison of Voronoi cell sizes in every frame to the cell sizes of the nearest cells in the previous frame. This may give some interesting insights in the bed packing.
- Possible dependence of the size of the bed packing fraction change (figure 4.16b) on the measurement parameters
- Possible dependence of the long-term bed rate of change of packing fraction on the measurement parameters

#### Flow field

Although the movement of sediment and the details of the water surface in breaking waves have been studied, little is known about the details of the internal fluid motion. A PIV measurement using tracer particles was not conducted due to fear of permanent contamination of the setup (see next section). Nevertheless, such an experiment is highly recommended; it will give better insight into the details of the internal fluid flow, and if conducted quantitatively may serve as an additional means to validate the numerical simulations.

#### Dependency of wave types on bed morphology

In this study, four different wave types have been found. However, not thoroughly investigated how they depend on the shape of the bed, and more specifically, at what point of the bed the breaking occurs. In the study of natural beaches, the so-called Iribarren number ([7; 18]) is defined as  $a_0\omega^2/g\alpha^2$ , in which  $a_0$  is the ‘offshore’ wave amplitude,  $g$  the gravitational acceleration,  $\omega$  the wave frequency

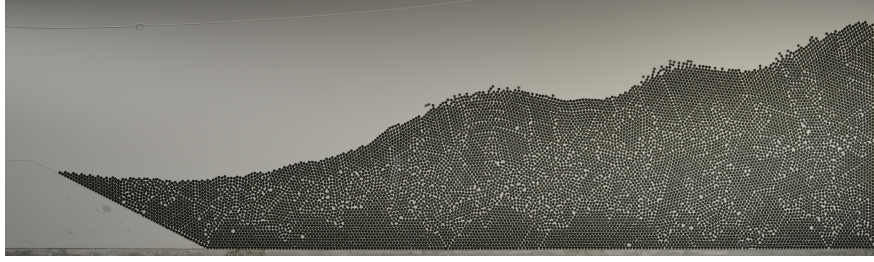


Figure 8.1: Example of observed ‘humps’ (possibly 2D sand ripples) in the beach evolution experiment series.

and  $\alpha$  the local bed slope. It is a ratio of the wave ‘steepness’  $a_0\omega^2/g$  and the square of the bed angle  $\alpha$ .

An examination of the dependence of position of the wave breaking and wave breaker type on Iribarren number using a variety of fixed (*e.g.* plastic) bed shapes may be recommended, followed by a thorough comparison to existing coastal engineering literature.

### Transport dynamics

In the study of sediment transport as described in this report, photographs were made every 10 seconds. This is convenient to investigate the long-term evolution of the bed. However, the more fundamental interaction between the fluid and the individual particles during the process of bed detachment and re-deposition happens on a much shorter, sub-wavemaker-period timescale. High-speed imaging combined with PIV of the fluid and PTV of the particles might be necessary to study this interaction; alternatively, the option of a new experiment dedicated to the study of the interaction between (Hele-Shaw) fluid motion and sedimenting particles should be investigated.

### Spacing

The ratio of Hele-Shaw cell spacing and mean particle diameter  $\Gamma = d/D_b$  has been chosen for rather practical reasons to be  $\Gamma = 1.1$ . Lee, Ramos, and Swinney [20] however show that for this ratio the vortices observed behind sedimenting spheres have a three-dimensional structure, while vortices for  $\Gamma \leq 1.05$  behave quasi-two-dimensional. This suggests that a smaller ratio  $\Gamma$  might give results which are more suitable for comparison with future 2D simulations of sediment transport.

### Two-dimensional sand ripples

In many cases, an unexplained ‘hump’ has been observed on top of both evolving and quasi-steady beds. Figure 8.1 shows a snapshot in which multiple humps can be seen. Only recently the question was raised whether they might be two-dimensional manifestations of the extensively studied 3D sand ripples (*e.g.*, [4; 16; 24]) appearing on natural suspended beds. The rise and decay of these humps have not been studied yet, and further investigation into whether they actually are quasi-2D sand ripples and their dynamics is recommended.

### Hele-Shaw flow assumption

As was shown in section 3.1.4, the assumption of Hele-Shaw flow was dubious. Although the results obtained in comparing simulation and experiments were encouraging, an additional investigation of the validity of the Hele-Shaw flow assumption may be useful.

### Glass particles

The Gamma Alumina particles used in the beach evolution experiments have a few disadvantages. They are highly porous, which is firstly not practical experimentally (the particles have to be put into the setup a day before starting the measurements in order to let the pores be filled with water), but also not ideal for comparison with a model based on non-porous particles. They break down easily, after which it is hard to remove particle fragments.

As described in appendix A, glass particles have been considered. They are non-porous, not breaking down, and not scratching the glass plates as was feared initially. The current problem is their hydrophobicity, which is caused by their black coloring. Removal of this coloring by treatment with

Piranha solution rendered the particles poorly detectable by the current analysis program. Since the non-porous, hard glass particles are highly favourable over the porous Gamma Alumina particles, a continuing of the search for a solution to the hydrophobicity is highly recommended.

### **Different liquids**

Since the main differences between naturally observed and experimental waves is likely to be caused by surface tension, the use of lower surface tension liquids should be looked into. Ethanol, which is already used for cleaning of the experiment, is a possible candidate. Note, that some parts of the setup (*e.g.*, the spacers) are not completely ethanol resistant. The long-term application of ethanol may severely affect these parts.

### **Different waves**

In the experiments described in this work, only waves generated by a sinusoidal, single-frequency motion of the linear actuator have been considered. It may be interesting to study the behaviour of waves generated in numerous different ways, for example by (timed) switching of frequency, by a superposition of frequencies, or by non-sinusoidal motion of the wavemaker. The capabilities of linear actuator and/or amplifier to perform such motions should also be examined.

## **8.2 Possible setup improvements**

At the start of the measurements described in this work, the experimental setup described in chapter 2 had already been constructed. Given it was a second generation design, it had undoubtedly been a major improvement on its predecessor. After numerous hours of experiments however, some possibilities for further improvement were encountered. They are as follows:

### **Spacing**

In the current setup, the spacing between the glass plates is fixed; the bottom and sides have been glued to the frame in order to prevent the Hele-Shaw cell from leaking. An adjustable spacing would off course be favourable for scientific reasons. Besides that, the fixed spacing renders a proper cleaning of the setup hard to achieve. The development of an alternative sealing mechanism, possibly using tailor-made rubber sealing, is recommended.

### **Spacers**

For the current experiments, plastic spacers designed for building model trains were used as spacers between the two glass plates. Although they may have the right precision, they are not ideal for two reasons. First of all, since they are made of plastic, they were feared to be deformable, albeit perhaps only under high pressure. The establishing of the spacing between the two glass plates was done by screwing, and no hard boundary was met when screwing the plates towards each other, as would be expected from indeformable spacers. Secondly, the spacer material, polyethylene, is not completely ethanol resistant, although no visible deterioration of the spacers due to ethanol cleaning of the setup has been observed. Literature (*e.g.* Lee et al. [20]) suggests the use of stainless steel spacers. Not only would they provide a better accuracy to the spacing between the glass plates, they also are less susceptible to deterioration.

### **Wavemaker**

The current pendulum-like wavemaker functions well but has a few disadvantages. Firstly, the wavemaker is hard to model numerically. Secondly, it is hard to align. Combined with the small amount of flexibility present in the material, this causes the position of the wavemaker perpendicular to the two glass plates (*i.e.*, the exact part of the spacing the wavemaker occupies) to be variable. This introduces an undesired uncertainty into the system. A vertical wavemaker with only horizontal movement may be easier to model; the alignment problem would however remain. A hydraulically or pressure driven wavemaker would perhaps be even more easily modelled and would not suffer from the alignment problem.

### **Minimal frame**

The currently present wooden frame is very useful for supporting the vertically positioned Hele-Shaw

cell. However, it renders the edges of the cell invisible. Additional plastic strips on the sides and bottom had to be introduced in order to make the entire experimental system visible. Especially in a fixed-spacing Hele-Shaw cell, additional fixed parts in the cell may add to an increased accumulation of dirt. Therefore, a minimally visible frame, serving purely to support the vertical position of the Hele-Shaw cell and to establish its spacing, is recommended.

# Acknowledgements

During the time I worked on this project, I received support from many people who helped me by having useful discussions, by generating ideas for improvements of analysis or experiments, or by having relaxing talks at the coffee machine or lunch table.

First of all I would like to express my gratitude to Dr. Thornton, for the helpful guidance he provided. Not only did he weekly take the time to extensively discuss the progress of this work, but also nearly every other interesting aspect of life; ranging from advise on comical literature to the history of British naval battles, and from the details of English spelling to those of Civilisation gaming.

I would like to thank the rest of the Multiscale Mechanics group, for granting me a significant part of their lab space for such a long time, for showing their genuine interest in this project, and for making me feel like one of their own.

It is a pleasure to thank the people of the Physics of Fluids group. The useful discussions, the inspirational chats, the gezelligheid at the coffee table and the time people took to help me with questions all contributed to a great atmosphere. I especially will remember the fun of playing soccer with the PoF United futsal team. I would like to thank Dr. Van der Meer for the insightful discussions at crucial moments during my project. I would notably like to mention the people of Studentroom A; Erik-Jan, Ivan, Wilco, Pascal, Jarich, Stef, Rianne, Michiel, the Beschermheer and others, who were always happy to help with a question or help think about a problem, whether it was of personal or professional nature, and who provided a wonderful distraction from daily responsibilities with the fun chats during coffee breaks. I would like to express my gratitude to Ceyda and Bram V., who took the time to introduce me to the complicated procedure of working with Piranha solution. I would also like to thank Gert-Wim, who designed and built important improvements to my experimental setup. I would like to thank Sander W., not only for the useful discussions but also the enthusiasm with which he approached ideas for fun Friday-afternoon experiments.

I would like to thank the MaCS group, for their help and useful discussions which helped me in the understanding of the theoretical background of the numerical models. A special thanks to Dr. Bokhove and Elena for the personal discussions and help with both the understanding the theory and the comparison of my experiments to the model.

I would like to thank mr. Zweers for showing me around in his FabLab, and the work he put into making a physical 3D model of my measurements of a breaking wave.

It is a pleasure to thank Thomas B. especially, for the inspiring daily chats and coffee walks, and who was always ready to listen to and comment on my daily worries and experiences.

I am especially thankful to Annemiek, who has continuously supported me greatly in many ways.



# Scientific Acknowledgements

Without the experimental setup as it exists today, I would not have been able to perform the experiments described in this thesis. A number of people are responsible for the currently existing Hele-Shaw cell, among which not the author. It was Onno Bokhove who came up with the original idea of studying the evolution and interaction of beaches and waves in a Hele-Shaw cell, and many thanks go to him and Wout Zweers who together spent a lot of time designing, building and testing the first version of the Hele-Shaw cell setup. A lot of time and effort were also spent by Anthony Thornton, Wout Zweers and Onno Bokhove in building and testing the second Hele-Shaw cell setup, for which I would like to express my gratitude. This was the setup used in the experiments described in this thesis. Gert-Wim Bruggert is acknowledged for the significant improvement of the wavemaker device, by installing the linear actuator and designing an improved version of the wavemaker itself, which was subsequently built by TCO. Bas Benschop is thanked for his efforts in installing the linear actuator electronics hardware, and his help with its digital control. Lastly I would like to express my severe gratitude to Boudewijn de Smeth, who lent me the sieves used for sieving the particles, trusting me with the safe and sound return of them by the end of the project.



# Bibliography

- [1] C.C. Addison and S.K. Hutchinson. The properties of freshly-formed surfaces. *Journal of the Chemical Society*, pages 943–948, 1948.
- [2] R. Albert, I. Albert, D. Hornbaker, P. Schiffer, and A.-L. Barabási. Maximum angle of stability in wet and dry spherical granular media. *Physical Review E*, 56(6):6271–6274, December 1997.
- [3] V.R. Ambati. *Forecasting water waves and currents: A space–time approach*. PhD thesis, University of Twente, The Netherlands, 2008.
- [4] K.H. Andersen, M.-L. Chabanol, and M. van Hecke. Dynamical models for sand ripples beneath surface waves. *Physical Review E*, 63:066308/1–066308/8, May 2001.
- [5] G.C. Barker and Anita Mehta. Transient phenomena, self-diffusion, and orientational effects in vibrated powders. *Physical Review E*, 47(1):184–188, January 1993.
- [6] G.K. Batchelor. *An Introduction to Fluid Dynamics*. Cambridge University Press, 1967.
- [7] J.A. Battjes. Surf similarity. In *Proc. Conf. Coastal Eng., 14th*, pages 466–479, 1974.
- [8] Daniel Blair and Eric Dufresne. Matlab particle tracking. URL <http://physics.georgetown.edu/matlab/>.
- [9] O. Bokhove, V. Zwart, and M.J. Haveman. Fluid fascinations. Publication of Stichting Qua Art Qua Science, Universiteit Twente, The Netherlands, 2010.
- [10] O. Bokhove, B. van der Horn, D. van der Meer, W. Zweers, and A. Thornton. Breaking waves on a dynamic Hele–Shaw beach. In *Conference Proceedings of the 3rd Int. Symp. on Shallow Flows*, June 4–6 2012.
- [11] Onno Bokhove. Derivation of width– and depth–averaged shallow water equations in a Hele–Shaw geometry. Private communications, 2012.
- [12] F. Cantelaube, Y. Limon-Duparcmeur, D. Bideau, and G.H. Ristow. Geometrical analysis of avalanches in a 2D drum. *Journal de Physique (France)*, 5(5):581–596, May 1995.
- [13] E. Gagarina, J. Van der Vegt, V. Ambati, and O. Bokhove. A Hamiltonian Boussinesq model with horizontally sheared currents. In *Conference Proceedings of the 3rd Int. Symp. on Shallow Flows*, June 4–6 2012.
- [14] C.J. Galvin. Breaker type classification on three laboratory beaches. *Journal of Geophysical Research*, pages 3651–3659, 1968.
- [15] David Grier, John Crocker, and Eric Weeks. Particle tracking using IDL. URL <http://www.physics.emory.edu/~weeks/idl/>.
- [16] J.L. Hansen, M. van Hecke, A. Haaning, C. Ellegaard, K.H. Andersen, T. Bohr, and T. Sams. Instabilities in sand ripples. *Nature*, 410():325, March 2001.
- [17] H.S. Hele-Shaw. The flow of water. *Nature*, 58(34):34–36, 1898.

- [18] C.R. Iribarren and C. Nogales. Protection des ports. In *Comm. 4, 17th Int. Nav. Congr.*, volume 31, page 80, 1949.
- [19] H.H. Kausch, D.G. Fesko, and N.W. Tschoegl. The random packing of circles in a plane. *Journal of Colloid and Interface Science*, 37(3):603–611, November 1971.
- [20] Andrew T. Lee, Eduardo Ramos, and Harry L. Swinney. Sedimenting sphere in a variable-gap Hele–Shaw cell. *Journal of Fluid Mechanics*, 586:449–464, 2007.
- [21] D.H. Peregrine. Breaking waves on beaches. *Annual Review of Fluid Mechanics*, 15:149–178, 1983.
- [22] F. Ribas, H.E. de Swart, D. Calvete, and A. Falqués. Modeling waves, currents and sandbars on natural beaches: The effect of surface rollers. *Journal of Marine Systems*, 88:90–101, 2011.
- [23] L. Rosenhead, editor. *Boundary Layer Theory*. Oxford University Press, 1963.
- [24] A. Stegner and J.E. Wesfreid. Dynamical evolution of sand ripples under water. *Physical Review E*, 60(4):3487–3490, October 1999.
- [25] Dominic Vella and L. Mahadevan. The ”cheerios effect”. *American Journal of Physics*, 73(9):817–825, 2005.
- [26] C.E. Vincent and D.M. Hanes. The accumulation and decay of near-bed suspended sand concentration due to waves and wave groups. *Continental Shelf Research*, 22:1987–2000, 2002.
- [27] G.B. Whitham. *Linear and nonlinear waves*. John Wiley & Sons, 1974.
- [28] L.D. Wright, J. Chappell, B.G. Thom, M.P. Bradshaw, and P. Cowell. Morphodynamics of reflective and dissipative beach and inshore systems. *Marine Geology*, 32:105–140, 1979.

# Appendix A

## Supplementary experiments

Some supplementary measurements were performed. Firstly, the possible influence of wavemaker motion to the temperature in the Hele-Shaw cell is treated. Secondly, a number of measurements determining the change of surface tension of water through time, and the influence of contamination on the surface tension are discussed. Thirdly, the properties of particles used in the beach evolution and wave dynamics experiments are examined.

### A.1 Temperature

Since the properties of the fluid may vary with temperature, it is important to know whether this is variable during the course of a measurement, and whether it is influenced by the energy added to the system due to the wavemaker motion. To examine this, the Hele-Shaw cell was cleared of wedge and particles, and the wavemaker was set to run for several hours with just water in the cell. During this time, the room temperature ( $T_1$ ) and the temperature of the water ( $T_2$ ) were measured. The parameters used in this experiment are listed in table A.1. Note, that the wavemaker frequency is the highest as used in experiments, and the amplitude is higher than during experiments, to make sure the wavemaker motion adds *at least* as much energy to the system as during the actual experiments. The measured temperatures at different times are shown in figure A.1. As may be clear, both the room and water temperature may be considered constant, and differ only a few points of a degree. Since the fluid properties of water only vary slightly with temperature in the range of interest (23-28 °C), the room temperature may be consid-

Parameter	Value
$H_0$	$110 \pm 2$ mm
$f_{\text{wm}}$	1.3 Hz
$\theta_{\text{wm}}$	$29 \pm 1^\circ$

Table A.1: Parameters of temperature experiment, which investigates the possible rise in temperature in the Hele-Shaw cell due to the wavemaker motion during experiments.

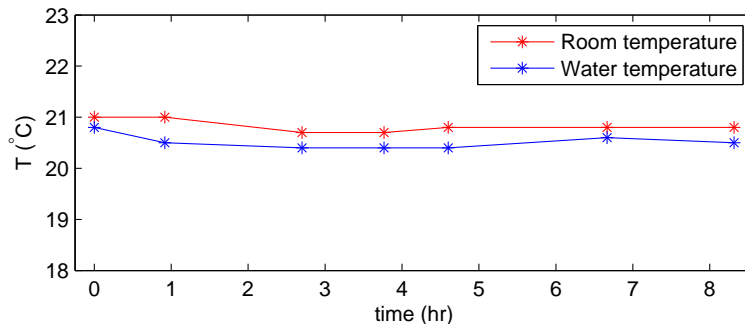


Figure A.1: Temperature experiment results, showing no measurable temperature rise due to the energy added to the system through the wavemaker motion.

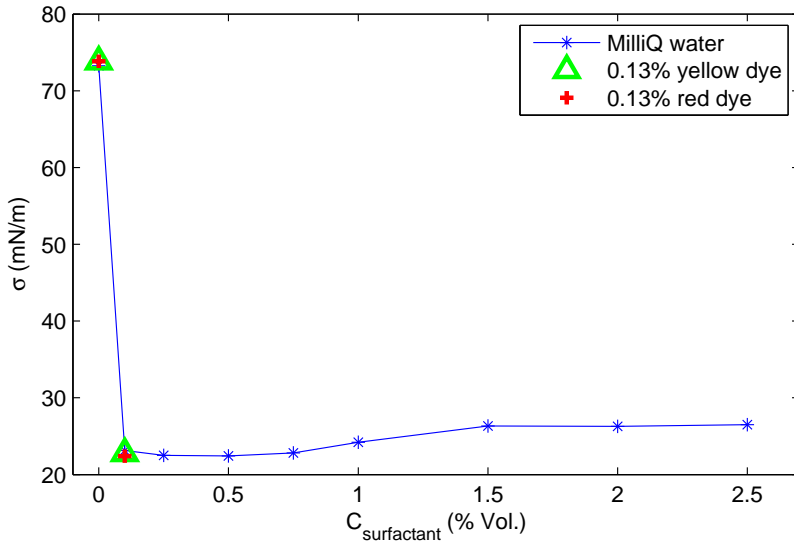


Figure A.2: Surface tension of MilliQ<sup>®</sup> water versus concentration of Dreft<sup>®</sup> surfactant.

ered a close enough approximation of the water temperature. No measurable temperature rise, due to the continuous addition of energy to the system through the motion of the wavemaker, has been observed.

## A.2 Surface tension measurements

A few experiments were conducted to determine the possible influence on the used MilliQ<sup>®</sup> water's surface tension of different processes and additions to the water.

Firstly, the influence of dye and surfactant (both applied in wave dynamics experiments) on the surface tension of the water was investigated. These measurements have been done using the OCA apparatus of the Physics of Complex Fluids group, which essentially uses the Pendant Drop method to determine the surface tension. The surface tension of water with different concentrations of Dreft<sup>®</sup> surfactant was measured; an extensive series without dye, and a few points with dye to compare. The results are shown in figure A.2. Two things are interesting about this figure. First, the surface tension minimum lies at 0.5% concentration, and *rises* again with higher concentration of surfactant. Although this seems counter-intuitive, such a minimum is not unknown in literature [1]. Secondly, the results with dye overlap perfectly with the results without dye. Therefore, the dye may be assumed to have no effect on the surface tension.

On a longer time scale, the surface tension of a drop of water is expected to decrease with time. This is due to dust particles getting picked up from the environment, acting as surface active components. To see whether this really happens and if so, at what rate, three surface tension measurements on a longer time scale have been performed, using the pendant drop method; one with MilliQ<sup>®</sup> water, one with MilliQ<sup>®</sup> water containing red dye and one with tap water. During these measurements the volume of the pendant drop was monitored and kept constant by continuous addition of the liquid examined. The results are shown in figure A.3. Interesting to see is that the three measurements show similar behaviour: first a period of relatively slow decay, then a transition to a larger decay rate. Note the vast difference in time scales observed between the three measurements. This may be caused by differences in environment between the measurements (e.g., different airflows, different contamination in the surrounding air), but more measurements would be needed to determine the exact cause of these differences. One thing being clear is that the surface tension might drop significantly within a matter of hours to days.

Just out of curiosity, the surface tension of the pure red dye has also been measured. The result of this is shown in figure A.4a. Surprisingly, the surface tension measured is rising with time. What this is caused by is unknown. The drop surface size in the same measurement has been plotted in fig. A.4b, which was

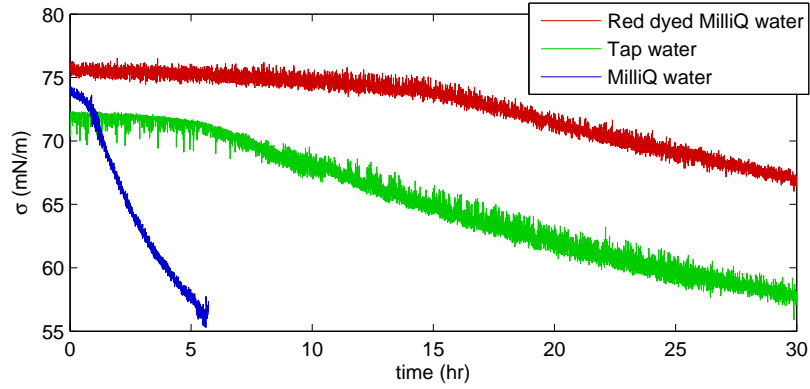


Figure A.3: Three long-term surface tension measurements of water using the pendant drop method.

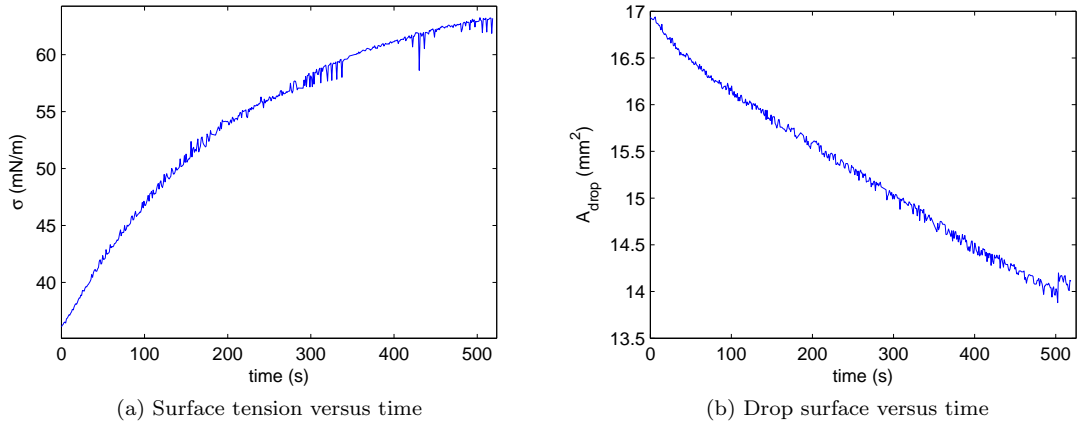


Figure A.4: Surface tension measurement of pure red dye.

not kept constant because of the relatively short timescale of this measurement.

When considering the surface tension of the water, an essential question is whether the surface tension of the water inside the Hele-Shaw cell would be influenced by possible contamination during the experiments. To study this, samples were examined of water used in measurements during one day of the beach evolution measurement series. These water samples were obtained during the usual drainage of the used water from the setup at the end of each measurement (see section 4.2). The surface tension of each sample was measured three times using the pendant drop method, the result being the average of the three. The measured surface tensions are listed in table A.2, along with that of clean MilliQ<sup>®</sup> water for comparison. The times in the middle column are the measurement times of the beach evolution measurements from which the samples were taken. They indicate the time each sample has been present in the Hele-Shaw cell. The deviations from the mean was less than the error of the measuring device in all cases, which was approximately 1 mN/m.

Note, that in all measured samples dust particles have been observed floating inside the pendant drops. These particles are believed to be tiny fragments of Gamma Alumina particles. Note also, that no significant decrease of surface tension has been measured. This despite the sometimes long measurement times of several hours, during which the water was present in the Hele-Shaw cell.

Measurement number	Measurement time (min)	Sample surface tension (mN/m)
41	128	$71.0 \pm 1$
42	121	$71.1 \pm 1$
43	84	$71.4 \pm 1$
44	6	$71.3 \pm 1$
45	142	$71.4 \pm 1$
MilliQ <sup>®</sup> water	0	$71.9 \pm 1$

Table A.2: Measured surface tensions of water samples from beach evolution measurements. The measurement time indicates the time that the water, from which the sample was taken, has been present in the Hele-Shaw cell during the beach evolution measurement. The measurement numbers correspond to those in table D.2.

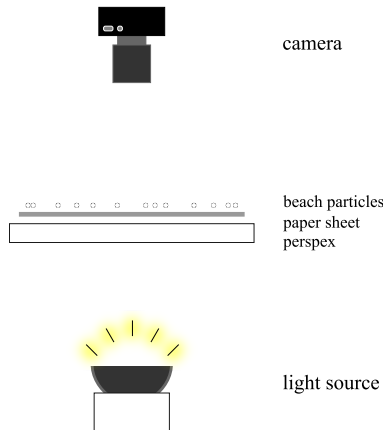


Figure A.5: Schematical representation of the size distribution measurement setup.

## A.3 Bed particles

Two types of particles were used as particles for the bed; Gamma Alumina (GA) particles during the beach evolution experiments, and glass particles during the wave dynamics experiments. The measurements of size distribution, density and porosity of the particles is described in detail, followed by a short treatment about the glass particles' hydrophobicity.

### A.3.1 Size distribution

The size distribution of the bed particles used in the beach evolution and wave dynamics experiments has been measured as follows. A horizontal piece of transparent perspex is lighted from below. A piece of paper is put on top of the perspex to diffuse the light. The beach particles are spread out on top of the paper and perspex. A Nikon 5100 camera with Sigma 18-200 mm zoom lens is positioned above all this, facing downward. A grid was used to check for lens distortions and pixel-to-mm ratio determination. The setup for this measurement is schematically shown in figure A.5.

Since a narrow size distribution around  $d = 1.8$  mm is desired, both sets of particles have been sieved with sieves of 1.7 and 2.0 mm gap width. The size distributions of the sieved GA and glass particles are shown in figure A.6.

### A.3.2 Density and porosity

The density and porosity of the bed particles was measured as follows. First, a certain amount of water is put into a measurement cup. The volume of water is then read out,  $V_1$ , and the mass measured,  $M_1$ . Next,

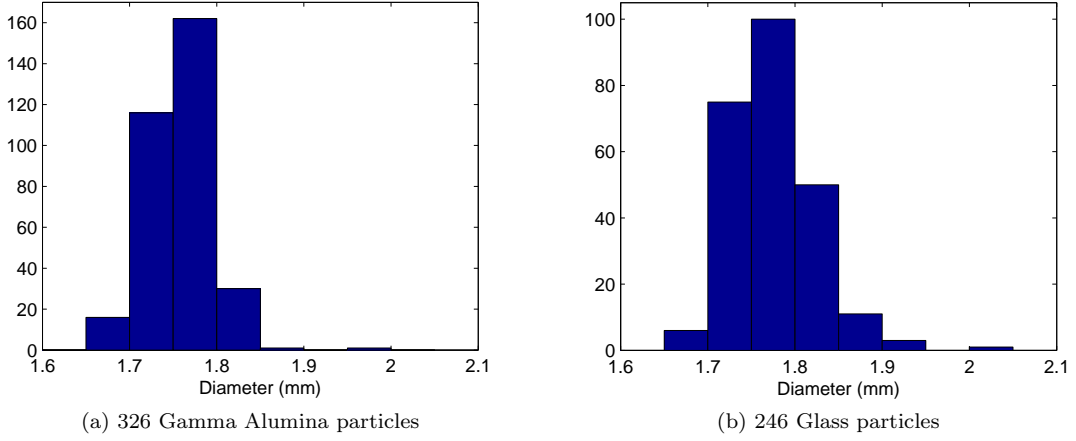


Figure A.6: Size distributions of sieved beach particles.

a certain amount of beach particles is poured in the water. The new volume and mass are then measured,  $V_2$  and  $M_2$ . If the beach particles are porous, it is important to measure  $V_2$  as quickly as possible, since it should reflect the total volume of the system with the particle pores *unfilled*. In the case of the GA particles,  $V_2$  was measured within  $\sim 15$  seconds after the first particle hit the water. Next, the particles are left submerged until no microbubbles are observed rising to the surface anymore, i.e. until all particle pores are filled with water. This usually takes around 90 minutes. After that, the blend is stirred with a small plastic stick, removing any air bubbles remaining. Then, the volume and mass are measured again, being  $V_3$  and  $M_3$ .

From these three volumes and masses, four interesting parameters are determined. The *effective porosity* is defined as the ratio of the volumes of the filled pores and the total particle volume,

$$\Phi_{\text{eff}} = \frac{V_{\text{filled pores}}}{V_{\text{total}}} = \frac{V_2 - V_3}{V_2 - V_1}, \quad (\text{A.1})$$

the *apparent density* is the ratio of the mass of the particle material and its volume, i.e. the density of the particles with unfilled pores,

$$\rho_{\text{app}} = \frac{M_{\text{material}}}{V_{\text{total}}} = \frac{M_2 - M_1}{V_2 - V_1}, \quad (\text{A.2})$$

the *effective density* is the ratio of the mass of the particle material plus the mass of the filled pores and the particle volume, i.e. the density of the particles with filled pores,

$$\begin{aligned} \rho_{\text{eff}} &= \frac{M_{\text{material}} + M_{\text{filled pores}}}{V_{\text{total}}} \\ &= \frac{M_{\text{m}}}{V_{\text{t}}} + \frac{\rho_{\text{water}} V_{\text{fp}}}{V_{\text{t}}} \\ &= \rho_{\text{app}} + \rho_{\text{water}} \Phi_{\text{eff}} \\ &= \frac{(M_2 - M_1) + \rho_{\text{water}}(V_2 - V_3)}{V_2 - V_1}, \end{aligned} \quad (\text{A.3})$$

and the *real porosity* is defined as the ratio of the total volume of pores (including the unfillable ones) and the total particle volume,

$$\begin{aligned} \Phi_{\text{real}} &= \frac{V_{\text{all pores}}}{V_{\text{total}}} = \frac{V_{\text{total}} - V_{\text{material}}}{V_{\text{total}}} \\ &= 1 - \frac{\frac{M_{\text{total}}}{\rho_{\text{total}}}}{\frac{M_{\text{total}}}{\rho_{\text{material}}}} \\ &= 1 - \frac{\rho_{\text{app}}}{\rho_{\text{material}}}, \end{aligned} \quad (\text{A.4})$$

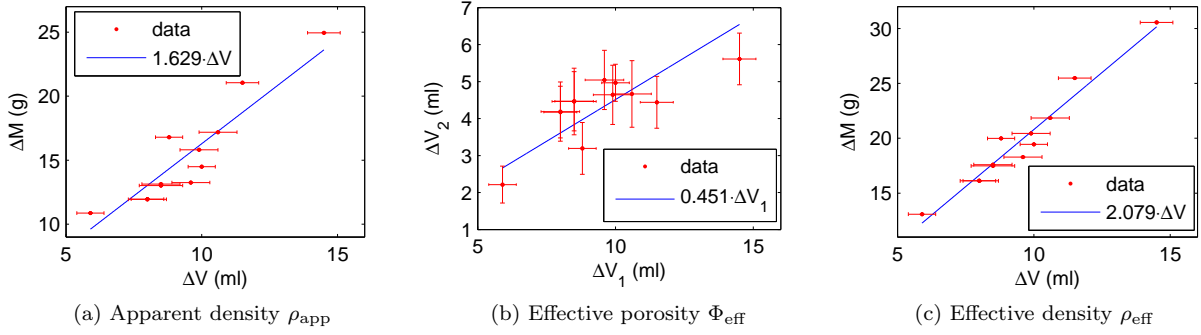


Figure A.7: Density and porosity determination by linear regression.

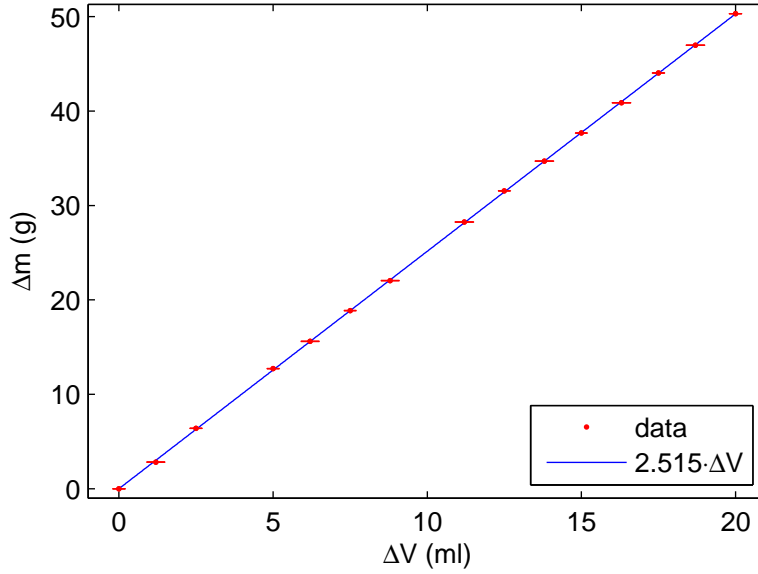


Figure A.8: Density measurement of the glass particles. The graph includes error bars.

in which  $\rho_{\text{material}}$  is the density of the material the particles are made off.

In the case of the GA particles,  $\rho_{\text{material}}$  was given by the manufacturer, being  $3.42 \text{ g cm}^{-3}$ . The water density was taken to be  $0.9982_{0.9970}^{0.9991} \text{ g cm}^{-3}$ . The density and porosity measurement was done twelve times. Three of the four looked-for parameters, namely  $\Phi_{\text{eff}}$ ,  $\rho_{\text{app}}$  and  $\rho_{\text{eff}}$ , are a fraction of two measurable quantities. Linear regression through the origin (LTO) can be used to determine the value of these. The resulting graphs for  $\Phi_{\text{eff}}$ ,  $\rho_{\text{app}}$  and  $\rho_{\text{eff}}$  are shown in figure A.7.

The fourth parameter, the real porosity  $\Phi_{\text{real}}$ , is not a fraction of two measured quantities. To get this real porosity, it is calculated from each measurement individually, after which the mean and standard deviation are calculated. This gives a  $\Phi_{\text{real}}$  of 0.53 with a standard deviation of 0.05.

The glass particles were found to be non-porous. Their density was measured by taking a fixed volume of water, measuring its weight, and then alternately adding some particles and measuring both the volume and weight. The result is shown in figure A.8. The density found is  $2.515 \pm 0.03 \text{ g cm}^{-3}$ . This is slightly different from the density mentioned by the manufacturer, which was  $2.50 \text{ g cm}^{-3}$ , although this quantity falls within the error limits.

### A.3.3 Hydrophobicity of the glass particles

The glass particles proved to be very hydrophobic. This caused many particles to ‘stick’ to the water free surface upon interaction with it, as was described by Vella and Mahadevan [25]. Besides that, tiny air bubbles remained attached to many of the particles after immersion in the water. Like the porosity of the GA particles, this behaviour is undesired because it is hard to model. Also, this behaviour is different from that of natural sand. It is caused by a colouring applied by the manufacturer and made the particles opaque, which was necessary for correct detection of the particles by the analysis program used.

Treatment with three different chemicals has been done in an attempt to make the particles hydrophilic. Treatment with ethanol (99.8%) and acetone proved unsuccessful. Treatment with Piranha solution (3:1 mixture of concentrated sulfuric acid and hydrogen peroxide solution) resulted in the particles becoming hydrophilic. However, this caused the particles to lose too much of their colouring, becoming partly translucent and impossible to detect accurately by the analysis program. Even a short treatment with Piranha solution, lasting only approximately 20 seconds, rendered the particles undetectable.

The fact that the glass particles are non-porous and relatively unbreakable makes them more suitable for usage in Hele-Shaw cell experiments as compared to the Gamma Alumina particles. Therefore, a continued search for a solution to this hydrophobicity problem is recommended.

## A.4 Wavemaker motion

The wavemaker is essentially a double welding wire of diameter 1.6 mm welded together at their two extremities. This is then attached to a pivot point, which in turn is rotated about its axis due to a mechanical connection with a Copley Controls ThrustTube<sup>®</sup> linear actuator (type STC-2506-S). This actuator itself is driven in a sinusoidal motion. The linear actuator is controlled by a Copley Controls Xenus<sup>®</sup> controller (type XTL-230-18-S). This controller is first programmed through the CME2 software delivered with it, and controlled during measurements by MATLAB through its RS232 port.

To examine the angular motion of the wavemaker, the linear actuator was programmed to perform a symmetric, sinusoidal motion at a typical frequency of  $f_{wm} = 1$  Hz and amplitude 30 mm. This is the same amplitude as used in the beach evolution and wave dynamics experiments. A MATLAB routine has been written to analyse high-speed images of the wavemaker and extract its angular position. The resulting angular motion of the wavemaker at a frequency of 1.0 Hz is shown in figure A.9. The one period shown in this figure is representative of the 8 periods the cosine fit was made to ( $R^2 = 0.999$ ).

It can be seen that the wavemaker motion deviates from the expected sinusoidal trajectory around the turning point. This is most likely caused by the presence of the spring in the connection between wavemaker and linear actuator.

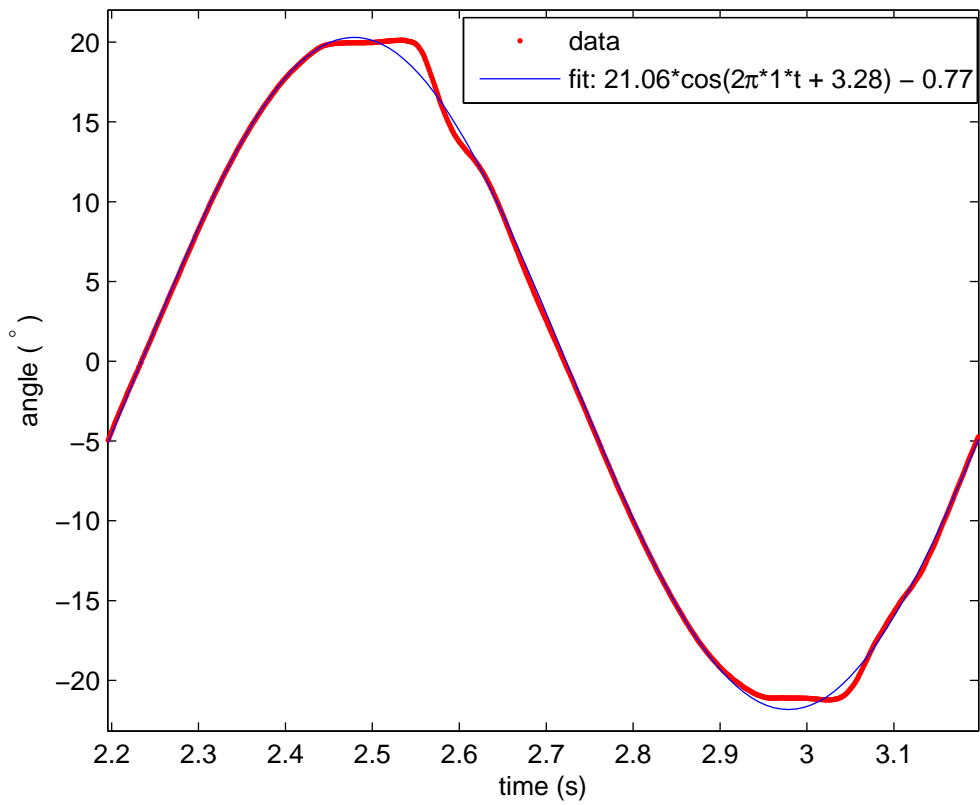


Figure A.9: One period of angular wavemaker motion for  $f_{wm} = 1$  Hz.

## Appendix B

### Wedge details

Figure B.1 shows a detailed drawing of the polycarbonate wedge used in the Hele-Shaw experiment. Notice the not-exactly symmetrical shape. A tiny deviation of the shape from a perfectly symmetrical truncated triangle, at its bottom left corner, allows for easy removal and reinstallation of the wedge during thorough cleaning of the Hele-Shaw cell.

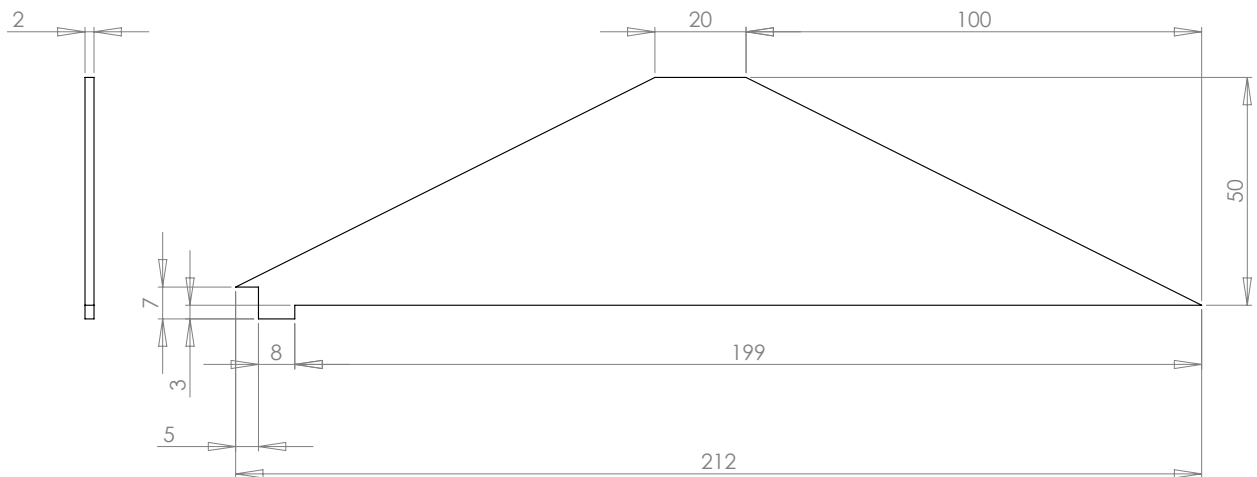


Figure B.1: Schematic drawing of the wedge. Notice the slight deviation from symmetry at the bottom left, which allows for easy installment in and removal from the Hele-Shaw cell.



## Appendix C

# Beach evolution: precursory measurements

This appendix shortly treats the beach evolution measurement series performed in December 2011, from hereon referred to as the precursory measurements, and its results. The parameters used in this series are listed in table C.1. Note the ‘weird’ choice of wavemaker frequencies; all lie 0.001 Hz above more ‘logical’ values. This is done to give an intentional mismatch with the camera timing. In this way, different phases in the wavemaker period are photographed over 100 frames. This was done to get an idea of the different wave phenomena occurring for different wavemaker frequencies and bed profiles. At the time these measurements were done, the experiments described in chapter 5 were not yet performed.

Besides some minor geometrical differences, two important differences between these measurements and the ‘new’ measurements done in may-june 2012 should be noted. Firstly, the wavemaker angular amplitude  $\theta_{\text{wm}}$ . While for the new measurements the wavemaker motion is quite symmetric and has an amplitude of  $\sim 21^\circ$ , in these precursory measurements the wavemaker motion was asymmetric. This was caused by an error in programming the linear motor, which caused the motor to move 40 mm to one side and 20 mm to the other side of the position in which the wavemaker was vertical during each wavemaker period, instead of the 30 mm - 30 mm movement it was supposed to make. This resulted in a wavemaker movement with different amplitudes left and right of the vertical position, namely around  $29^\circ$  left, and around  $13^\circ$  right. Figure C.1 illustrates the difference in wavemaker motion during the precursory (red) and new (blue) measurements. As a consequence of this difference, the wavemaker came less close to the bed and plastic wedge during the precursory measurements than it did during the new measurements. Also, the wavemaker was positioned  $\sim 13$  mm closer to the bed in the new measurements, which is clear from the differences in the horizontal wedge and wavemaker positions  $x_w$  and  $x_{\text{wm}}$  and the wavemaker pivot-to-rod distance  $\Delta_{\text{wm}}$ . This is probably the reason why during the precursory measurements undisturbed bed evolution was observed for parameters where during the new measurements heavy suction occurred.

Secondly, not all particles present in the bed were visible during the precursory measurements; due to the geometry of the setup, the lower part of the bed and a small section of the bed at the right-most end of the setup were invisible from the camera’s point of view. This was corrected in the new measurement series by adding fixed, perspex strips to the bottom and sides of the Hele-Shaw cell.

Table C.2 lists the actual measurements done in this series, in order of performance. Note that these measurements, like the measurements mentioned in chapter 4, were randomised before they were performed.

Figure C.2 shows the phase diagrams obtained from the precursory measurements. For  $B_0 = 20$  mm, no sed-

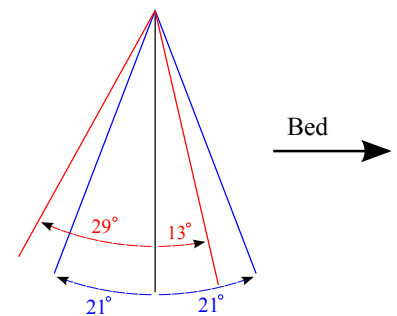


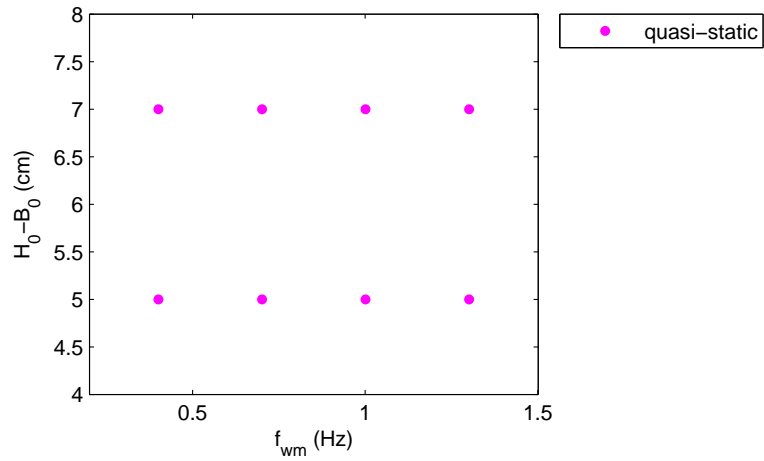
Figure C.1: Illustration of difference in wavemaker motion during precursory (red) and new (blue) measurements.

Varied parameters		Fixed parameters	
Parameter	Values	Parameter	Value
$H_0 - B_0$	$\in [10, 30, 50, 70] \pm 3$ mm	$L$	$980 \pm 3$ mm
$B_0$	$\in [20, 50, 80] \pm 2$ mm	$d$	$2.0 \pm 0.05$ mm
$f_{wm}$	$\in [0.401, 0.701, 1.001, 1.301]$ Hz	$x_w$	$372 \pm 1$ mm
		$l_w$	$212 \pm 0.1$ mm (app. B)
		$h_w$	$5 \pm 0.1$ mm (app. B)
		$t_w$	$20 \pm 0.1$ mm (app. B)
		$x_{wm}$	$205 \pm 3$ mm
		$\Delta_{wm}$	$11 \pm 0.5$ mm
		$h_{wm}$	$340 \pm 2$ mm
		$l_{wm}$	$333 \pm 2$ mm
		$\theta_{wm}$	asymmetric, $\sim 13 - 29^\circ$
		$T$	$20-25$ °C
		$f_\rho$	$\rho_{water}$
		$f_\mu$	$\mu_{water}$
		$\sigma$	$\sigma_{air-water}$ (app. A.2)
		$\rho_b$	$2.08 \pm 0.2$ g cm $^{-3}$ (app. A.3.2)
		$\Phi_b$	$0.45 \pm 0.09$ (app. A.3.2)
		$D_b$	$1.8 \pm 0.1$ mm (app. A.3.1)

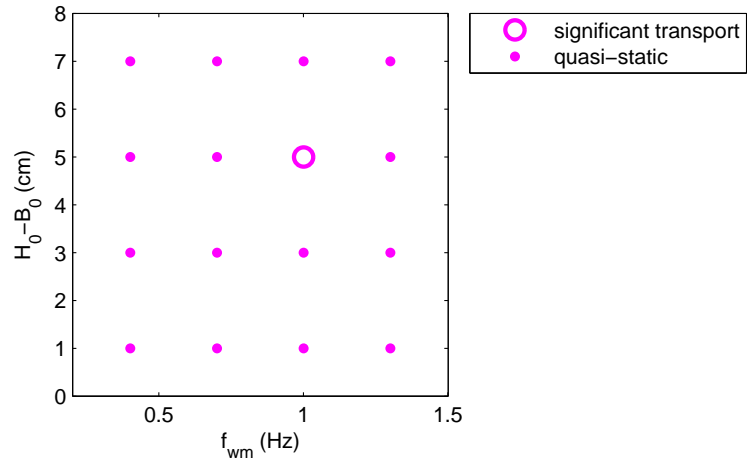
Table C.1: Parameter values of december 2011 beach evolution measurement series.

$B_0 = 80$ mm			$B_0 = 20$ mm			$B_0 = 50$ mm		
No.	$f_{wm}$ (Hz)	$H_0 - B_0$ (mm)	No.	$f_{wm}$ (Hz)	$H_0 - B_0$ (mm)	No.	$f_{wm}$ (Hz)	$H_0 - B_0$ (mm)
1	1.001	50	17	0.401	50	25	0.401	30
2	1.301	60	18	1.301	70	26	1.001	10
3	0.401	70	19	0.401	70	27	1.301	50
4	1.001	10	20	1.001	50	28	1.001	50
5	0.401	10	21	1.001	70	29	1.301	30
6	1.001	30	22	0.701	70	30	0.401	10
7	0.701	10	23	0.701	50	31	1.301	70
8	0.401	30	24	1.301	50	32	0.701	10
9	1.301	50				33	1.001	30
10	0.701	30				34	0.701	50
11	1.301	30				35	0.401	50
12	0.701	70				36	0.401	70
13	1.301	10				37	0.701	30
14	0.701	50				38	1.301	10
15	1.001	70				39	0.701	70
16	0.401	50				40	1.001	70

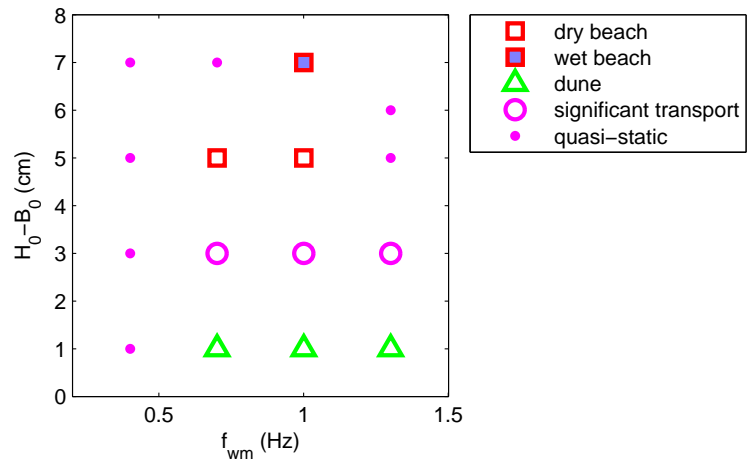
Table C.2: December 2011 beach evolution measurements in performed order.



(a)  $B_0 = 20$  mm

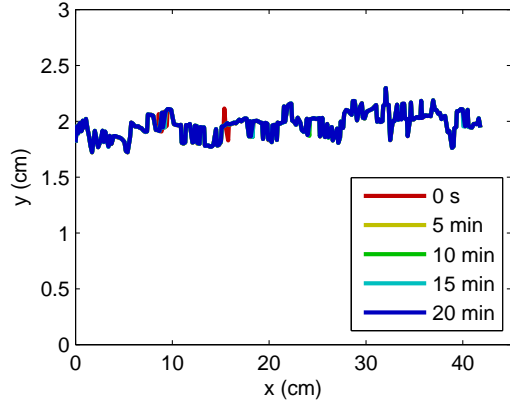


(b)  $B_0 = 50$  mm

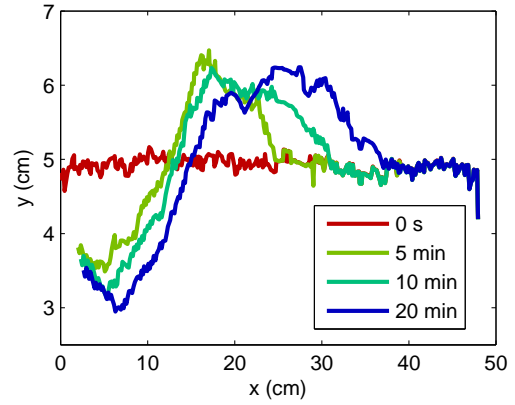


(c)  $B_0 = 80$  mm

Figure C.2: Phase diagrams of all GA-beads beach evolution measurement series.

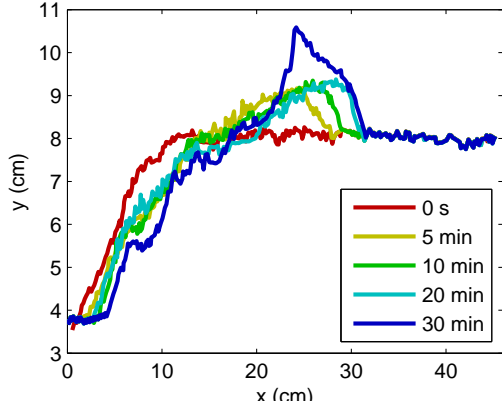


(a) Static bed;  $B_0 = 20$  mm,  $(H_0 - B_0) = 50$  mm,  $f_{wm} = 1.001$  Hz. Water depth 7 cm.

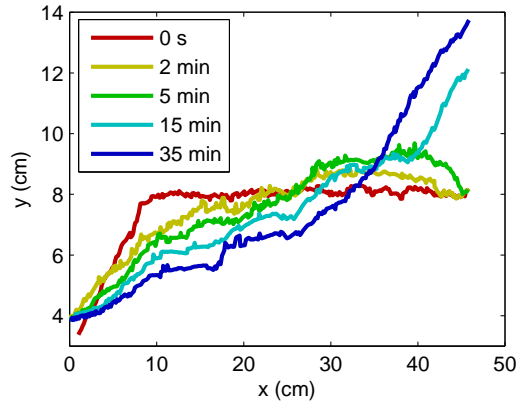


(b) Significant transport;  $B_0 = 50$  mm,  $(H_0 - B_0) = 50$  mm,  $f_{wm} = 1.001$  Hz. Water depth 10 cm.

Figure C.3: Some bed evolutions of  $B_0 = 20$  and 50 mm.



(a) Dune formation;  $B_0 = 80$  mm,  $(H_0 - B_0) = 10$  mm,  $f_{wm} = 1.001$  Hz. Water depth 9 cm.



(b) Beach formation;  $B_0 = 80$  mm,  $(H_0 - B_0) = 50$  mm,  $f_{wm} = 0.701$  Hz. Water depth 13 cm.

Figure C.4: Some bed evolutions of  $B_0 = 80$ .

iment transport takes place in any of the measurements. As an example, the evolution of the measurement with  $(H_0 - B_0) = 50$  mm and  $f_{wm} = 1.001$  Hz is shown in figure C.3a. Note the almost perfect overlap of all beach profiles. The initial flat bed is significantly lower than the wedge height; all of the bed is effectively situated in the wedge's wake, where the flow is not strong enough to cause any sediment to be replaced.

For  $B_0 = 50$  mm, the initial bed is of the same height as the wedge. The only measurement in which significant sediment transport is observed is for  $B_0 = 50$  mm,  $(H_0 - B_0) = 50$  mm and  $f_{wm} = 1.001$  Hz. C.3b shows the evolution of this measurement. Most of the sediment transport takes place within the first 6 minutes. In this time, a hole is dug in the bed just behind the wedge, and the sediment coming from it is deposited onto a heap just beside it. For the rest of the measurement time, this pile of sediment is just moving downstream slowly.

For  $B_0 = 80$  mm, 5 different steady beach morphologies are observed: dunes, dry beaches, a wet beach, significant transport and quasi-static. At low frequency (0.401 Hz), hardly any sediment transport is observed. At higher frequencies different phenomena occur. At  $(H_0 - B_0) = 10$  mm 3 dunes are created. A typical dune formation is shown in figure C.4a. An initial heap of newly transported sediment forms just behind the wedge. While moving downstream, it keeps growing until at some point it reaches the free surface. Since at this point the heap has not reached the right end of the setup yet, it effectively forms a dune with the waves

coming in from the left (upstream) and a small, relatively ‘calm’ lake on the right. The free surface of this lake will still be moving up and down slowly, due to the porous structure of the bed. At  $(H_0 - B_0) = 30$  mm, significant sediment transport takes place, but neither a dune nor a beach is created. At  $(H_0 - B_0) = 50$  mm, dry beaches are formed at  $f_{\text{wm}} = 0.701$  and  $0.1001$  Hz. The typical formation of a beach is shown in figure C.4b. A heap is formed like in significant transport, but now it has a chance to travel all the way to the end of the setup, and forms a beach. Strangely enough, very little sediment transport is observed at  $f_{\text{wm}} = 1.301$  Hz. At  $(H_0 - B_0) = 60$  and  $70$  mm, nothing happens except at  $f_{\text{wm}} = 0.701$  Hz, where a wet beach occurs.



## Appendix D

# GA beach measurements

As discussed in section 4.2, the measurement series for the Gamma Alumina beads beach evolution was done in a randomized order. Tables D.1 and D.2 show the varied parameters for these measurements, in the order in which the measurements were performed.

$B_0 = 60$ mm			$B_0 = 50$ mm		
No.	$f_{\text{wm}}$ (Hz)	$H_0 - B_0$ (mm)	No.	$f_{\text{wm}}$ (Hz)	$H_0 - B_0$ (mm)
1	0.9	10	21	0.9	30
2	0.7	70	22	0.9	70
3	0.9	50	23	1.0	30
4	1.0	50	24	1.0	70
5	0.9	70	25	0.7	30
6	1.3	50	26	0.9	10
7	1.0	70	27	1.3	30
8	0.7	50	28	0.7	10
9	1.3	30	29	1.3	70
10	1.3	70	30	1.1	70
11	1.0	30	31	1.0	50
12	0.7	30	32	1.1	30
13	1.0	10	33	0.7	70
14	1.1	10	34	1.1	10
15	1.1	50	35	1.3	50
16	0.9	30	36	1.0	10
17	1.1	70	37	1.1	50
18	1.3	10	38	0.7	50
19	0.7	10	39	0.9	50
20	1.1	30	40	1.3	10

Table D.1: Gamma-Alumina beach experiments in performed order; part 1

$B_0 = 80$ mm			$B_0 = 70$ mm		
No.	$f_{\text{wm}}$ (Hz)	$H_0 - B_0$ (mm)	No.	$f_{\text{wm}}$ (Hz)	$H_0 - B_0$ (mm)
41	1.1	30	61	1.3	30
42	0.9	70	62	0.9	50
43	0.9	50	63	1.1	30
44	1.3	70	64	0.7	70
45	0.7	10	65	0.7	10
46	1.3	30	66	1.1	70
47	1.3	10	67	1.0	50
48	1.1	50	68	1.0	30
49	0.7	50	69	1.3	50
50	0.9	10	70	1.0	70
51	1.0	10	71	1.1	10
52	1.1	10	72	1.3	10
53	0.7	70	73	1.1	50
54	1.1	70	74	0.9	70
55	0.7	30	75	0.7	50
56	1.0	70	76	0.9	10
57	1.0	30	77	1.3	70
58	1.3	50	78	0.7	30
59	1.0	50	79	0.9	30
60	0.9	30	80	1.0	10

Table D.2: Gamma-Alumina beach experiments in performed order; part 2

# Appendix E

## Beach evolution analysis

The ten-second interval recordings of the beach evolution were analysed in MATLAB. A schematic drawing of the analysis program structure is shown in figure E.1. The analysis is done in several steps inside the function (`cl_main.m`). After the measurement, the raw images are saved in a certain directory, say `path\`. A measurement-specific tweak file, `mtweak.m`, is added to that path, containing measurement specific data like the meter-per-pixel ratio, crop settings and the measurement's  $B_0, H_0 - B_0$  and  $f_{wm}$ . The script `GA_beach_evolution_tweak.m` is part of the analysis programs and contains the tweak variables for the different following analysis functions. Next, the image cropping in `imcrop_b.m` is rather trivial; the region of interest containing the beach particles is cut out of the raw recorded image, resulting in an image like the one in figure E.2a.

### E.1 Coastal region

To prevent any noise to end up in the final set of particle locations, the beach is first roughly located. This is done by `cblob.m`:

```
1 se = strel('disk',imdildisk);           % imdilatae discs
2 Alblob = imdilate(im2,se);             % imdilate
3 Alblob = imfill(Ablob,'holes');        % fill holes in image
4
5 %% remove all objects except the coast
6 % find largest object (=coast)
7 objects = regionprops(Ablob,'Area','BoundingBox','Image');
8 ncoast = 1;
9 for i=2:length(objects)
10     if objects(i).Area > objects(ncoast).Area
11         ncoast = i;
12     end
13 end
14
15 % place coast in 'clean' background
16 Alblob = zeros(size(Ablob,1),size(Ablob,2));
17 wbb = objects(ncoast).BoundingBox;
18 Alblob(ceil(wbb(2)):ceil(wbb(2))+wbb(4)-1, ...
19     ceil(wbb(1)):ceil(wbb(1))+wbb(3)-1) ...
20     = objects(ncoast).Image;
21
22 end
```

`cblob.m` returns a black-and-white image in which the beach region is white and everything else is black, `A1blob`. This output is shown in figure E.2b.

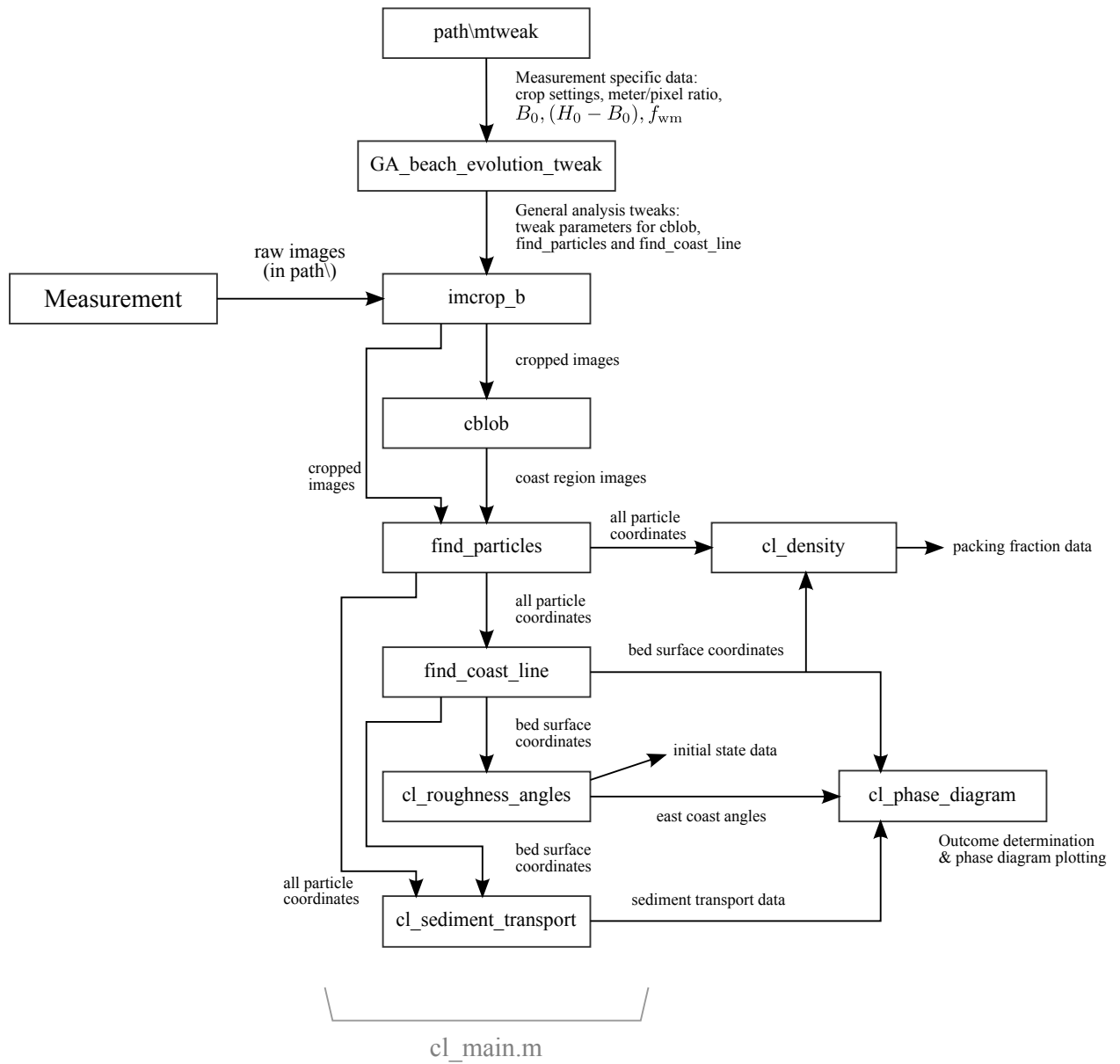


Figure E.1: Beach evolution analysis program structure.

## E.2 Particle positions

The program `find_particles.m` then uses the cropped image `A1crop` and `A1blob` as input, and finds the locations of all beach particles in each photograph:

```
1 function indcoor = findparticles(A1crop,A1blob,ptweak)
2
3 %% initial manipulation
4 A=rgb2gray(A1crop);           % grayscale image
5 A=255-A;                     % invert: dark particles become bright spots
6 A = double(A).*A1blob;       % keep only particles in A1blob region (=coast bulk)
7
8 %% apply IDL method
9 im = bpass(A,1,ptweak.ps);   % apply bandpass filter based on particle size
10 pk = pkfnd(im,ptweak.pthresh,ptweak.psize); % find bright peaks
11 cnt = cntrd(im,pk,ptweak.csize); % find particle centroids
12
13 %% output
14 % indcoor:  particle coordinates in A1crop figure; horizontal = (:,1), vertical = (:,2)
15 indcoor=[];
16 indcoor(:,1) = cnt(:,1);      % horizontal coordinate = horizontal matrix position
17 indcoor(:,2) = size(A1crop,1) - cnt(:,2)+1; % vertical coordinate = vertical matrix size
18                                     % - vertical matrix position + 1
19 indcoor = sortrows(indcoor,1); % sort on x-location
20
21 end
```

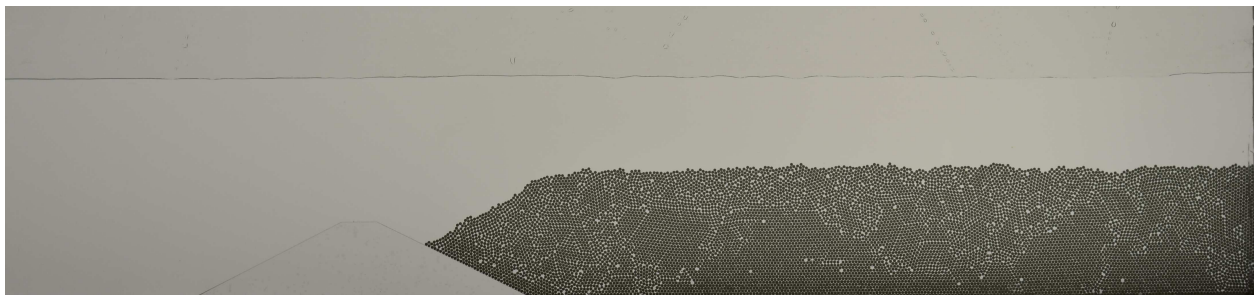
This program uses the Matlab Adaptation by Daniel Blair and Eric Dufresne [8] of IDL Particle Tracking software developed by David Grier, John Crocker, and Eric Weeks [15]. Its output is an  $N \times 2$  array of particle location coordinates. The particle coordinates are shown in figures E.2c and E.2d.

## E.3 Beach surface

From the acquired particle location-time data, the particles actually belonging to the beach *surface* are determined. This is done by the function `find_coast_line.m`:

```
1 function indcoor = find_coast_line(indc,cltweak)
2
3 %% TWEAK
4 ps = cltweak.ps;             % estimated particle size: bin width
5 step = cltweak.step;        % step size: distance between centers of bins
6
7 %% make intervals & find top layer particles
8 indcoor = [];
9 for i=0:round(indc(end,1)/step)+1
10     indci = indc(indc(:,1)<=(i*step+ps/2)&indc(:,1)>(i*step-ps/2),:);
11     if ~isempty(indci)
12         [~,I] = max(indci(:,2));
13         indcoor(end+1,:) = indci(I,:);
14     end
15 end
16
17 % output: beach surface coordinates
18 indcoor = unique(indcoor,'rows'); % remove double entries and sort for x position
19
20 end
```

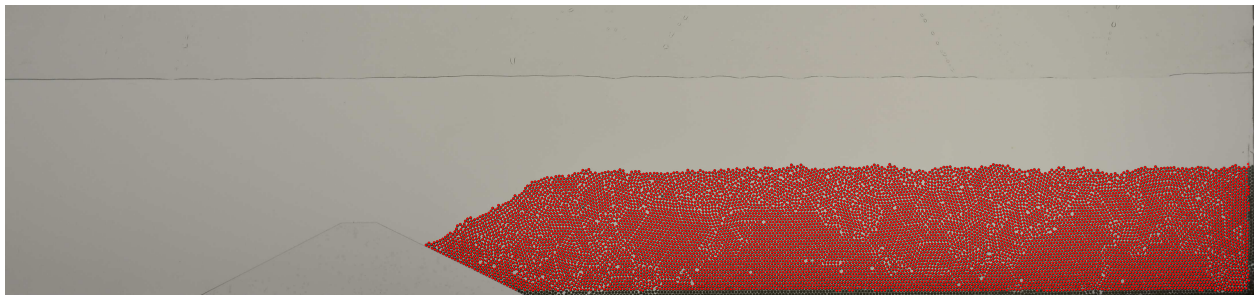
Here, `indc` is the array of particle coordinates from `find_coast_line.m`. `indcoor` is a similar array of beach surface particles. `find_coast_line.m` determines the beach surface particles as follows. It first divides the particle data into bins whose centres are `cltweak.step` pixels apart, and which are `cltweak.ps` wide. Of all the particles in each bin, the highest one (i.e., with largest vertical coordinate) is seen as belonging



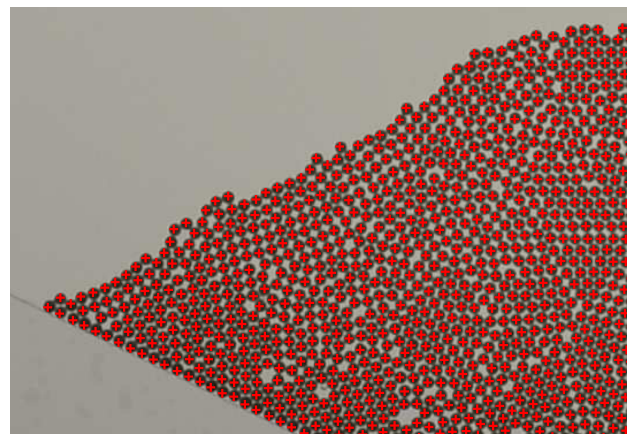
(a) A1crop: cropped image



(b) A1blob: coastal region



(c) Particle locations



(d) Zoom in particle locations

Figure E.2: Input and output of `cblob.m` and `find_particles.m`.

to the beach surface. Since for some tweak settings the bins are overlapping, all double entries are removed after having run through all bins.

## E.4 Initial state and east coast angles

Using the obtained beach surface data, `cl_roughness_angles.m` analyses the initial beach state and determines the angles of the east (right-most) part of the beach:

```

1 function coast = cl_roughness_angles(indc,xla,qeast)
2 if ~exist('qeast','var')
3     qeast = 0;
4 elseif strcmp(qeast,'east')
5     qeast = 1;
6 end
7
8 %% Roughness and angle analysis
9 % limit analysis to possibly given range (xla)
10 if ~isempty(xla)
11     bs = indc( indc(:,1)>=xla(1) & indc(:,1)<=xla(2),:);
12 else bs = indc;
13 end
14
15 L = max(bs(:,1)) - min(bs(:,1));           % beach length
16
17 %% East coast trend line and angle
18 x_mid = min(bs(:,1)) + 2*L/3;             % left-most x-coordinate of beach east part
19 bs_east=[];
20 for i=1:size(bs,1)
21     if bs(i,1)>=x_mid; bs_east=bs(i:end,:); break; end
22 end
23 p2 = polyfit(bs_east(:,1),bs_east(:,2),1); % linear fit
24 ang2 = atand(p2(1));                      % angle is inv. tangent of slope, which is p1(1)
25
26 x2 = linspace(min(bs_east(:,1)),max(bs_east(:,1)),1E3); % for plotting
27 f2 = polyval(p2,x2);                     % for plotting
28
29 if ~qeast % if qeast: skip roughness and whole beach angle analysis
30     %% Whole beach trend line and angle
31     p1 = polyfit(bs(:,1),bs(:,2),1);      % linear fit
32     angl = atand(p1(1));                  % angle is inv. tangent of slope, which is p1(1)
33     x1 = linspace(min(bs(:,1)),max(bs(:,1)),1E3); % for plotting
34     f1 = polyval(p1,x1);                 % for plotting
35
36     %% Beach roughness
37     Lc = sqrt(L^2+(p1(1)*L)^2);           % corrected beach length
38     c1 = bs(:,2) - (p1(1)*bs(:,1)+p1(2)); % beach particles y-position relative to ...
        linear fit
39
40     % Normalised mean deviation (1st moment)
41     mdevc = sum(abs(c1-mean(c1)))/size(c1,1); % Mean y-deviation
42     M2 = mdevc/Lc;                       % Normalized mean deviation
43
44     % Normalised standard deviation (2nd moment)
45     sigc = std(c1);                      % standard deviation
46     R2 = sigc/Lc;                        % Normalized sd
47
48     % Physical Surface Roughness: real divided by linear surface length
49     Lreal = path_length(bs(:,1),bs(:,2)); % real surface length
50     P2 = Lreal/Lc;                       % Surface roughness
51 end
52
53 %% output: roughness and angle data
54 coast = [];
55 coast2 = []; coast2.poly = p2; coast2.ang = ang2; coast2.x = x2; coast2.y = f2;
56 coast.east = coast2;

```

```

57
58 % if qeast: output only the east coast angle data
59 if qeast
60     coast = coast.east;
61 end
62
63 % if ~qeast: output all data
64 if ~qeast
65     coast1=[]; coast1.poly = p1; coast1.ang = angl; coast1.x = x1; coast1.y = f1;
66     coast.whole = coast1;
67     coast.rough.sigc = sigc;
68     coast.rough.mdevc = mdevc;
69     coast.rough.Lreal = Lreal;
70     coast.rough.Lc = Lc;
71     coast.rough.R2=R2;
72     coast.rough.M2=M2;
73     coast.rough.P2=P2;
74 end
75
76 end

```

The tweak value `x1a` is used for limiting the horizontal range over which the roughness and angle analyses are performed. It is a  $1 \times 2$  double array, containing the left- and right-most horizontal coordinate (in pixels) of the part of the beach to be analysed. This limiting is useful in case the beach starts with an incline due to geometrical reasons (e.g., the initial beach height  $B_0$  is higher than the wedge height  $h_w$ ), or when right-most last beach particle detected is not *actually* at the surface, due to the vertical wall on the right. The east coast angle is determined by making a linear fit through the right-most one-third part of the beach surface (note the `'/3'` in line 18). The angle of this fit is easily determined. If the input `qeast = 'east'`, only this east coast angle analysis is done. If this entry is not entered, also the rest of the beach will be analysed. The roughness and angle analyses starts also by making a linear fit through the surface particles, from which the angle is obtained easily. Next the roughness of the beach is determined. One way to quantify the roughness is by looking at the standard deviation of the particle positions from the linear fit. The Normalized Standard Deviation (R2, line 46) is this standard deviation divided by the beach surface length. Another way of looking at the roughness is by comparing the detailed length of the bed (i.e., the length of the path which connects all surface particles) with the 'macroscopic' beach length, i.e. the length of the linear fit. The Physical Surface Roughness (P2, line 50) is the ratio of the two.

## E.5 Sediment transport

With all particle coordinates, different stages of the beach profile can be compared to one another. The function `cl_sediment_transport.m` compares all subsequent beach profiles to the first, looking at differences in sediment location:

```

1 function ststruct = cl_sediment_transport(pindc,cindc,m,cltweak)
2
3 %% t0 data
4 b0 = cindc{1}; % beach surface at t0
5 bu0 = find_coast_underline(pindc{1},cltweak); % beach underline at t0
6
7 %% sediment transport time calculation
8 pst = zeros(1,length(cindc)); % positive st's
9 nst = pst; % negative st's
10 pcom = [pst' pst']; % positive centers of mass
11 ncom = pcom; % negative centers of mass
12
13 for i = 1:length(cindc)
14     bt = cindc{i}; % beach surface at t
15     but = find_coast_underline(pindc{i},cltweak); % beach underline at t
16
17     % adding 'left' part of both old and new beach
18     butleft = but(but(:,1)<b0(1,1),:); % part of beach at t which is left of beach at t0

```

```

19 bu0left = bu0(bu0(:,1)<bt(1,1),:); % part of beach at t0 which is left of beach at t
20
21 butleft(:,2) = butleft(:,2)-1.8E-3/m.mpix; % d_beads 1.8 mm correction
22 bu0left(:,2) = bu0left(:,2)-1.8E-3/m.mpix; % d_beads 1.8 mm correction
23
24 bt = [bu0left; bt]; % ) actual adding of left part to beach profiles
25 b0t = [butleft; b0]; % )
26
27 % scanning of beach at time t (bt)
28 dst = []; % array of net st on each particle position
29 dcom = []; % array of net st centers of mass
30 if i==length(cindc) % for hatched plot
31     dxl = [];
32     lines = [];
33 end
34 for j=2:size(bt,1)-1
35     for k=1:size(b0t,1)-1
36         if bt(j,1)>b0t(k,1) && bt(j,1)<=b0t(k+1,1) % particle bt(j,:) in ...
37             x-interval [b0t(k,1), b0t(k+1,1)]
38             dx1 = bt(j,1)-b0t(k,1); % x-distance to nearest ...
39             b0t-particle LEFT of particle bt(j,:)
40             dx2 = b0t(k+1,1)-bt(j,1); % x-distance to nearest ...
41             b0t-particle RIGHT of particle bt(j,:)
42             yki = b0t(k,2) + dx1/(dx1+dx2)*(b0t(k+1,2)-b0t(k,2));
43             % effective t0 y-coordinate on x-j
44             dxs = 1/2*(bt(j+1,1)-bt(j-1,1)); % effective st column width
45             xs = bt(j,1); % effective st x-coordinate
46             dys = (bt(j,2)-yki); % effective st column height
47
48             dst(end+1) = dxs * dys; % dx*dy; effective net st on x=xs (pix^2)
49             dcom(end+1,:) = [xs yki+dys/2]; % effective 'center of mass' of j'th net ...
50             st part
51
52             if i==length(cindc) % hatched plot data
53                 lines(end+1,:) = [xs bt(j,2) xs yki]; % lines ends: [x1 y1 x2 y2]
54                 dxl(end+1) = dxs; % lines thicknesses (dx, pixels)
55             end
56             break
57         end
58     end
59 end
60
61 % find net transports
62 pst(i) = sum(dst(dst>0)); % 'positive' net sediment transport (pix^2)
63 nst(i) = sum(dst(dst<0)); % 'negative' net sediment transport (pix^2)
64
65 % find average sediment replacement
66 pdst = dst(dst>0);
67 ndst = dst(dst<0);
68 pcom(i,:) = sum([pdst'.*dcom(dst>0,1) pdst'.*dcom(dst>0,2)] ,1)/pst(i); % center-of-mass
69 ncom(i,:) = sum([ndst'.*dcom(dst<0,1) ndst'.*dcom(dst<0,2)] ,1)/nst(i);
70 end
71
72 % sediment replacement
73 dist = abs(pcom-ncom);
74 rep = sqrt(dist(:,1).^2 + dist(:,2).^2); % sediment replacement (pix)
75
76 %% OUTPUT: ststruct
77 ststruct.pst = pst; % positive sediment transport (pix^2) (Nx1 double)
78 ststruct.nst = nst; % negative sediment transport (pix^2) (Nx1 double)
79 ststruct.pcom = pcom; % positive centers of mass (pix) (Nx2 double)
80 ststruct.ncom = ncom; % negative centers of mass (pix) (Nx2 double)
81 ststruct.rep = rep; % net sediment replacements (pix) (Nx1 double)
82
83 % for hatched plotting:
84 ststruct.lines = lines; % last frame st lines ends (pix) (Mx[x1 y1 x2 y2] = Mx4 double)
85 ststruct.dxl = dxl; % last frame st lines thicknesses (pix) (Mx1 double)
86

```

This function looks at the differences in height between the beach profiles, returning the positive sediment transport (sediment which wasn't there first but is there now, `pst` in  $\text{pix}^2$ ), negative sediment transport (sediment which was there first, but isn't there anymore, `nst` in  $\text{pix}^2$ ), their respective centers of mass (`pcom` and `ncom`) and the mean sediment replacement, i.e. the absolute distance between the centers of mass (`rep`).

## E.6 Phase diagrams

The function `cl_phase_diagrams.m` uses the data acquired in `cl_main.m` to do the determination of outcomes already explained in detail in section 4.4.1. The largest parts of the code in this function are about going through all measurements and plotting. Of interest is the fact that it uses the function `cl_ctr_times.m`, to determine for all measurements the time at which the bed state switches from dynamic to quasi-steady. It uses the CTR threshold  $R_{thresh}$  described in section 4.3.1 to determine this time. Further, the `if`-statement determining the steady bed morphology is worth taking a look at:

```

1  if length(cindc) <= 6*20 && np(1)-np(end) > 90 % short measurement, lot of particle loss
2      ns(k) = 8; % suction
3
4  elseif sum(bend(:,2)>H0)>=1 % dry parts of beach
5
6      if sum(bend(end-10:end,2)>H0)>=1 % dry part is in the east
7
8          if (bend(end,1) - bendmax(1))*m.mpix > 5E-2 % bed maximum > 5cm away from bed end
9              ns(k) = 3; % dune-beach
10             else
11                 ns(k) = 1; % dry beach
12             end
13         else % dry part is not in the east
14             ns(k) = 2; % dune
15         end
16
17     elseif eangle(qt(k)).ang >= 5 % east coast angle > 5 \deg
18         ns(k) = 5; % wet beach
19
20     elseif -st.nst(qt(k)).*1E4*m.mpix^2 >= 10 % transport > 7 cm^2
21         ns(k) = 6; % significant transport
22
23     else % none of the above
24         ns(k) = 7; % quasi-static
25     end

```

Here, `cindc` is an array whose length is the total number of frames, `np` is an array of the number of particles detected, `H0` is the mean water depth, `qt(k)` is the frame at which the state becomes quasi-steady, `bend` are the coordinates of the bed surface at frame `qt(k)`, `bendmax` contains the coordinates of the vertical maximum of the bed at frame `qt(k)`, `m.mpix` is the meter-per-pixel ratio, `eangle` is an array containing the eastern bed angles, `st.nst` is an array containing the negative sediment area (in  $\text{pix}^2$ ), and `ns` is a variable used for saving the SBMs.

The determination method matches the quantified outcome requirements listed in table 4.2.

## E.7 Plotting

Having extracted the useful data, all that is left is to turn them into understandable figures. Standard MATLAB functions are used for this, which are configured and called in `cl_plot.m` and its subfunctions. Figure 4.2 shows examples of the obtained plots.

# Appendix F

## Wave dynamics analysis

The high-speed image recordings of the wave dynamics were analysed using MATLAB. Figure F.1 shows a schematical representation of the analysis programs. A graphical representation is shown in figure F.2. The wave dynamics analysis is divided into data extraction (`fs_main.m`) and plotting (`fs_plot_slices(_beach).m`). After the measurement, the raw images are saved in a certain directory, say `path\`. A measurement-specific tweak file, `tweak_fs_1000fps.m`, is added to the folder above that path (`path\..\`). This file contains measurement specific data like the meter-per-pixel ratio, crop settings and analysis tweaks. The image cropping that follows in `imcrop_b.m` is again rather trivial; an example of a cropped image is shown in fig. F.2a.

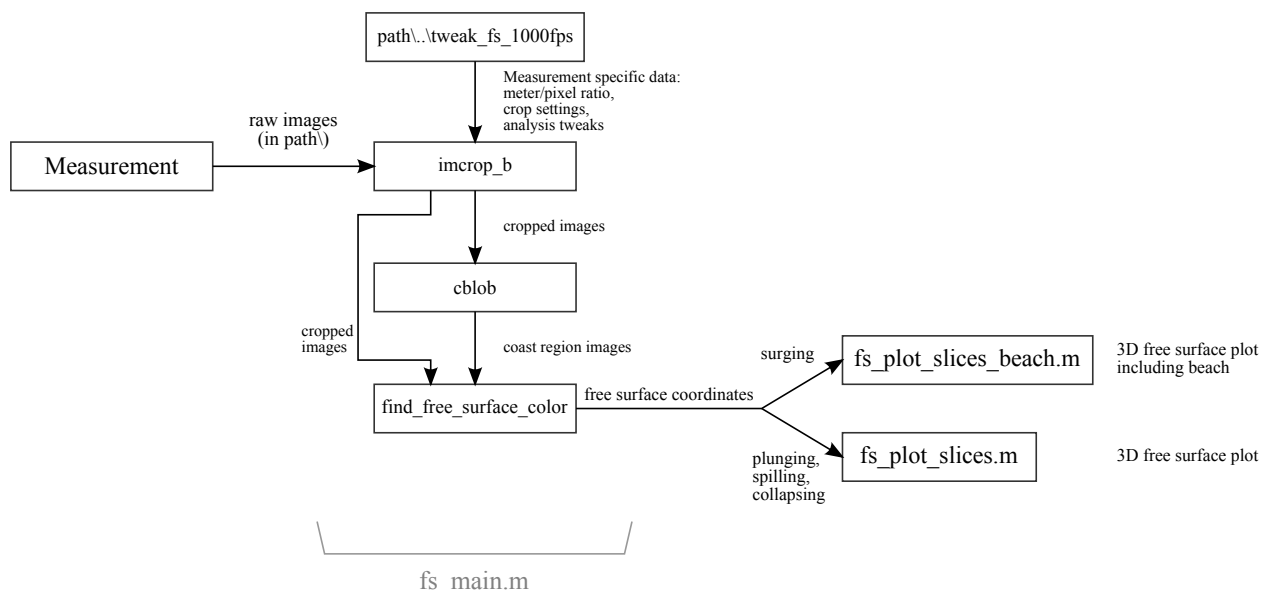


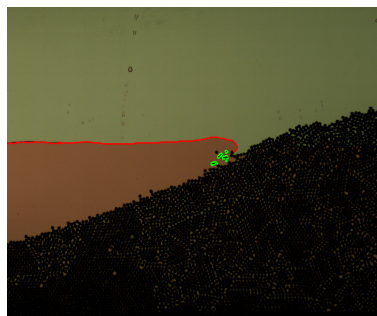
Figure F.1: Wave dynamics analysis program structure.



(a) Cropped image



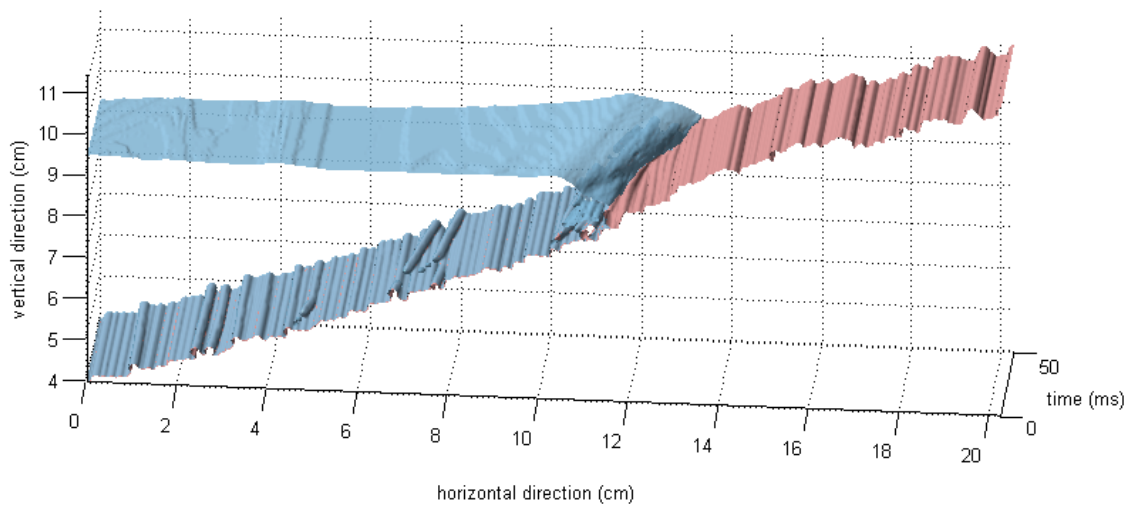
(b) Analysis result: red = free surface, green = air pockets



(c) Plotting range in x-direction



(d) Slice: grey = air (0), white = water (1), black = beach (-1)



(e) 3D Wave evolution plot: pasted-together time frames

## F.1 Free surface detection

The actual extraction of the free surface coordinates from the cropped figure is done in `find_free_surface_color.m`:

```
1 function indcoor = find_free_surface_color(Alcrop,ffstweak,Alblob)
2
3 %% TWEAK
4 % color selection
5 try hq = ffstweak.hq; hr = ffstweak.hr; end % hue limits
6 try sq = ffstweak.sq; sr = ffstweak.sr; end % saturation limits
7 try vq = ffstweak.vq; vr = ffstweak.vr; end % value limits
8 try rq = ffstweak.rq; rr = ffstweak.rr; end % red limits
9 try gq = ffstweak.gq; gr = ffstweak.gr; end % green limits
10 try bq = ffstweak.bq; br = ffstweak.br; end % blue limits
11
12 %% RGB to HSV
13 Alhsv = rgb2hsv(Alcrop);
14
15 %% hsv/rgb selection of region of interest
16 if exist('hq','var'); rh = roicolor(Alhsv(:,:,1),hq,hr); else rh=1; end
17 if exist('sq','var'); rs = roicolor(Alhsv(:,:,2),sq,sr); else rs=1; end
18 if exist('vq','var'); rv = roicolor(Alhsv(:,:,3),vq,vr); else rv=1; end
19 if exist('rq','var'); r0r = roicolor(Alcrop(:,:,1),rq,rr); else r0r=1; end
20 if exist('gq','var'); rg = roicolor(Alcrop(:,:,2),gq,gr); else rg=1; end
21 if exist('bq','var'); rb = roicolor(Alcrop(:,:,3),bq,br); else rb=1; end
22
23 im = im2bw( rh.*rs.*rv .* r0r.*rg.*rb, .5);
24
25 %% find water object: largest object!
26 b = regionprops(im,'Image','BoundingBox','Area','Extrema');
27 q=1;
28 for j=1:length(b)
29     if b(j).Area>b(q).Area
30         q=j;
31     end
32 end
33 wobj = b(q);
34
35 rt = wobj.Extrema(3,:); % RIGHT TOP of water object
36 lt = wobj.Extrema(8,:); % LEFT TOP of water object
37
38 %% remove all non-water objects
39 imw = zeros(size(im,1),size(im,2));
40 wbb = wobj.BoundingBox;
41 imw(ceil(wbb(2)):ceil(wbb(2))+wbb(4)-1,ceil(wbb(1)):ceil(wbb(1))+wbb(3)-1) ...
42     = wobj.Image;
43
44 %% find water and bubbles
45 b2 = bwboundaries(imw);
46
47 % select water and air pockets
48 j=0;
49 boundaries = cell(1,length(b2));
50 for k=1:length(b2)
51     if length(b2{k})>sqrt(2*pi*ffstweak.wbmax2) % interesting object
52         j=j+1;
53         boundaries{j}=b2{k};
54     end
55 end
56 boundaries=boundaries(1:j);
57
58 %% crop upper part of water boundary (= free surface!)
59 bwater = boundaries{1};
60 bwater.new=zeros(size(bwater,1),size(bwater,2));
61 q = 0;
```

```

62 for i=1:length(bwater) % ALWAYS starts at lt: intrinsic property of bwboundaries
63     q=q+1;
64     bwater_new(q,:) = bwater(i,:);
65
66     % non-surgng breaker: break at right-most surface coordinate: rt
67     if ~exist('A1blob','var')
68         if abs(bwater(i,1)-rt(2))<1 && abs(bwater(i,2)-rt(1))<1
69             break
70         end
71     else % surging breaker: break when surface meets beach (A1blob)
72         if A1blob(bwater(i,1),bwater(i,2))
73             break
74         end
75     end
76     %
77     if abs(bwater(i,1)-rt(2))<1 && abs(bwater(i,2)-rt(1))<1
78         break
79     end
80 end
81 boundaries{1}=bwater_new(1:q,:);
82
83 %% output
84 % indcoor: particle coordinates in Alcrop figure; horizontal = (:,1), vertical = (:,2)
85 indcoor = cell(1,length(boundaries));
86 for i=1:length(boundaries)
87     for j=1:length(boundaries{i})
88         indcoor{i}(:,1) = boundaries{i}(:,2);
89         % horizontal coordinate = horizontal matrix position
90         indcoor{i}(:,2) = size(A1crop,1) - boundaries{i}(:,1) + 1;
91         % vertical coordinate = vertical matrix size - vertical matrix position + 1
92     end
93 end
94
95 end

```

A key step in the analysis is taken in line 13: the conversion of the image to Hue-Saturation-Value variable space. Since the water is colored red, the hue color channel is ideal for the water area detection. The input variable `ffstweak` contains selection limits of color values of any color channel preferred. The value of `ffstweak` differs between measurements, as the useful color channel limits depend on things like lightning, shutter time and the amount of dye added to the water. Typically, only the hue and saturation channels are used to select a so-called 'region of interest'. The regions of interest of the selected channels are obtained using `roicolor` (lines 16-21). These regions are then combined in line 23. This basically already selects the water area. `regionprops` is next used to get rid of any possible noise, making use of the fact that the water area is the largest object in the combined region of interest image (`im`). Lastly, `bwboundaries` is used to get the actual coordinates of the free surface and air pockets. Note that when analysing a surging breaker, `A1blob` (output of `cblob.m`) needs to be given as input. The output variable `indcoor` is a cell array containing the free surface coordinates in the first index, followed by all found air pockets. Figure F.2b shows the output in the (cropped) original figure. The free surface is shown in red, while the submerged air pockets are plotted in green. The data of all images of a certain measurement is gathered in `fs_main.m` and from there saved to a `.mat` data file.

## F.2 Plotting

Next, the acquired data is loaded again from the data file, and plotted using the functions `isosurface`, `isonormals` and `patch`. Surging breakers are plotted in `fs_plot_slices_beach.m`:

```

1 %% Function:
2 % script for plotting the free surface data obtained with fs_main.m,
3 % together with the beach obtained from cblob.
4 %
5 %% ----- TWEAK -----

```

```

6 expdir = 'G:\Bram\Experiments\20120126';
7 run([expdir, '\tweak_fs.1000fps']); % GIVES: mpix, c, btweak, fftweak
8 expname = '1000fps_H095-0.9Hz-sur';
9
10 fwm = 0.9; % wave maker frequency in Hz
11 fps = 1000; % camera speed in frames per second
12 dt = 1/fps; % time interval between frames
13
14 % plot range
15 xmin = 800; % x lower limit
16 xmax = 1600; % x upper limit
17 first = 400; % first frame
18 last = 700; % last frame
19
20 % plot options
21 fsfolder = 'fsplots'; % plot save folder
22 fcolor = [.6 .85 1]; % free surface face color
23 fcolor2 = [1 .7 .7]; % beach color
24 smoothfactor = 1; % number of times the fs gets smoothed
25 lights = [-60,60]; falpha = 0.85; % lighting and water opacity
26
27 %% load data
28 andir = [expdir, '\', expname, '\analysis'];
29 anfile = [andir, '\analysis.mat'];
30 ims = dir([expdir, '\', expname, '*tif']);
31
32 load(anfile); % gives fsindc{frame}{obj}([x,y])
33
34 %% Make slices
35 scrop = [c.height+1,c.width+1]; % crop image size
36 imwhite = true(scrop); % slyce input: crop-sized white image
37 imwhite = imwhite(:,xmin:xmax);
38
39 [ymin ymax] = yextr(fsindc(first:last),[xmin xmax]); % extract min and max of surface y-data
40 voll = zeros((ymax-ymin+1), (xmax-xmin+1), (last-first+1)); % pre-allocation
41
42 for i=first:last
43 % select surface coordinate data of frame i
44 fsi = fsindc{i};
45
46 % get coast region
47 Alblob = cblob(iscrop_b([expdir, '\', expname, '\', ims(i).name],c),btweak);
48
49 % turn surface data into a black-and-white slice
50 islice = slyce(imwhite,fsi,[xmin xmax],0,Alblob,'sur');
51
52 % add the slice to the 3D matrix
53 voll(:, :, i-first+1) = islice( (size(islice,1)-ymax+1):(size(islice,1)-ymin+1) , : );
54 end
55
56 %% permuting and smoothing
57 voll = permute(flipdim(voll,1),[3 2 1]);
58
59 if smoothfactor>0
60 for q = 1:smoothfactor
61 voll = smooth3(voll);
62 end
63 end
64
65 %% plotting
66 % axes
67 X = (0:1:xmax-xmin).*mpix*1E2; % x (cm)
68 Y = (0:1:last-first).*dt*1E3; % t (ms)
69 Z = (0:1:ymax-ymin).*mpix*1E2; % y (cm)
70
71 % open figure
72 fig1 = figure;
73

```

```

74 % surface 1: air-water free surface
75 surface1 = isosurface(X,Y,Z,vol1,0.25);           % surface data
76 colormap gray
77 hiso = patch('Vertices',surface1.vertices,...    % patching the surface
78             'Faces',surface1.faces,...
79             'FaceColor',fcolor,...
80             'FaceAlpha',falpa,...
81             'EdgeColor','none');
82 isonormals(X,Y,Z,vol1,hiso)                       % plotting the surface
83 grid on
84
85 set(hiso,'SpecularColorReflectance',0,'SpecularExponent',50)
86 view(25,25)                                       % view angle
87
88 % title and labels
89 tfwm = ['f_{wm}=',num2str(fwm,'%1.2f'),'Hz'];
90 tcam = ['cam speed = ',num2str(fps,'%1.0f'),'fps'];
91 title({'Time evolution of water-air free surface profile;';
92       [tfwm,' ',tcam, '.']});
93 xlabel('horizontal direction (cm)')
94 ylabel('vertical direction (cm)')
95 ylabel(['time (ms)'])
96 daspect([1 15 1])                                % data aspect ratio
97
98 hold on
99
100 % surface 2: beach
101 surface2 = isosurface(X,Y,Z,vol1,-.25);
102 hiso2 = patch('Vertices',surface2.vertices,...
103             'Faces',surface2.faces,...
104             'FaceColor',fcolor2,...
105             'EdgeColor','none');
106 isonormals(X,Y,Z,vol1,hiso2)
107 set(hiso2,'SpecularColorReflectance',0,'SpecularExponent',50)
108
109 for i=1:size(lights,1)
110     lightangle(lights(i,1),lights(i,2));
111 end
112
113 % lighting
114 lighting gouraud
115 axis tight
116
117 %% save
118 imname = ['f',num2str(first),'to',num2str(last),'_x',num2str(xmin),'to',num2str(xmax)];
119 sfig(fig1,[andir,'\',fsfolder,'\',imname])

```

The acquired wave data is loaded in line 32. To focus on the important details of the analysis, first a plotting range in both the x-direction and time is chosen in lines 15-18. Figure F.2c shows an example of such a selected range in the x-direction. To make the plot with `isosurface` and `isonormals`, the x-y-t data has to be turned into a 3-dimensional data matrix. This matrix is `vol1`, which is pre-allocated in line 40. Next, for all plotted time frames three things are done. First, the beach location is retrieved using `cblob` (see app. E.1) in line 47. Second, the function `slyce` in line 50 turns the surface coordinate data into a 2D image matrix containing three regions with three different values: 0 where there is air, 1 where there is water, and -1 where there is beach. An example of such a slice is shown in figure F.2d. Lastly, the 'slice' is added to the 3D data matrix `vol1` in line 53. In the rest of the script, the actual plotting is performed. Figure F.2e shows an example of such a wave evolution plot.

The observed spilling, plunging and collapsing breakers are plotted in the simpler plotting program `fs_plot_slices.m`, which does almost the same but leaves out the beach region.